PNEUMATIC VARIABLE STIFFNESS MECHANISMS FOR APPLICATION IN LOWER-LIMB EXOSKELETONS

Luka Mišković

Doctoral Dissertation
Jožef Stefan International Postgraduate School
Ljubljana, Slovenia

Supervisor: Prof. Tadej Petrič, Jožef Stefan Institute, Ljubljana, Slovenia

Evaluation Board:
Prof. Andrej Gams, Chair, Jožef Stefan Institute, Ljubljana, Slovenia
Prof. Matjaž Mihelj, Member, Faculty of Electrical Engineering, Ljubljana, Slovenia
Prof. Lorenzo Masia, Member, Institute for Technical Informatics (ZITI), Heidelberg University, Germany

MEDNARODNA PODIPLOMSKA ŠOLA JOŽEFA STEFANA
JOŽEF STEFAN INTERNATIONAL POSTGRADUATE SCHOOL

Luka Mišković

PNEUMATIC VARIABLE STIFFNESS MECHANISMS FOR APPLICATION IN LOWER-LIMB EXOSKELETONS

Doctoral Dissertation

PNEVMATSKI MEHANIZMI S SPREMENLJIVO TOGOSTJO ZA UPORABO V EKSOSKELETIH SPODNJIH OKONČIN

Doktorska disertacija

Supervisor: Prof. Tadej Petrič

Ljubljana, Slovenia, October 2024

To my family

Acknowledgments

First and foremost, I am sincerely grateful to my mentor, Prof. Dr. Tadej Petrič, for giving me the opportunity to pursue this doctoral program. His constant support, guidance, and trust in my ideas have been invaluable along the way.

I would like to express my heartfelt gratitude to my family and friends for their unwavering encouragement and understanding. Their support has been essential in both my academic and personal life.

A special mention goes to my fiancee, Kristina, for her tremendous support and patience during the challenging times of my PhD. Her love and encouragement have been a huge part of me reaching this milestone.

To the friends I have made during my time in Slovenia, your friendship and support have been a constant source of strength and motivation. I extend my gratitude to my office colleagues and the rest of the E1 department at the Jožef Stefan Institute. Their support has made my time here enjoyable and productive. This research would not have been possible without the support of the department head, Prof. Dr. Aleš Ude.

This research was made possible by funding from the Slovenian Research Agency (ARIS, Research Core Funding No. PR-10489). I am also grateful to the Erasmus+ program for partially financing my research stay at Heidelberg University. Lastly, my sincere appreciation to the entire ARIES laboratory team, under the leadership of Prof. Dr. Lorenzo Masia, for sharing their expertise and hosting me during my research stay.

Abstract

Wearable robotics holds promise for enhancing human capabilities and addressing motor challenges in individuals with impairments, amputations, or those who are healthy. Exoskeletons, among various wearable devices, are designed to be worn on the upper or lower limbs. While some applications, like in the medical field, have been widely adopted, others still face unique challenges. These challenges primarily center around Actuation, Control, and Ergonomics. This thesis primarily focuses on inventing actuators with novel superior functionalities together with corresponding control algorithms and their application in lower limb exoskeletons. The thesis contains four main parts, each representing a distinct phase of the research process.

In the first part, a quasi-passive pneumatic variable stiffness mechanism is introduced, mathematically described, and experimentally evaluated. This mechanism is distinctive as it utilizes a vacuum to draw air from the atmosphere, thereby adjusting the pressure inside the actuator. This approach enables the pneumatic mechanism to mimic the behavior of a nonlinear variable stiffness spring without requiring an external air supply. Additionally, through a proposed valve combination, the mechanism can be completely deactivated to allow free motion, while also offering the capability to incrementally adjust stiffness.

In the second part, based on the fundamental principles of the quasi-passive mechanism, the air harvesting capabilities are extended to the entire Pneumatic Exoskeleton Joint Mechanism (PEJM). This design introduces additional components, including the Pneumatic Artificial Muscle (PAM), which acts as a soft reservoir for the harvested air and additionally influences the stiffness of the joint. At this stage, the exoskeleton joint remains quasi-passive and continues to rely on vacuum for air intake. The joint undergoes experimental validation using a setup that does not involve human subjects.

In the third part, a mechatronic concept of a complete pneumatic fully portable bilateral knee exoskeleton is presented. The novelty lies in its multimodal functionality, allowing the exoskeleton to operate in both active and quasi-passive modes using the same actuator. This versatility improves energy efficiency by enabling air recovery in quasi-passive mode and the reuse of stored air in active mode, which also uses an integrated air pump. A pilot study involving a single healthy participant is conducted to demonstrate simultaneous energy recovery and human assistance.

Finally, the fourth part is about the hybrid rigid-soft and pneumatic-electromechanical exoskeleton for multi-joint lower limb assistance. This concept uses tendon-driven electromechanical actuation for the hip joint and a pneumatic rigid exoskeleton for the knee joint. The hip joint, with its three active degrees of freedom (DoF), benefits from tendon-driven actuation, simplifying mechanics. Conversely, the knee joint, with its single active DoF crucial for weight-bearing, exhibits compliance during the weight acceptance phase, making it suitable for a pneumatic exoskeleton. The exoskeleton is evaluated in human studies while measuring their metabolic cost, muscular activity, and kinematics.

Povzetek

Robotika, ki jo je mogoče nositi, je obetavna za izboljšanje človeških zmogljivosti in reševanje motoričnih izzivov pri posameznikih z okvarami, amputacijami ali pri zdravih osebah. Eksoskeleti so med različnimi nosljivimi napravami zasnovani za nošenje na zgornjih ali spodnjih okončinah. Medtem ko so se nekatere aplikacije, na primer na medicinskem področju, že široko uveljavile, se druge še vedno soočajo z edinstvenimi izzivi. Ti izzivi se osredotočajo predvsem na aktuatroje, vodenje in ergonomijo. Ta disertacija se osredotoča predvsem na raziskave na področju aktuatorjev z naprednimi lastonstmi skupaj z ustreznimi algoritmi za vodenje in njihovo uporabo v eksoskeletih za spodnje okončine. Disertacija vsebuje štiri dele, od katerih vsak predstavlja ločeno fazo raziskovalnega procesa.

V prvem delu je predstavljen, matematično opisan in eksperimentalno ovrednoten kvazipasivni pnevmatski mehanizem s spremenljivo togostjo. Ta mehanizem je svojevrsten, saj uporablja vakuum za črpanje zraka iz ozračja, s čimer uravnava tlak v aktuatorju. Ta pristop omogoča, da pnevmatski mehanizem posnema obnašanje nelinearne vzmeti s spremenljivo togostjo, ne da bi potreboval zunanji dovod zraka. Poleg tega je mogoče mehanizem z izbrano kombinacijo ventilov popolnoma izklopiti, da se omogoči prosto gibanje, obenem pa je možno tudi postopno prilagajanje togosti.

V drugem delu so na podlagi temeljnih načel kvazipasivnega mehanizma razširjene funkcionalnosti shranjevanja zraka na celotni pnevmatski eksoskeletni sklepni mehanizem (PEJM). Ta zasnova uvaja dodatne komponente, vključno s pnevmatsko umetno mišico (PAM), ki deluje kot mehki rezervoar za zbrani zrak in dodatno vpliva na togost sklepa. Na tej stopnji razvoja ostaja eksoskeletni sklep kvazipasiven in še vedno temelji na vakuumu za zajem zraka. Razvit sklepmi mehanizem je ovrednoten z uporabo eksperimentalnega sistema, ki ne vključuje človeških subjektov.

V tretjem delu je predstavljen mehatronski koncept celovitega pnevmatskega bilateralnega kolenskega eksoskeleta. Novost je v njegovi multimodalni funkcionalnosti, ki eksoskeletu omogoča delovanje v aktivnem in kvazi pasivnem načinu z uporabo istega aktuatorja. Ta multifunkcionalnost izboljšuje energetsko učinkovitost, saj omogoča rekuperacijo zraka v kvazipasivnem načinu in ponovno uporabo shranjenega zraka v aktivnem načinu, ki prav tako uporablja vgrajeno zračno črpalko. Izvedena je pilotna študija, ki vključuje enega zdrav subjekt,z namenom ponazoritve hkratnega pridobivanja energije in podpore človeku.

V četrtem delu je predstavljen hibridni togo-mehki in pnevmatsko-elektromehanski eksoskelet za večsklepno pomoč spodnjim okončinam. Ta koncept uporablja tetive za kolčni sklep in pnevmatski eksoskelet za kolenski sklep. Kolčni sklep s tremi aktivnimi prostostnimi stopnjami izkorišča pogon na tetive, kar poenostavlja mehaniko. Nasprotno pa kolenski sklep z eno aktivno prostostnjo stopnjo prevzame del obremenitve med stojo ali hojo. Razviti eksoskelet smo evalvirali v raziskavi, ki je vključevala seden subjektov, pri čemer smo merili njihovo metabolično porabo, mišično aktivnost in kinematiko.

Contents

List of Figures xvii

List of Tables xxv

Abbreviations xxvii

Glossary xxix

1 Introduction 1
- 1.1 Ongoing Challenges . . . 3
- 1.2 Purpose of the Dissertation . . . 6
- 1.3 Goals of the Dissertation . . . 8
- 1.4 Hypothesis . . . 8
- 1.5 Structure of the Dissertation . . . 9

2 Literature Review 11
- 2.1 Lower Limb Exoskeletons . . . 11
  - 2.1.1 Energy Flow Between Humans and Exoskeletons . . . 12
  - 2.1.2 Active Exoskeletons and Actuators . . . 13
    - 2.1.2.1 Electromechanical Actuators . . . 13
    - 2.1.2.2 Pneumatic Actuators . . . 13
    - 2.1.2.3 Hydraulic Actuators . . . 14
    - 2.1.2.4 Variable Stiffness . . . 14
      - 2.1.2.4.1 Electromechanical Variable Stiffness: . . . 15
      - 2.1.2.4.2 Pneumatic Variable Stiffness: . . . 17
  - 2.1.3 Energy Harvesting Exoskeletons . . . 18
  - 2.1.4 Passive and Quasi-Passive Exoskeletons . . . 19
  - 2.1.5 Rigid Exoskeletons and Soft Exosuits . . . 21
  - 2.1.6 Control of Lower-Limb Exoskeletons . . . 22
- 2.2 Proposed Methodologies . . . 23

3 Quasi-Passive Pneumatic Variable Stiffness Mechanism 27
- 3.1 Mathematical Model . . . 28
  - 3.1.1 Modeling the Stiffness of the Quasi-Passive Mechanism . . . 29
- 3.2 Experimental Evaluation . . . 32
  - 3.2.1 Description of Components . . . 32
  - 3.2.2 Experimental Procedure . . . 33
- 3.3 Results . . . 35
- 3.4 Application, Comparison, and Discussion . . . 36
  - 3.4.1 Comparison with Existing Solutions . . . 37
- 3.5 Chapter Conclusion . . . 38

4 Pneumatic Exoskeleton Joint Mechanism 41
- 4.1 Design and Operating Principle . . . 42
  - 4.1.1 System Overview . . . 42
  - 4.1.2 Kinematic Analysis . . . 43
  - 4.1.3 Torque modeling . . . 45
- 4.2 Novel Variable Stiffness Method . . . 47
- 4.3 Experimental Setup for the Joint Mechanism . . . 50
  - 4.3.1 Mechatronic Design of the Experimental Setup . . . 50
  - 4.3.2 Controller Structure . . . 51
- 4.4 Experimental Procedure and Results . . . 52
  - 4.4.1 Basic Mechanism Verification . . . 53
  - 4.4.2 Pneumatic Cylinder Pressure Increase . . . 54
  - 4.4.3 PAM pumping . . . 55
  - 4.4.4 PAM as an Air Tank . . . 56
  - 4.4.5 Pumping PAM Using an External Pump . . . 56
  - 4.4.6 Temperature Variation Effect . . . 57
  - 4.4.7 Leak Analysis . . . 58
- 4.5 Discussion . . . 58
  - 4.5.1 Application . . . 60
- 4.6 Chapter Conclusion . . . 61

5 Knee Exoskeleton with Bidirectional Energy Flow 63
- 5.1 Overview of the Exoskeleton . . . 65
  - 5.1.1 Exoskeleton Design . . . 65
    - 5.1.1.1 Actuator Unit . . . 65
    - 5.1.1.2 Control Unit . . . 66
    - 5.1.1.3 Pneumatic Multimodalities . . . 66
- 5.2 Mathematical Model . . . 67
  - 5.2.1 Air Pump . . . 67
  - 5.2.2 Pneumatic Artificial Muscle (PAM) . . . 68
  - 5.2.3 Actuator Pressure, Force, and Torque . . . 69
- 5.3 Concept of Energy Recovery in Sit-Stand . . . 71
- 5.4 Human Subject Experimentation . . . 72
  - 5.4.1 Experiment . . . 72
- 5.5 Discussion . . . 74
- 5.6 Chapter Conclusion . . . 75

6 Hybrid Rigid-Soft Exoskeleton for Multi-joint Lower Limb Assistance 77
- 6.1 Hybrid Concept . . . 78
  - 6.1.1 Tendon-Driven Hip Exosuit . . . 78
    - 6.1.1.1 Design . . . 78
    - 6.1.1.2 Control . . . 79
  - 6.1.2 Pneumatic Rigid Knee Exoskeleton . . . 79
    - 6.1.2.1 Design . . . 80
    - 6.1.2.2 Control . . . 80
  - 6.1.3 Technical Metrics and Hybrid Gait Assistance . . . 81
- 6.2 Experimental Evaluation with Human Subjects . . . 82
  - 6.2.1 Experimental Setup . . . 82
  - 6.2.2 Experimental Protocol . . . 83
  - 6.2.3 Data and Statistical Analysis . . . 84
    - 6.2.3.1 Muscular Activity . . . 84

6.2.3.2 Metabolic Cost 84
6.2.3.3 Kinematics 85
6.2.3.4 Hip Motor and Knee Exoskeleton Torque 85
6.2.4 Statistical Analysis 85
6.3 Results of Muscular Activity, Metabolic Cost, and Kinematics 85
6.3.1 Muscular Activity 85
6.3.2 Metabolic Cost 87
6.3.3 Kinematics 87
6.3.4 User Preference 88
6.3.5 Assistance Profiles: Hip Motor and Knee Actuator 89
6.4 Discussion 90
6.4.1 Versatility of the Proposed Hybrid Configuration 92
6.5 Chapter Conclusion 92

7 Conclusion **95**

References **97**

Bibliography **113**

Biography **115**

List of Figures

Figure 1.1: (a) Medical: ABLE by ABLE Human Motion (lower-limb active exoskeleton), ArmeoSpring by Hocoma (for arm rehabilitation), ReWalk exosuit (for ankle rehabilitation). (b) Consumer: FitExo by Enhanced Robotics, Elevate pneumatic exoskeleton by ROAM Robotics (enhances skiing endurance), GEMS (Gait Enhancing and Motivation System) by Samsung (for haptic feedback in gaming). (c) Occupational: Ottobock Paexo, Atoun by Panasonic, CarrySuit by Auxivo, Cray by German Bionic (enhance endurance during lifting). (d) Military: PowerWalk by Bionic Power, for electrical energy harvesting, and Onyx by Lockheed Martin for increased weight carrying. 1

Figure 2.1: Examples of lower limb exoskeletons. (a) and (b) depict complete mobilization lower limb exoskeletons, while (c) through (g) show partial assistance exoskeletons. In (a), the ATALANTE exoskeleton by Wandercraft weighs 80 kg and features 12 actuated joints [74], [75]. (b) showcases the ReWalk Personal Exoskeleton, weighing 20.4 kg with two actuated joints per leg [76], [77]. (c) Myosuit by Myoswiss AG, weighs 4.5 kg and is designed for knee extension assistance in patients with motor disorders [3]. (d) Hip exoskeleton for walking, running, and stair ascent weighs 3.5 kg [37]. (e) Samsung hip exoskeleton for assisting healthy human subjects, reducing the metabolic cost of walking, and weighing 2.4 kg [12]. (f) Ankle exoskeleton aimed at improving walking in individuals with cerebral palsy, weighing 2.8 kg [78]. (g) Tendon-driven exoskeleton (a concept known as an exosuit) provides hip assistance and weighs 2.87 kg [79]. 11

Figure 2.2: Three examples of the energy cycle between humans and exoskeletons. Negative joint power generated by human joints is depicted in red, positive power is shown in blue, and exoskeleton power is represented in green. (a) Active exoskeletons inject energy at the joint during the positive power intervals of the gait via an actuator. (b) Passive exoskeletons store energy during the negative power intervals and immediately return it to the same joint through elastic components. (c) Energy-harvesting exoskeletons extract energy from the joint during the negative power intervals of the gait and generate electricity or compressed air in the case of pneumatic exoskeletons. The figure is adapted from [54]. 12

Figure 2.3: Examples of electromechanical actuators in lower limb exoskeletons for partial assistance: (a) Transmission system with belt, ball screw, and levers for mechanical advantage at the knee joint [38]. (b) Combination of helical gear, ballscrew, and fiberglass springs for torque amplification at the hip joint [37]. (c) Planet gears on the output of a BLDC motor in a knee exoskeleton [88]. (d) Actuator denoted with number two, with a rope wound around the output pulley for ankle joint assistance [40]. 14
Figure 2.4: Examples of pneumatic actuators in lower limb exoskeletons for partial assistance: (a) Portable hip exoskeleton with pneumatic cylinder [41]. (b) Soft inflatable actuator for knee assistance [90]. (c) Pneumatic ankle exoskeleton with double-piston crank power source [42]. (d) Exoboot, a soft inflatable robotic boot providing ankle assistance [43]. (e) McKibben Pneumatic Artificial Muscles (PAMs) in bioinspired design [91]. (f) Custom McKibben-style pneumatic actuators for hip, knee, and ankle assistance [46]. (g) Commercialized pneumatic knee exoskeleton with fabric actuator from ROAM Robotics [92]. (h) Robotic ankle-foot orthosis with inflatable actuator aiding in plantarflexion for gait rehabilitation [45]. 15
Figure 2.5: Ottobock C-Brace®. Figure adapted from [97]. 16
Figure 2.6: Actuator architectures: (a) Stiff actuator, (b) Series elastic actuator adds compliance, (c) Variable stiffness actuators adjust the stiffness of the spring through various mechanisms. 16
Figure 2.7: Various mechanisms for adjusting stiffness include (a) Spring pretension-based involving different spring configurations; (b) mechanisms employing variable moment arms with a movable pivot point; and (c) adjustments based on variable length. Figure adapted from [113]. 16
Figure 2.8: Electromechanical variable stiffness actuators using different mechanisms. (a) MACCEPA actuator utilizes a spring pretension-based mechanism adjusted by a lever arm, as depicted in the schematic. Motor 2 in the prototype adjusts spring pretension, while Motor 1 controls joint rotation [105], [114]. (b) AwAS-II alters stiffness by modifying the transmission between load and spring, achieved through pivot repositioning while maintaining fixed spring position [108]. (c) Braun et al. achieve wide-range stiffness modulation using a variable-length leaf spring [112]. 17
Figure 2.9: An example of a pneumatic variable stiffness actuator (schematic diagram). Figure adapted from [117]. 18
Figure 2.10: Exoskeletons for biomechanical energy harvesting: (a) Illustrates a device that converts biomechanical energy into electrical energy [122]. (b) Shows a device that generates compressed air from biomechanical energy [55]. 18
Figure 2.11: Examples of passive exoskeletons without clutches: (a) Hip exoskeleton aiding flexion and extension [30]. (b) Elastic band assisting hip flexion [31]. (c) LiftSuit by AUXIVO AG supports the lower back during lifting tasks or forward-leaning positions [32]. (d) SPEXOR Exoskeleton utilizing MACCEPA variable stiffness mechanics for lower back support [124]. (e) Ottobock Paexo shoulder exoskeleton for industrial workers [28]. 19
Figure 2.12: Examples of passive exoskeletons with clutches: (a) Ratchet-Pawl-based clutch activated via pin only at specific angles [26]. (b) Low-profile friction clutch mechanism [27]. 20

Figure 2.13: Quasi-Passive exoskeletons featuring passive actuators that are engaged or disengaged by actively controlled clutches. (a) Depicts a pneumatic-based friction clutch [34]. (b) Shows a custom interference clutch integrated with a planetary gear transmission [36]. (c) Includes a mechanical ratchet-pawl clutch actuated by a servo motor [35]. 20
Figure 2.14: From Hardiman to more ergonomic rigid exoskeletons to exosuits. The figure is adapted from Xiloyannis et al. [57]. 21
Figure 2.15: Latest advancements in exosuits. (a) Exosuit targeting hip flexion to treat freezing in Parkinson's disease patients [132]. (b) Exosuit aiding hip extension, resulting in reduced sprinting time [10]. (c) Pneumatic inflatable exosuit facilitating both hip flexion and extension [133]. . . . 22
Figure 2.16: Control strategies classification diagram for lower-limb exoskeletons by Baud et al. [50]. Red indicates higher occurrences in literature, and blue is the opposite. 23
Figure 2.17: Key milestones in the dissertation. (a) Pneumatic quasi-passive variable stiffness mechanism for energy storage applications, published in [143]. (b) Pneumatic exoskeleton joint with a self-supporting air tank and stiffness modulation, published in [144]. (c) Active, quasi-passive, pneumatic and portable knee exoskeleton with bidirectional energy flow for efficient air recovery, published in [145]. (d) Hybrid rigid-soft and pneumatic-electromechanical exoskeleton for multi-joint lower limb assistance, published in [146]. 24

Figure 3.1: Possible states of the quasi-passive mechanism, where ON denotes that the valve is open and vice versa, OFF indicates that the valve is closed. 29
Figure 3.2: Theoretical forces in both chambers and total force when functioning as a nonlinear spring. $F_{\mathrm{m}n}$ is the total force to pull the rod from its initial position, $F_{\mathrm{u}n}$ is the pulling force due to vacuum, $F_{\mathrm{c}n}$ is the pushing force due to compressed air. Forces shown are before the stiffness increase ($p_{\mathrm{i}0} = p_{\mathrm{atm}}$). 30
Figure 3.3: Stiffness modulation method in a pneumatic quasi-passive mechanism. Modes are switched in a timed sequence while the piston rod is deflected by an external force to adjust the pressure inside the cylinder. Below atmospheric air pressure is used to draw additional air into the cylinder. 31
Figure 3.4: Modulation of the initial pressure for different sizes of cylinder diameter and $z = z_{\mathrm{max}} = 100$ mm. 32
Figure 3.5: Theoretical increase in maximum stiffness and energy storage capacity for different initial pressure and cylinder sizes. Results shown are for the cylinder with a total stroke length of 100 mm. 32
Figure 3.6: Schematic of the experimental setup composed of: Quasi-passive mechanism, Load and Control System. 33
Figure 3.7: Experimental setup. a) Overview, b) Quasi-passive mechanism c) Load 34
Figure 3.8: Experimental results depicting the force of the quasi-passive mechanism in relation to linear displacement for various stepwise increments of initial pressures $p_{\mathrm{i}n}$. Theoretical results are presented in (a), while (b) displays the measured results. 35
Figure 3.9: Experimental force measurements in the air cylinder versus linear displacement at five initial positions z_0, with constant initial pressure $p_{\mathrm{i}n} = 1$ bar and a cylinder stroke of 100 mm. The dashed curve depicts theoretical results. 36

Figure 3.10: Proposed application of a pneumatic quasi-passive variable stiffness mechanism for a portable ankle exoskeleton. 37

Figure 4.1: In (a) the PEJM CAD model applied to the knee exoskeleton, in (b) an exploded view. 43

Figure 4.2: Kinematic model of the proposed mechanism. The point $\mathrm{P_j}$ marks the center of rotation and the origin. The perpendicular distance, denoted by r, between $\mathrm{P_j}$ and l represents the moment arm, and l is the length between the endpoints of the cylinder. (a) With $\theta = 0°$, (b) with $\theta \neq 0°$, and (c) the triangle $\Delta \mathrm{A'B'P_j}$ shows a more detailed representation of vectors. 44

Figure 4.3: Joint rotation (θ) creates negative pressure ($p_{\mathrm{u}n}$) in the blue chamber, generating force $F_{\mathrm{u}n}$, while compressed air in the red chamber ($p_{\mathrm{c}n}$) produces force $F_{\mathrm{c}n}$. The total force ($F_{\mathrm{tot}n}$) generates torque $T_{\mathrm{tot}n}$ at the moment arm r that tends to return the mechanism to its initial state if all valves are closed. Pressurizing the PAM increases contraction (δy), leading to an increased total force $F_{\mathrm{tot}n}$ due to the increased dimension z. 45

Figure 4.4: Pressure change in both cylinder chambers starting from the atmospheric pressure $p_{\mathrm{i}n} = p_{\mathrm{atm}}$. Underpressure is generated in the blue chamber, while air is compressed in the red chamber. 46

Figure 4.5: Theoretical profiles without stiffness increase ($p_{\mathrm{i}n} = p_{\mathrm{atm}}$, $\delta \mathrm{y} = 0$); (a) Force in the cylinder, (b) Moment arm length, (c) Torque of the PEJM. 47

Figure 4.6: Mechanism's stiffness modulation is a process done in n steps. For different valve combinations, different mechanism behavior is obtained. The blue marked cylinder chambers represent underpressure, while the red represents compressed air. When underpressure is generated, air ΔN_n enters the blue chamber by opening valve 2. When the amount of air in the cylinder increases, it can be pumped and stored in the pneumatic muscle by timely opening valve 3. Valve 1 acts as a clutch, by allowing free movement without generating force, as the air passes from one chamber to the other. 48

Figure 4.7: As air is gradually drawn in, the initial cylinder pressure $p_{\mathrm{i}n}$ rises until $p_{\mathrm{u}n}$ equals p_{atm}, indicating no more air can enter the chamber. The pressure can be increased in desired steps n, followed by valve 3 opening to share the pressure with the pneumatic muscle, denoted as $p_{\mathrm{m}n}$. . . . 49

Figure 4.8: The increase in the initial cylinder pressure $p_{\mathrm{i}n}$ increases the torque $T_{\mathrm{tot}n}$, torsional stiffness k_n, and storable energy of the mechanism H_n. . 49

Figure 4.9: The contraction of the pneumatic muscle δy alters the effective length of the cylinder, impacting the force and consequently influencing the torque $T_{\mathrm{tot}n}$, torsional stiffness k_n, and storable energy H_n of the mechanism. 50

Figure 4.10: Experimental platform schematic with components. The control system is highlighted in yellow, output signals in red, and input signals in black. 50

Figure 4.11: Control block scheme of the experimental setup. Sensor signals are inputs to the stateflow, where the algorithm decides when to open/close valves and switch the motor from the repetitive sequence to the standby state. A PD controller with feedforward term achieves the desired motor position, using the encoder signal for feedback. Valve amplitudes are either high or low, but scaled for illustration. 52

Figure 4.12: Actual experimental setup with all parts marked. 52

Figure 4.13: Basic mechanism verification; (a) With all three valves closed, (b) valves 1 and 3 closed and valve 2 open, and (c) valves 1 and 2 closed and valve 3 open. Red line: theoretical values, blue line: measured values. 53
Figure 4.14: Basic mechanism verification with different initial pressures and all valves closed. Blue line: measured torque-deflection profiles, red line: theoretical values. Relative initial pressure in the pneumatic cylinder: (a) 0 bar, (b) 1.46 bar, (c) 1.88 bar, (d) 2.26 bar, and (e) 2.62 bar. . . 53
Figure 4.15: Pneumatic cylinder pressure increase. In (a) motor angle, valve states, and pressure in the cylinder. In (b) measured force and torque with the calculated torsional stiffness and stored energy versus deflection. . . . 54
Figure 4.16: Stateflow algorithm for experiments: (a) Pneumatic cylinder pressure increase, (b) PAM pumping without cylinder pressure increase, (c) PAM as an air tank. 54
Figure 4.17: Two different ways of PAM pumping. In (a) without cylinder pressure increase, and in (b) with two strokes of cylinder pressure increase. Valve 1 is shown in red, valve 2 in green, and valve 3 in blue. 55
Figure 4.18: PAM as an air tank. In (a) with shown motor angle, valve states, pressure in PAM, and contraction. In (b), measured force and torque with the calculated torsional stiffness and energy stored versus deflection. 56
Figure 4.19: PAM inflation by a cordless pump. In (a) the experimental setup is illustrated. In (b) measured force and torque with calculated torsional stiffness and stored energy versus deflection. 57
Figure 4.20: Temperature variation effect on cylinder and PAM pressure. 57
Figure 4.21: Cylinder pressure loss by constant joint rotation over 180 min. 58
Figure 4.22: Graphical comparison of other VSAs with PEJM. 59
Figure 4.23: Application of the PEJM in a knee exoskeleton. Left image source: www.freepik.com 60

Figure 5.1: A person wearing the JSI-KneExo, published in [145]. 63
Figure 5.2: (a) The JSI-KneExo comprises three modular parts: control unit, left-leg exoskeleton, and right-leg exoskeleton. (b) The actuator unit incorporates air solenoid valves, PAM, pneumatic cylinder, force sensor, absolute encoder, shank and thigh lever, and a linear bearing facilitating linear PAM deflection. (c) Pink background highlights control unit components, while light blue denotes exoskeleton (leg side) components; optional insole sensors can be added. 65
Figure 5.3: Pneumatic circuit of the JSI-KneExo. Different valve positions achieve different exoskeleton states. 66
Figure 5.4: Filling compressed air into the PAM with two different pumps, the larger BD-07A-35L and the smaller BD-04A-20L. The equation fitted through measured data has the form: $p_\mathrm{m}(t) = p_\mathrm{max}(1 - e^{-t/k})$. For the larger pump: $p_\mathrm{max} = 6.5$ bar, $k = 2.0713$, and $\mathrm{R}^2 = 0.9921$. For the smaller pump: $p_\mathrm{max} = 3.32$ bar, $k = 1.8302$ and $\mathrm{R}^2 = 0.9969$. 67
Figure 5.5: Model-identification of the PAM DMSP-20-100N-RM-RM. In (a) PAM contraction versus pressure. In (b) PAM volume versus contraction. . . 68
Figure 5.6: (a) Exoskeleton flexed at $\theta = 107^\circ$, the angle where $z = z_0$ for $\varepsilon(p_\mathrm{m} = 3.32, \mathrm{bar})$ contraction. (b) Exoskeleton at $\theta = 0^\circ$ for user standing. . . . 69
Figure 5.7: Theoretical profiles of different physical parameters for the joint rotation from $\theta = 107^\circ$ to $\theta = 0^\circ$. 70
Figure 5.8: Concept of energy recovery in the sit-stand task. The power profile shape and amount are only illustrative. 71

Figure 5.9: Experimental setup: EMG electrodes, reflective markers, and screen for visual feedback. 72

Figure 5.10: Right leg exoskeleton torque during transition, scaled from 100% (sitting) to 0% (standing), with numbered circles indicating different states. 73

Figure 5.11: Pressure sensor measurements over time with state distinctions using numbers. Pump on-off intervals and air recovery periods are marked. . 73

Figure 5.12: EMG recordings of the vastus medialis and gluteus maximus during sitting and standing transfers under assisted and unassisted conditions. 75

Figure 6.1: (a) Overview of the hybrid exoskeleton with labeled parts. In (b) hip exosuit features a tendon-driven actuation with a double-layered pulley, where each layer contains a tendon so that one direction of motor rotation assists one leg and vice versa assists the other leg. In (c) knee exoskeleton comprises three main parts: the control unit, the left leg, and the right leg exoskeleton. The actuator includes a pneumatic cylinder, pneumatic muscle and two air solenoid valves. Compressed air is supplied from the air compressor. Insoles with FSR sensors inside shoes wirelessly transmit signals to the control unit. 79

Figure 6.2: The hip exosuit control involves a high-level controller and a low-level controller. The adaptive oscillator layer in high-level uses the inter-limb hip flexion angle to derive a motor reference position trajectory and identify the gait phase. In the low-level, a PID controller transforms the position error into a motor velocity command. 80

Figure 6.3: The knee controller operates as a Deterministic Finite State Machine (DFSM): The thresholds are individualized for users. Valve1 - clutch valve, Valve2 - torque enabling valve, T - Thresholds, HS - Heel sensor, FS - Finger sensor, θ_{K} - Knee encoder. The subscript "o" denotes the opposite leg. 81

Figure 6.4: An example of knee and hip assistance profiles with the gait cycle. . . . 81

Figure 6.5: Experimental setup during inclined walking at 15° and 3 km/h speed. . 83

Figure 6.6: The protocol consisted of two visits: the familiarization and measurement visit. The second visit was arranged one day following the first. Randomization of conditions was applied during both visits. Upon completing the experiment, the participants were asked the questions shown in the figure. 84

Figure 6.7: Top row illustrates the percentage change in mean RMS EMG from the unassisted condition, averaged across subjects (N=7). Negative values indicate a decrease, while positive values denote an increase in EMG activity. The asterisk (*) below the bars indicates statistically significant differences among conditions ($p < 0.05$). Error bars represent the mean ± standard error. The bottom row presents the normalized EMG activity throughout the gait cycle for a representative subject averaged across steps. 86

Figure 6.8: Average metabolic costs across subjects (N=7) in each condition. The metabolic cost for all assisted conditions is lower when compared to the unassisted condition. Error bars represent the mean ± standard error. The asterisk (*) denotes a statistically significant difference ($p < 0.05$). Arrows show percentage change from unassisted condition. 87

Figure 6.9: The first row shows average kinematic values across subjects (N=7), while the second row shows profiles for a representative subject. (a) Average knee angle RoM; minimum during knee extension, marked with ⓙ, medium during weight acceptance, marked with ⓘ, and maximum during knee flexion in preswing, marked with ⓚ. (b) Average knee angle velocity; (c) Average hip RoM; (d) Average hip angular velocity. In (e), rising knee angle indicates flexion, while falling indicates extension. In (f), positive velocity occurs during knee flexion and negative during extension. In (g), rising hip angle indicates flexion and decreasing indicates extension. (h) Hip velocity is positive during hip flexion and negative during extension. 88
Figure 6.10: User preferences for walking assistance effectiveness compared to unassisted, rated on a scale from 1 (least effective) to 10 (highly effective). The asterisk (*) denotes a statistically significant difference ($p < 0.05$). 89
Figure 6.11: The top row depicts the assistance applied by the knee exoskeleton, while the bottom row illustrates the motor torque profiles for hip assistance. Blue lines represent profiles for individual subjects, with the red line indicating the average torque profile across all subjects. Bar charts represent the average mean peak value ± SD. 89
Figure 6.12: Versatility of Hybrid Rigid-Soft Configurations: (a) Illustration depicting the proposed concept discussed in this chapter, showcasing a rigid knee exoskeleton paired with a tendon-driven hip exosuit. (b) Hypothetical concept demonstrating potential upper limb configurations, including a rigid elbow exoskeleton coupled with a tendon-driven shoulder exosuit. 93

List of Tables

Table 3.1: Technical specifications Pneumatic Quasi-Passive Variable Stiffness Mechanism . . . 37
Table 3.2: Technical specifications of recent Quasi-Passive Ankle Exoskeletons . . . 38

Table 4.1: Parameters of the proposed PEJM . . . 58
Table 4.2: Comparison with different variable stiffness actuators . . . 59

Table 5.1: Maximum Actuation Frequency with and without Energy Recovery . . . 75

Table 6.1: Parameters of the Hybrid Exoskeleton . . . 82

Abbreviations

10MWT	10-meter walk test
6MWT	6-min walk test
ANOVA	Analysis of Variance
ARIES	Assistive Robotics and Interactive Exosuits
AwAS	actuator with adjustable stiffness
DAQ	Data Acquisition
DoF	Degree of Freedom
EMG	Electromyography
FMA	Fugl-Meyer assessment
IMU	Interial Measurement Unit
LiPo	lithium-polymer battery
MACCEPA	mechanically adjustable compliance and controllable equilibrium position actuator
MVC	Maximum Voluntary Contraction
N/A	Not applicable
PAM	Pneumatic Artificial Muscle
PC	Personal Computer
PCB	Printed Circuit Board
PEJM	Pneumatic Exoskeleton Joint Mechanism
RMS	Root Mean Square
RoM	Range of Motion
SEA	Series Elastic Actuator
TFL	Tensor Fasciae Lata
TUG	timed up and go test
VSA	Variable Stiffness Actuator
VL	Vastus Lateralis
VM	Vastus Medialis

Glossary

Active Exoskeletons: Exoskeletons equipped with powered actuators or motors that actively assist or augment the wearer's movements, providing additional strength, endurance, or mobility support.

Air Harvesting: The process of accumulating air mass into the actuator through the utilization of a vacuum.

Backdrivability: Refers to the ability of a mechanical system, such as an actuator, to be driven manually or by external forces without damaging its internal components.

Energy Regenerating Actuator: An actuator that not only provides mechanical assistance but also recovers and stores energy during certain phases of operation, allowing for improved energy efficiency and prolonged usage without external power sources.

Energy Storing Capacity: In the context of compliant mechanisms, it refers to the ability to store mechanical energy, typically achieved through the compression of elastic components, and often utilized in various applications such as energy-efficient locomotion or impact absorption.

Exoskeletons: External mechanical structures worn by humans to augment or enhance physical capabilities, typically designed to assist with movement, support, or protection, often utilized in medical rehabilitation, military applications, and industrial settings.

Pneumatic Artificial Muscle (PAM): A pneumatic actuator that contracts when pressurized air is introduced, mimicking the function of biological muscles.

Quasi-Passive Exoskeletons: Exoskeletons that primarily rely on mechanical or passive elements for assistance, with minimal active control of clutches for engaging or disengaging assistance.

Variable Stiffness: In the context of exoskeletons, it refers to a property where the stiffness of the mechanism or actuator can be adjusted or modified, usually to accommodate various tasks or environments.

Chapter 1

Introduction

The field of wearable robotics has emerged as a promising avenue for enhancing human capabilities and addressing motor challenges in individuals with impairments, amputations, or even those who are healthy. Among the diverse range of wearable robotic devices, such as robotic prostheses and supernumerary robotic limbs, exoskeletons stand out as innovative technologies designed to be worn on the body and existing body limbs, attached to either the upper or lower limbs, offering potential benefits for mobility, strength, and rehabilitation [1]. These devices can be classified according to various criteria, but one of the most notable is their application. Exoskeletons find applications across a diverse range of sectors, among which the most common include medical, consumer, occupational, and military contexts. Some commercial examples of different application exoskeletons are shown below in Figure 1.1.

Figure 1.1: (a) Medical: ABLE by ABLE Human Motion (lower-limb active exoskeleton), ArmeoSpring by Hocoma (for arm rehabilitation), ReWalk exosuit (for ankle rehabilitation). (b) Consumer: FitExo by Enhanced Robotics, Elevate pneumatic exoskeleton by ROAM Robotics (enhances skiing endurance), GEMS (Gait Enhancing and Motivation System) by Samsung (for haptic feedback in gaming). (c) Occupational: Ottobock Paexo, Atoun by Panasonic, CarrySuit by Auxivo, Cray by German Bionic (enhance endurance during lifting). (d) Military: PowerWalk by Bionic Power, for electrical energy harvesting, and Onyx by Lockheed Martin for increased weight carrying.

Medical exoskeletons provide support and assistance to users with conditions such as spinal cord injuries, stroke, or neurological disorders to regain mobility and independence by supporting them in standing, walking, and performing daily tasks [2]–[5]. In rehabilitation scenarios, by leveraging the brain's neuroplasticity, these devices can impose correct walking patterns and help in relearning lost movements [6]–[8]. Additionally, by offering personalized rehabilitation options, they enable healthcare professionals to customize treatment plans to suit each patient's unique needs. Advancements in technology allow modern exoskeletons to monitor physiological data, track progress, and offer real-time feedback, ultimately optimizing rehabilitation outcomes. Often, medical exoskeletons are combined with virtual reality and augmented reality technologies to make the patient's rehabilitation process more interesting [9].

Consumer exoskeletons are wearable devices designed for everyday use, distinct from those intended for medical, occupational, or military purposes. Examples can include fitness exoskeletons [10]–[12], skiing braces that support weakened muscles such as the Elevate exoskeleton by ROAM Robotics, and gaming exoskeletons that offer enhanced haptic feedback, such as GEMS (Gait Enhancing and Motivation System) by Samsung. For instance, Samsung's GEMS exoskeleton can simulate walking through viscous fluids like water by applying resistive forces to the user's legs. These devices can target various limbs, from the upper to the lower limbs. Additionally, haptic gloves have recently garnered attention from large companies such as Meta in their Reality Labs Research division [13].

Occupational exoskeletons can be applied across various sectors, such as in industrial settings [14]–[17], where workers frequently face the risk of lifting heavy loads, posing potential costly injuries for both the worker and the company [18], [19]. Commercialized examples include Ottobock Paexo, which offers shoulder assistance, and CarrySuit by Auxivo, designed to transfer payload weight to the user's hips, thereby alleviating critical joints like the wrist, elbow, shoulder, and spine and relieving muscles in the torso and upper extremities. Other industrial exoskeletons incorporate motors that actively produce torque, such as Atoun by Panasonic and Cray by German Bionic. Occupational exoskeletons often provide targeted support to areas such as the lower back or shoulder joints [17]–[19]. Additionally, they can be utilized by healthcare providers or surgeons who may need to maintain their arms in a static position for extended periods, leading to fatigue.

Military exoskeletons are designed with the idea of empowering soldiers by allowing them to carry more of the weight normally caused by their mission-critical equipment. This field of research often appears in the literature as weight-bearing exoskeletons [20]–[24]. A systematic literature review of exoskeletons in defense and security use cases was made by Farris et al. [25]. Some commercialized devices also exist, such as PowerWalk by BionicPower that harvests energy to generate electricity and Onyc by Lockheed Martin for support during heavy-weight carrying.

Beyond their categorization by application, exoskeletons can be primarily distinguished as passive, quasi-passive, or active based on the actuation technology. Passive exoskeletons rely on mechanical elastic components, such as springs, to provide support and assistance without the use of powered actuators [26]–[32]. In some cases, they may incorporate passive clutches to store and release energy during different phases of a task. Sometimes clutches can also be powered and actively controlled. In the literature, exoskeletons featuring powered components like clutches or sensors are referred to as quasi-passive exoskeletons [24], [33]–[36]. Here, it is important to note that despite the inclusion of some powered components, quasi-passive exoskeletons still depend primarily on fully passive actuators for their operation. On the other hand, active exoskeletons incorporate powered actuators and sensors to augment the user's strength and mobility, offering more dynamic support for activities demanding greater assistance and versatility [37]–[45].

While certain sectors, notably the medical field, have adopted exoskeletons, others still face challenges, whether technical or nontechnical, that must be overcome before adoption could happen. Users whose functions or daily activities can experience significant improvement are more inclined to embrace the technology. In healthy subjects, whether in consumer, occupational, or military exoskeletons, comfort is crucial as it significantly influences user acceptance, and discomfort can potentially lead to rejection. However, comfort is closely tied to the actuation and mechanical design of the exoskeleton due to its weight. Additionally, if the control algorithm does not seamlessly synchronize with the user, it can disrupt comfort levels. In general, the open challenges in wearable robotics emerge from the three main pillars: Actuation, Control, and Ergonomics. These pillars are interconnected, influencing and shaping one another. A brief overview of each of these pillars is provided below, followed by a summary of the main challenges.

Actuation: Actuators play a key role in the functionality and performances of exoskeletons, as they are the driving force behind their movement and assistance. Different types of actuators are used in the design of exoskeletons, with the most common including electromechanical [37]–[40], pneumatic [41], [43], [45]–[47], and hydraulic systems [2], [48]. Each actuator type presents unique advantages and challenges, guiding their selection based on the specific requirements of the exoskeleton design and intended application. Electromechanical actuators, such as DC motors with gears, offer precise control and high power output, making them suitable for dynamic movements and load-bearing tasks in exoskeletons. Pneumatic actuators, like pneumatic artificial muscles (PAMs) and pneumatic cylinders, provide high power density and inherent compliance ideal for exoskeletons, albeit with trade-offs in portability and controllability [49]. Hydraulic actuators excel in applications requiring high force output and robustness, such as industrial exoskeletons, where they provide substantial lifting capabilities and endurance; however, they are heavy due to their use of oil.

Control: The control of exoskeletons is intricately tied to the actuation mechanism employed. Depending on the actuation method whether electromechanical, hydraulic, or pneumatic, control algorithms exhibit significant variation. The task of these algorithms is to coordinate the interaction between the user and the device, ensuring seamless movement and functionality while minimizing user effort and fatigue. From simple position control to more advanced impedance and force control strategies, the design of control algorithms plays a crucial role in optimizing performance, stability, and user comfort [50]. Moreover, advancements in sensor technology and machine learning have enabled the development of adaptive control strategies, allowing exoskeletons to autonomously adjust to the user's needs and environment in real-time [51].

Ergonomics: Just as even the most stylish shoes are left unworn if uncomfortable, exoskeletons, despite their advanced actuation and control features, risk rejection if their attachment points to the human body lacks ergonomic design or if a design is bulky. Thus, ergonomics holds a pivotal role in ensuring the comfort, safety, and overall efficacy of wearable devices. This entails studying biomechanics and anthropometry to tailor exoskeletons to diverse body types and movements, ensuring ergonomic compatibility across a broad range of users. Additionally, researchers investigate the effects of prolonged exoskeleton use on user convenience, pressure on the skin, fatigue, and overall performance to inform iterative design improvements [52].

1.1 Ongoing Challenges

Although rapid technological advancements from both industry and academia drive the field forward and enable emerging exoskeletons to enter the market, certain technological aspirations remain beyond current reach, while others seem within grasp but necessitate further research and development. Listed below are areas within exoskeleton research that persist as major ongoing challenges, ranked in descending order of importance according to the author's subjective judgments:

1. **The field remains heavily reliant on actuation technology that has persisted for nearly two centuries, the electric motor, thus innovations on this topic are urgent**. There is a demand for actuators that resemble biological muscles [53], particularly those that are intrinsically compliant or fully soft, capable of adjusting stiffness without complex mechanisms, and have a high level of integration with sensors in one component so that they can be comfortably embedded in clothing. Existing actuators that mostly resemble muscles (Pneumatic Artificial Muscles and Pneumatic Inflatable Actuators), often demand large air tanks. One promising solution to this challenge is biomechanical energy harvesting [54] and innovative methods for delivering pneumatic energy [55], [56].
2. **The mechanical design requires simplification compared to current norms in the field, alongside the improvement of attachment points**. Common mechanical designs typically involve rigid frames with actuators aligned with human joints, however, trends are moving toward fabric-based designs with the goal of reducing weight on the distal limbs for better adaptation to the human body [57]. Yet, challenges remain in effectively attaching a robot and transmitting forces to the human body, demanding urgent systematic investigation and innovative approaches, such as hybrid rigid-soft systems. Besides innovative exoskeleton designs, the advances in this regard could also be enabled by the development of novel materials [58].
3. **Hierarchical control where the high-level algorithms should infer human intentions as we need exoskeletons to be increasingly versatile**. This domain is advancing in several ways, e.g. by taking into account not only the user and the exoskeleton but also the environment through the use of cameras [59], [60]. Another seemingly more challenging approach is to infer intent directly from the human brain via electrodes [61]. Moreover, there is growing interest in human-in-the-loop controllers, which allow exoskeleton parameters to be optimized based on real-time data from the user where different objective functions can be used also to improve the interaction [51], [62].
4. **Benchmarking of exoskeletons and quantitative indicators of performance other than in the laboratory settings**. This is an under-addressed topic but one in need of thorough exploration. This aspect is less related to technological innovations, however crucial for the usability of exoskeletons [63].

Furthermore, there exist other challenges that seem comparatively more approachable or are commonly encountered in robotics:

1. Novel sensors that can be embedded into clothing have the potential to enhance overall comfort, performance, and control with human-in-the-loop aspects [64], [65].
2. Enhancing autonomy via advancements in battery technology is a significant consideration, albeit a prevalent challenge across robotics [66].
3. Ensuring the cost-effectiveness and affordability of exoskeleton technology is crucial for fostering broader adoption [67].

4. Prioritizing safe operation remains a vital aspect of the design process [1].
5. The customization of exoskeletons to accommodate individual needs in terms of size, control, and other parameters [40].

Why is it hard to engineer an actuator similar to biological muscles?

Most of the design challenges revolve around actuation, leading the author to prioritize actuation as the most crucial aspect. The concept of an actuator resembling biological muscles has been a longstanding goal in robotics as no actuator can satisfy all the actuation requirements [53]. The actuation continues to be predominantly influenced by a technology that has been in existence for nearly two centuries, the electric motor. Biological muscles possess the unique ability to adjust their stiffness, allowing for safe interaction with humans and adaptation to varying environments [68]. The compliance is attributed to the viscoelastic properties of muscles, including the ability to change their moduli. Humans utilize the entire muscle structure's morphology, material, and constraints to adapt stiffness and damping to unfamiliar environments. Moreover, biological muscles exhibit a high level of integration, where actuation, transmission elements, proprioceptive sensing, control circuits, and viscoelastic properties are seamlessly integrated into one material architecture [53]. Therefore, differences in the actuation principle between robot actuators and biological muscles still exist, but we are on the right way to create artificial muscles intrinsically similar to biological, whose actuation can be based on pneumatic, thermal, and electrical inputs [53]. Actions directed towards addressing the complexities associated with pneumatic artificial muscles and pneumatic inflatable actuators, including the exploration of innovative methods for delivering pneumatic energy (such as through chemical or electrochemical reactions), are likely to significantly influence the field in the long term.

Why mechanical design requires simplification?

Exoskeletons are often complex in their mechanical design, however, they must strike a balance between functionality and simplicity to ensure minimal weight and, crucially, user comfort and minimal invasiveness to avoid rejection. Furthermore, complexity is responsible for increasing cost, weight, and size. The time required for putting on and taking off the device is also a significant consideration. Research challenges in this domain aim to innovate lighter and simpler structures that enhance comfort, reduce the time needed for putting on the device, and offer greater freedom of movement. Besides traditional exoskeletons with rigid structures known for their high power, a novel concept of soft exoskeletons emerges that resembles everyday clothes, making them increasingly popular in research. These exoskeletons utilize soft actuation mechanisms, offering enhanced comfort, and reduced weight, and are typically fabric-based, and thus better conform to the human body. Continued advancements in soft materials hold the promise of driving further innovation in exoskeleton design [69].

What can high-level controllers do better than what exists?

Humans naturally adjust joint torques and movement patterns based on environmental signals, such as when approaching stairs for ascent or descent, using visual input. Similarly, when lifting objects, humans intuitively gauge the required power. However, inferring human intentions for exoskeletons can be challenging but may necessitate adaptation to various environments, requiring movement and torque adjustments and locomotion changes. A high-level controller is essential for interpreting human intentions and generating and adjusting reference actions to ensure that the desired task is executed according to the user's intentions and assisted as intended by the exoskeleton. In the field, very little effort has been made in recognizing the environment around the user, as mostly the focus has been on the user and the exoskeleton. Further recent investigations often put human-in-the-loop meaning that the exoskeleton can adapt parameters while measuring the effects on humans such as energetic cost, kinematics, or even interaction forces or user preference potentially improving comfort and user satisfaction [51]. However, some methodologies require long measurement times that increase the rate of dropout and induce muscle fatigue. Accordingly, future research in the robotics field would benefit from combining human-in-the-loop with available musculoskeletal models, since these models allow for the simulation of an objective function while customizing control parameters using online measurements directly from participants. Moreover, as new soft robotic actuators emerge, there is a growing effort among research groups in academia and industry to address the challenges of novel compliant controllers and nonlinear modeling [70], [71].

Why are quantitative performance indicators essential for progress in the field?

The field of wearable robotics lacks standardized quantitative indicators of performance, leaving researchers questioning what parameters to measure to assess a device's effectiveness. Benchmarks provide a quantitative assessment, enabling the evaluation of system impact using standardized units. Currently, lab evaluations often involve measuring parameters like muscular activity, metabolic cost, or joint power in healthy subjects to assess exoskeleton performance, often hypothesizing similar effects on impaired subjects. However, other benchmarks, such as consideration of adaptability, interaction ability, or dependability, are needed to achieve further progress. Other approaches are assessing the functional improvements achieved with exoskeletons in impaired individuals, and evaluating the user's ability to accomplish specific tasks [50]. A good example of a wearable robotics competition is Cybathlon, where such tests are performed. These might involve for example the 10-meter walk test (10MWT), the 6-min walk test (6MWT), the timed up and go (TUG) test [72], or the Fugl-Meyer assessment (FMA) [73].

1.2 Purpose of the Dissertation

In general, the purpose of this dissertation is to explore and invent novel pneumatic actuation mechanisms with variable stiffness and corresponding control algorithms and implement them in a newly developed innovative rigid-soft lower-limb exoskeleton prototype for partial assistance. It will also explore biomechanical energy harvesting and novel methods for delivering pneumatic energy, and thus advance the current state-of-the-art.

Specifically, first, it seeks to develop a novel type of lightweight quasi-passive pneumatic mechanism and method that enables stiffness modulation without an external air supply, which has been identified as one of the major bottlenecks. Such a mechanism could improve devices that currently rely on single-stiffness mechanical springs. The dissertation further seeks to explore energy harvesting methods using the developed mechanism. After developing and validating a quasi-passive pneumatic mechanism, the dissertation aims to bring a whole prototype of a fully portable exoskeleton that in addition to the quasi-passive mode can operate in active mode. This multi-modal operation could increase the energy efficiency in pneumatic exoskeletons. With the same prototype, the dissertation also seeks to devise a methodology for simultaneous human assistance and more efficient energy recovery than with existing actuators for lower limb exoskeletons. Finally, the dissertation will investigate the synergies between tendon-driven electromechanical actuation and pneumatic actuation, aiming to bring the hybrid rigid-soft multi-joint assisted device that could simplify the mechanics and optimize the functionality and effectiveness.

Unlike targeting a specific group of applications (e.g., rehabilitation or impaired individuals), the developed exoskeleton prioritizes advances in the underlying technology and is tested on healthy subjects. As a result, the technology has the potential to enhance a broad spectrum of wearable devices tailored for specific applications, possibly extending to other types of legged robots.

1.3 Goals of the Dissertation

Four primary goals have been set to realize the purpose of this dissertation.

G1. Develop and experimentally evaluate a portable pneumatic quasi-passive variable stiffness mechanism featuring a novel stiffness modulation method that operates without an external air supply by utilizing a vacuum to harvest the air and adjust stiffness. The mechanism must be compact and lightweight so that it can be installed in the exoskeleton.

G2. Integrate the developed quasi-passive variable stiffness mechanism into a novel exoskeleton joint prototype, incorporating additional inflatable pneumatic components, to serve as a soft reservoir for harvested air and further influence joint stiffness. Experimentally validate the exoskeleton joint prototype on the experimental device.

G3. Develop an entire bilateral portable pneumatic knee exoskeleton with multiple modes of operation, among which the most important are quasi-passive and active. The same actuator should be capable of operating in multiple modes. The quasi-passive mode should be achieved by utilizing the previously developed joint, and active by including a portable air supply. These multimodalities are intended to function simultaneously during tasks and improve the energy efficiency in pneumatic exoskeletons.

G4. Extend the exoskeleton's functionality to provide multi-joint assistance for the lower limbs by integrating a hybrid actuator, consisting of a soft tendon-driven design for hip joint assistance and a rigid design for knee assistance. Demonstrate the advantages of this configuration through experimental studies on humans.

1.4 Hypothesis

Aligned with the dissertation goals, we have formulated the following hypotheses:

H1. The newly developed mechanism will function as a nonlinear variable stiffness spring when engaged and remain transparent and fully backdrivable when disengaged. Stiffness modulation will be achieved through efficient air harvesting. Experimental results will showcase improved functionalities and technical specifications compared to current quasi-passive mechanisms.

H2. The exoskeleton joint will efficiently accumulate and store compressed air in the soft air tank, thereby additionally adjusting stiffness. The stored air will be reusable. The exoskeleton joint prototype will excel in energy density compared to similar mechanisms.

H3. The entire exoskeleton prototype will reduce muscle activity in both active and quasi-passive modes. Moreover, experimental validation will demonstrate a reduction in exoskeleton energy consumption when combining two operational modes.

H4. Assisting multiple joints will result in lower human metabolic costs compared to assisting a single joint. In addition, the assisted muscles will exhibit lower muscle activation with minimal changes in kinematics.

1.5 Structure of the Dissertation

The dissertation is structured in the following way.

Chapter 2 provides an overview of the state of the art in wearable robotics, with a particular emphasis on lower-limb exoskeletons. It provides an in-depth review of the various types of exoskeletons, the actuators employed, and the control strategies, and concludes by proposing methodologies on how to the key issues in the field are improved in the dissertation.

Chapter 3 introduces the quasi-passive pneumatic variable stiffness mechanism in relation to goal **G1** and hypothesis **H1**. It begins with the theoretical concept and pneumatic design, followed by a mathematical description of stiffness modulation. Subsequently, the physical prototype is presented, accompanied by a detailed description of the experiments. The chapter then outlines the results, followed by an application, comparison, and discussion. Finally, concluding thoughts are provided to wrap up the chapter.

Chapter 4 presents the pneumatic exoskeleton joint mechanism (PEJM), building upon the fundamental principles established in the previous chapter and is related to goal **G2** and hypothesis **H2**. This mechanism incorporates additional components, including pneumatic artificial muscle (PAM). The chapter begins by detailing the mechatronic design and operational principles. Subsequently, it explores a novel method of stiffness modulation. Following this, an experimental evaluation on the setup is conducted, and the results are presented alongside a comparative analysis with alternative approaches. The chapter concludes with final reflections on the findings.

Chapter 5 delivers the entire pneumatic portable knee exoskeleton and is associated with **G3** and hypothesis **H3**. The chapter begins with a mechatronic design, followed by an examination of its pneumatic multimodalities. Of particular significance is the concept of energy recovery, which is elaborated upon mathematically. Subsequently, a pilot study involving a healthy subject is conducted, and the results are discussed in the context of simultaneous energy recovery and human assistance. The chapter concludes with final reflections on the implications of the findings.

Chapter 6 delves into the hybrid rigid-soft and pneumatic-electromechanical exoskeleton designed for multi-joint lower limb assistance, associated with **G4** and hypothesis **H4**. The chapter begins by detailing the actuation configuration and the decoupled control of both joints (hip and knee). Human studies are conducted in the experimental environment, together with data collection and statistical analysis to examine the impact on muscular activity, metabolic cost, and kinematics. Subsequently, the results are thoroughly discussed, leading to the conclusion of the chapter.

The dissertation conclusions are presented in Chapter 7.

Chapter 2

Literature Review

This chapter provides an overview of lower limb exoskeletons, encompassing the actuation, various types, and typical control algorithms. In the end, it introduces the methodologies and innovations proposed in this dissertation to address the deficiencies. Given the dissertation is concentrated on lower limb exoskeletons for partial assistance, the literature review is specifically directed toward this field.

2.1 Lower Limb Exoskeletons

Robotic lower limb exoskeletons can apply assistive torque, and thereby reduce or, in certain scenarios, entirely replace the exertion required by leg muscles, thereby aiding individuals during activities such as walking, standing up, sitting down, and more. The manner and configuration of assistive motion and torques vary depending on the specific application. There are two primary categories of exoskeletons designed to aid in walking: those intended for complete mobilization and those for partial assistance. In Figure. 2.1

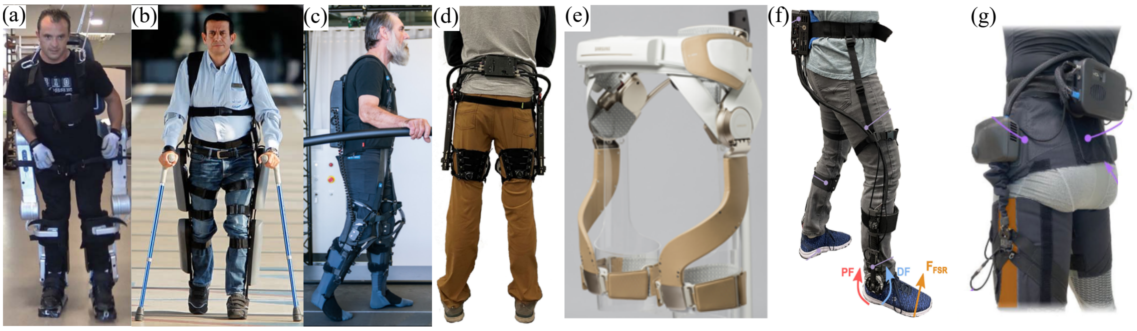

Figure 2.1: Examples of lower limb exoskeletons. (a) and (b) depict complete mobilization lower limb exoskeletons, while (c) through (g) show partial assistance exoskeletons. In (a), the ATALANTE exoskeleton by Wandercraft weighs 80 kg and features 12 actuated joints [74], [75]. (b) showcases the ReWalk Personal Exoskeleton, weighing 20.4 kg with two actuated joints per leg [76], [77]. (c) Myosuit by Myoswiss AG, weighs 4.5 kg and is designed for knee extension assistance in patients with motor disorders [3]. (d) Hip exoskeleton for walking, running, and stair ascent weighs 3.5 kg [37]. (e) Samsung hip exoskeleton for assisting healthy human subjects, reducing the metabolic cost of walking, and weighing 2.4 kg [12]. (f) Ankle exoskeleton aimed at improving walking in individuals with cerebral palsy, weighing 2.8 kg [78]. (g) Tendon-driven exoskeleton (a concept known as an exosuit) provides hip assistance and weighs 2.87 kg [79].

examples including (a) and (b) are complete mobilization exoskeletons, while (c) through (g) show partial assistance exoskeletons. Exoskeletons aimed at complete mobilization are engineered to facilitate leg movement for individuals experiencing significant motor impairment or motor disorders, commonly observed in cases of spinal cord injury (SCI). These devices have been on the market since 2011 when ReWalk (ReWalk Robotics, Israel) was introduced commercially. These exoskeletons require actuators with high torque capability as they are responsible for providing the entire torque necessary for movement. Some examples of such exoskeletons are given in [74]–[77], [80]–[84]. Partial assistance exoskeletons generally have a lighter design with less powerful actuators and target different less severe impairments such as decreased stamina due to aging, weakened strength or coordination resulting from incomplete spinal cord injury, stroke, neurodegenerative diseases, and similar conditions. These devices can also assist the gait of healthy people, which can be useful for endurance augmentation purposes. Some examples of partial assistance exoskeletons are found in [3], [12], [26], [37], [78], [85], [86].

2.1.1 Energy Flow Between Humans and Exoskeletons

Human joints exhibit the ability to both generate and absorb energy, influenced by the coordinated action of muscle pairs engaging in concentric and eccentric contractions. The activation of muscles results in the production of joint torques, thus governing joint motion. Joint power is the product of the joint torque and the joint angular velocity. A positive value indicates power generation, which reflects concentric muscle activation, and a negative value, in contrast, indicates power absorption, which reflects eccentric muscle activation [87]. Taking this into account, various energy exchange mechanisms between humans and exoskeletons exist, occurring during both positive and negative joint power

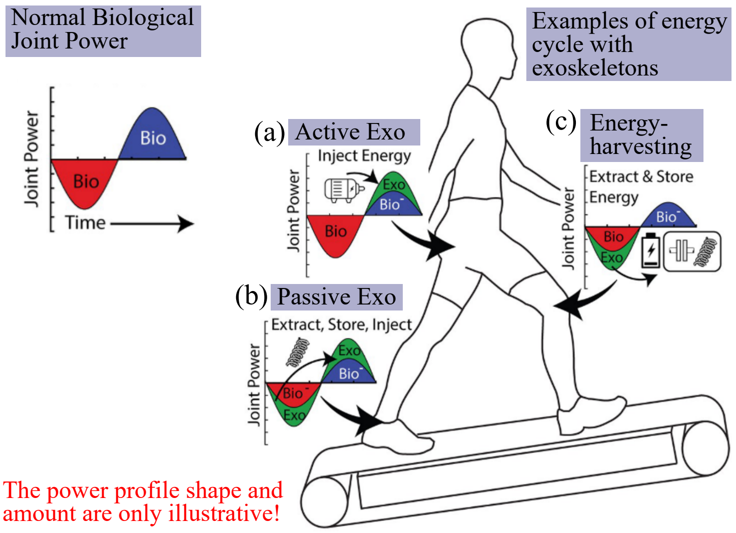

The power profile shape and amount are only illustrative!

Figure 2.2: Three examples of the energy cycle between humans and exoskeletons. Negative joint power generated by human joints is depicted in red, positive power is shown in blue, and exoskeleton power is represented in green. (a) Active exoskeletons inject energy at the joint during the positive power intervals of the gait via an actuator. (b) Passive exoskeletons store energy during the negative power intervals and immediately return it to the same joint through elastic components. (c) Energy-harvesting exoskeletons extract energy from the joint during the negative power intervals of the gait and generate electricity or compressed air in the case of pneumatic exoskeletons. The figure is adapted from [54].

intervals. Three instances of energy flow between humans and exoskeletons are depicted in Fig. 2.2. For instance, Fig. 2.2a illustrates active exoskeletons delivering power via actuators at joints during the positive joint power phase of the gait cycle. In Fig. 2.2b, passive exoskeletons store energy during negative joint power intervals and return it to the joint to assist during positive joint power intervals, typically accomplished through elastic components. Figure 2.2c showcases energy-harvesting exoskeletons capable of extracting and storing energy during negative joint power intervals to charge the batteries using energy-regenerating actuators. In the case of pneumatic exoskeletons, this process can involve accumulating compressing air. Understanding these biomechanical principles is crucial for comprehending the following reviews on various types of exoskeletons.

2.1.2 Active Exoskeletons and Actuators

Active exoskeletons are designed to augment or restore human capabilities by integrating sensors and powered actuators that deliver forces or torques to human joints. They are equipped with electronic circuits, where the control algorithms run and continuously monitor and adjust assistance levels in real-time. The power for these actuators is sourced from various power sources, including batteries for electromechanical actuators or different pumps for pneumatic and hydraulic actuators.

2.1.2.1 Electromechanical Actuators

One of the most common actuator types in active exoskeletons is electromechanical actuators, typically comprising an electric motor and gear transmission to amplify torque. These actuators convert electrical energy into mechanical motion, enabling precise control over force or torque. Electromechanical actuators offer efficient and adaptable assistance, making them suitable for a wide range of exoskeleton applications. Examples of exoskeletons for partial assistance with electromechanical actuators are given in Figure. 2.3. Backdrivability is another crucial aspect of actuators, enabling the transmission of external forces back through the system to the motor. This feature enables bidirectional interaction between the exoskeleton and the user, facilitating natural movement and proprioceptive feedback. Typically, high-reduction gears lack backdrivability. However, a concept gaining traction in recent literature is a quasi-direct drive, wherein a small reduction gear is added to an electric motor that already possesses notable torque, such as in [89].

2.1.2.2 Pneumatic Actuators

Another commonly used type of actuator in active exoskeletons is pneumatic actuators, which operate by utilizing compressed air. These actuators offer high power density and inherent compliance, along with high backdrivability, making them well-suited for exoskeleton applications. However, they come with certain trade-offs in terms of portability and controllability. In wearable robotic applications, various portable pneumatic energy sources are employed, ranging from large stationary air compressors e.g. in [43], [45], [91], [93], to more portable options like small air pumps [41], [42], [94] which can be further configured either in parallel for high flow rates or in series for high-pressure output [95]. These air pumps are available in different designs, including diaphragm pumps and piston pumps, capable of delivering high pressure but possibly generating noise. Alternatively, electro-pneumatic pumps operate quietly but have limitations in the pressure they can generate [56]. Nonetheless, they appear to be a promising avenue for future advancements in pump technologies. Figure 2.4 shows examples of pneumatic actuators in lower limb exoskeletons for partial assistance.

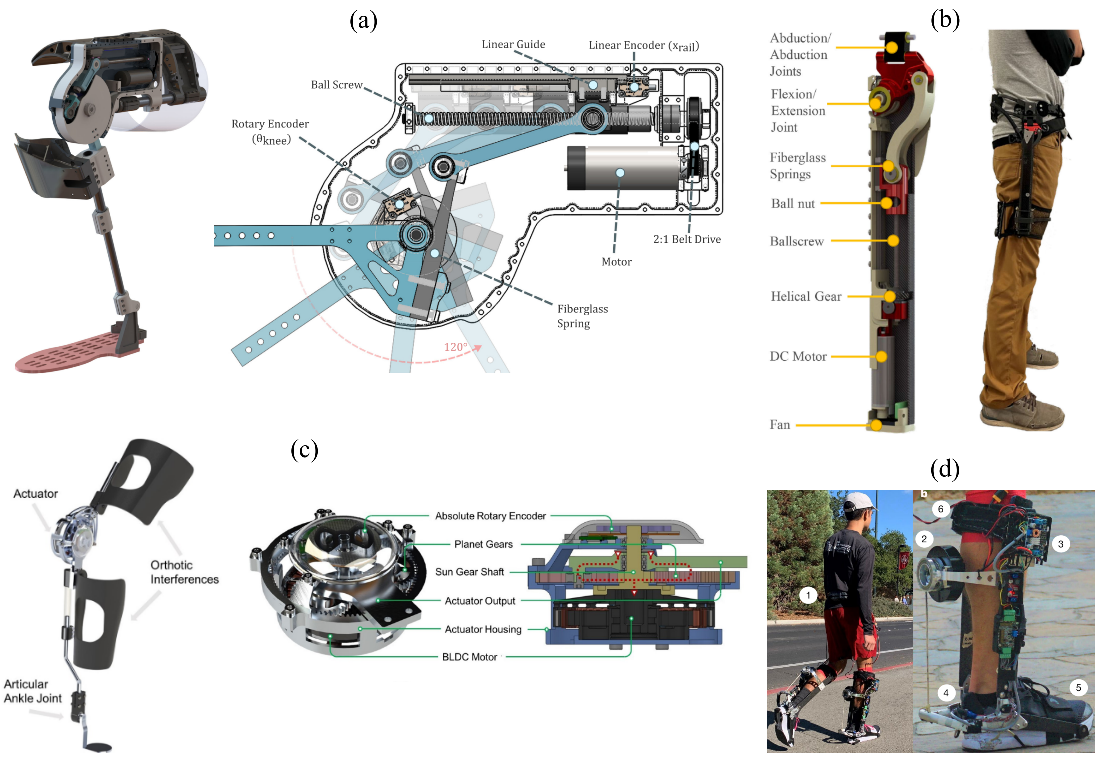

Figure 2.3: Examples of electromechanical actuators in lower limb exoskeletons for partial assistance: (a) Transmission system with belt, ball screw, and levers for mechanical advantage at the knee joint [38]. (b) Combination of helical gear, ballscrew, and fiberglass springs for torque amplification at the hip joint [37]. (c) Planet gears on the output of a BLDC motor in a knee exoskeleton [88]. (d) Actuator denoted with number two, with a rope wound around the output pulley for ankle joint assistance [40].

2.1.2.3 Hydraulic Actuators

The hydraulic actuators appear less frequently in exoskeletons because of their higher weight and complexity compared to pneumatic and electromechanical alternatives. Additionally, they require more maintenance due to the potential for fluid leakage and hydraulic component wear. However, hydraulic actuators offer high power density and robustness, making them suitable for applications where high forces and torques are required. One notable example of a commercialized hydraulic knee exoskeleton is the Ottobock C-Brace® [2], [96], depicted in Fig. 2.5. This exoskeleton operates hydraulically but is passive, with adjustable damping only. Its purpose is to prevent knee drop resulting from impaired knee extensor muscle groups, commonly observed in neurological conditions.

2.1.2.4 Variable Stiffness

Variable stiffness in actuators refers to the ability of an actuator to change its stiffness, which is essentially the relationship between torque and deflection. In exoskeletons, variable stiffness actuators are often used to mimic the compliance and adaptability of human muscles and tendons. By adjusting the stiffness of the actuator, it can better replicate the behavior of biological muscles, allowing for smoother and more natural movements. This capability is particularly useful in exoskeletons where the user's movements may vary in speed, force, or direction, requiring adaptable levels of support and resistance.

Variable stiffness is a feature commonly found in electromechanical actuators, and to a lesser extent, in pneumatic ones. The upcoming section will discuss the current state-of-the-art in electromechanical variable stiffness actuators followed by pneumatic actuators.

2.1.2.4.1 Electromechanical Variable Stiffness: To understand variable stiffness actuators, it's crucial to grasp the concept of Series Elastic Actuators (SEAs). These actuators incorporate a compliant element, typically a spring, in series with the output linkage. This configuration enables the actuator to store and release mechanical energy, providing inherent compliance and shock absorption. SEAs offer several advantages, including enhanced safety, energy efficiency, and robustness in interactions with the environment or human users. They were first introduced by Pratt et al. [98]. However, SEAs have fixed stiffness, which has led to the development of Variable Stiffness Actuators (VSAs), an innovative actuator design that allows for adjustable stiffness properties during operation. Unlike traditional actuators with fixed stiffness, VSAs enable dynamic changes in stiffness based on task requirements. Figure 2.6 shows the schematic concept of a stiff actuator, series elastic actuator (SEA), and variable stiffness actuator (VSA).

Several mechanisms exist for adjusting stiffness, typically powered by a secondary motor alongside the primary one. This is extensively covered in the review paper by Wolf et al. [99]. Common approaches are illustrated in Fig. 2.7. They often involve alter-

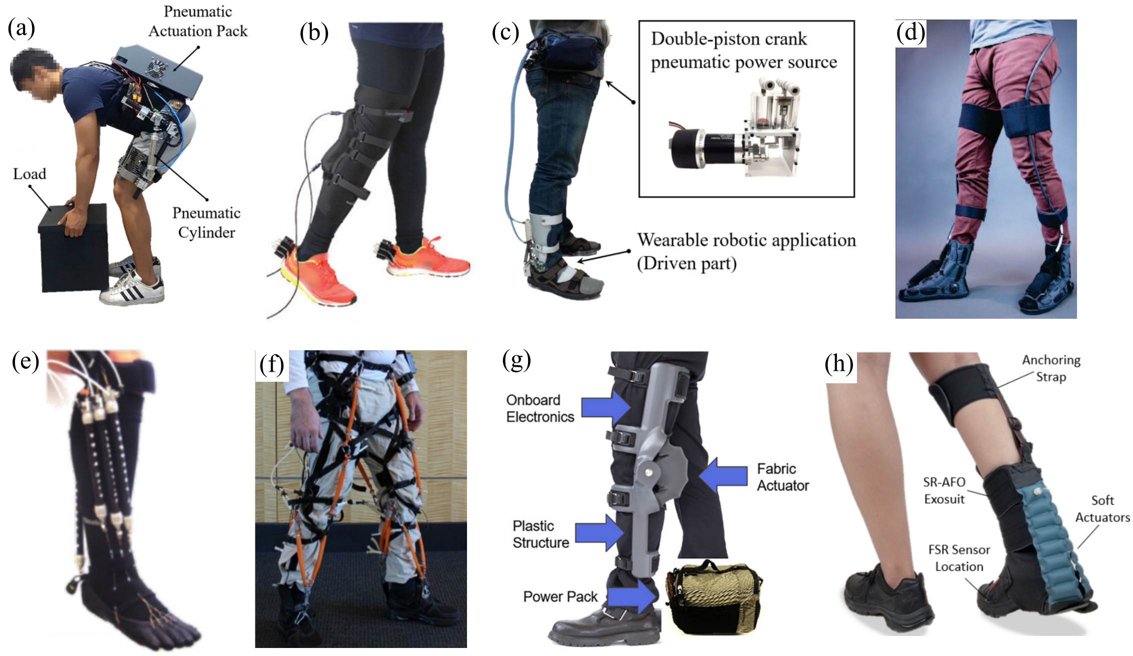

Figure 2.4: Examples of pneumatic actuators in lower limb exoskeletons for partial assistance: (a) Portable hip exoskeleton with pneumatic cylinder [41]. (b) Soft inflatable actuator for knee assistance [90]. (c) Pneumatic ankle exoskeleton with double-piston crank power source [42]. (d) Exoboot, a soft inflatable robotic boot providing ankle assistance [43]. (e) McKibben Pneumatic Artificial Muscles (PAMs) in bioinspired design [91]. (f) Custom McKibben-style pneumatic actuators for hip, knee, and ankle assistance [46]. (g) Commercialized pneumatic knee exoskeleton with fabric actuator from ROAM Robotics [92]. (h) Robotic ankle-foot orthosis with inflatable actuator aiding in plantarflexion for gait rehabilitation [45].

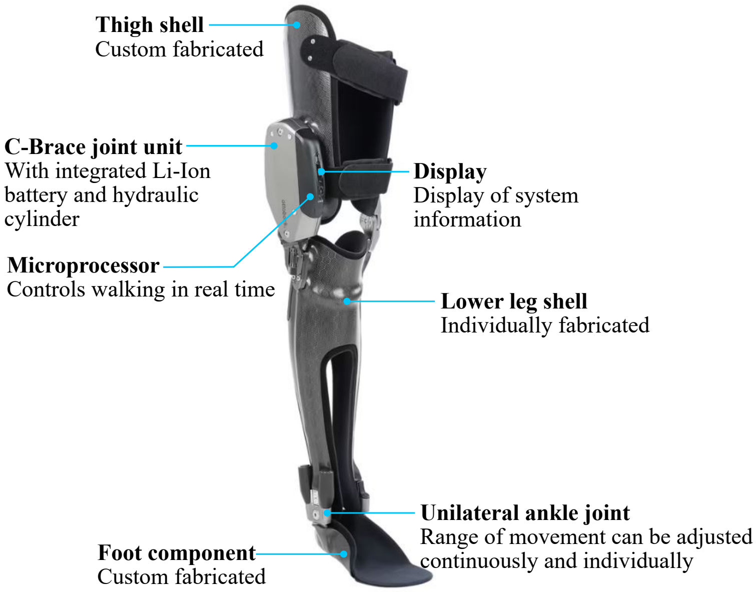

Figure 2.5: Ottobock C-Brace®. Figure adapted from [97].

ing spring pretension [100]–[106], adjusting the transmission mechanism between the load and the spring [107]–[110], and modifying the physical properties of the spring, such as its effective length or cross-sectional shape [111], [112]. Figure 2.8 showcases examples from literature employing various mechanisms for stiffness modulation in electromechanical variable stiffness actuators (VSAs). Utilizing nonlinear transmissions allows for tailored spring pretension adjustments to suit specific application needs. The cam mechanism,

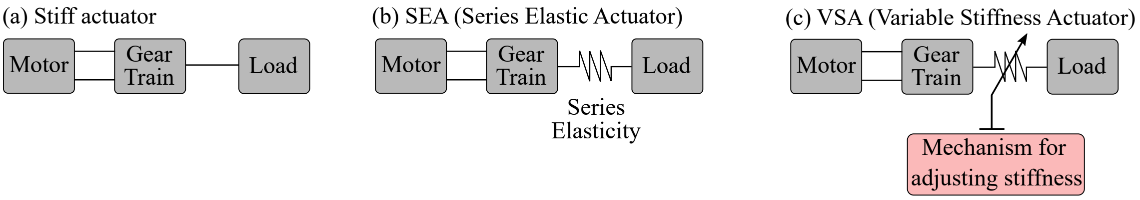

Figure 2.6: Actuator architectures: (a) Stiff actuator, (b) Series elastic actuator adds compliance, (c) Variable stiffness actuators adjust the stiffness of the spring through various mechanisms.

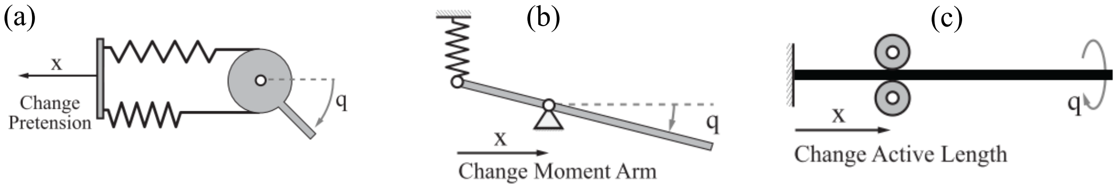

Figure 2.7: Various mechanisms for adjusting stiffness include (a) Spring pretension-based involving different spring configurations; (b) mechanisms employing variable moment arms with a movable pivot point; and (c) adjustments based on variable length. Figure adapted from [113].

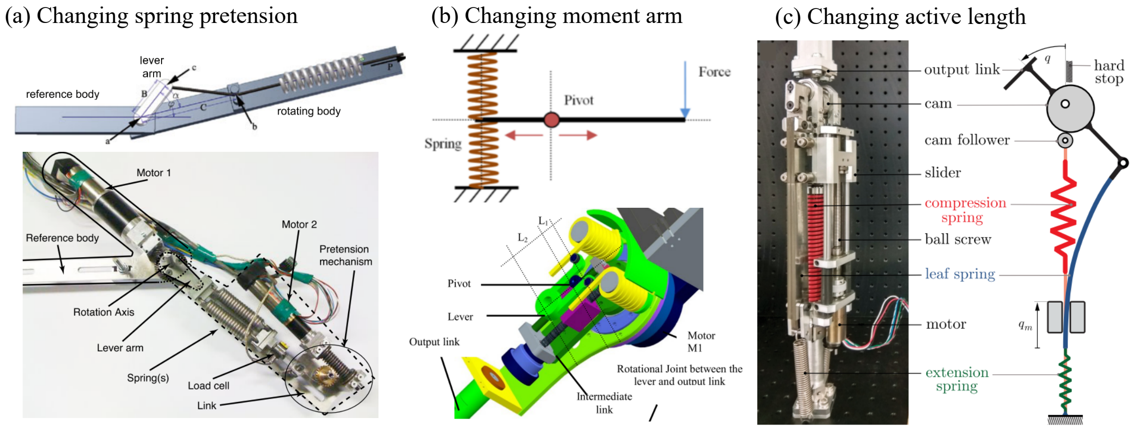
(a) Changing spring pretension (b) Changing moment arm (c) Changing active length

Figure 2.8: Electromechanical variable stiffness actuators using different mechanisms. (a) MACCEPA actuator utilizes a spring pretension-based mechanism adjusted by a lever arm, as depicted in the schematic. Motor 2 in the prototype adjusts spring pretension, while Motor 1 controls joint rotation [105], [114]. (b) AwAS-II alters stiffness by modifying the transmission between load and spring, achieved through pivot repositioning while maintaining fixed spring position [108]. (c) Braun et al. achieve wide-range stiffness modulation using a variable-length leaf spring [112].

commonly employed, provides desired stiffness-displacement characteristics. For instance, in MACCEPA and MACCEPA 2.0 [104], [105], a cam mechanism situated between two steering gears enables controlled adjustment of actuator stiffness. Unlike adjusting stiffness via spring preload, transmission modulation demands lower motor torque for stiffness adjustment. Lever mechanisms are often used, altering actuator stiffness by adjusting the lever's fulcrum or the spring's position along the lever arm [108], [115]. A third approach involves changing the active length, as demonstrated by Braun et al., achieving wide-range stiffness modulation of the VSA through a variable-length leaf spring [112].

2.1.2.4.2 Pneumatic Variable Stiffness: Exploiting the compressibility of air is another way to achieve stiffness modulation in exoskeletons. In pneumatic actuators, the stiffness is usually controlled by adjusting the pressure. Some examples of the studies on variable stiffness pneumatic actuators were conducted by [116], [117], where both groups controlled the stiffness by feeding the disparate amounts of compressed air to chambers from the remote air supply. Only recently, stiffness modulation demonstrated on an air cylinder in passive use without the remote air supply was proposed by [111]. Here, modulating the initial volume to be compressed affects the compression force, simultaneously increasing the stiffness range and storable energy capacity. This method is comparable to adjusting the active length of a spring in electromechanical variable stiffness actuators. However, cylinders have a limited stroke length, and shortening it could impact the usability as the available range of motion is impacted. Moreover, the future direction may involve integrating pneumatic variable stiffness actuators with other types, such as electric motors [118] or hydraulic systems [119].

An example of a pneumatic variable stiffness actuator is given in Fig 2.9. Here the stiffness adjustment is achieved through a pressure control mechanism, comprising two solenoid valves and an air cylinder actuated by a motor-screw system. Rotation of the stiffness modulation motor in either direction alters the pressure through the air cylinder.

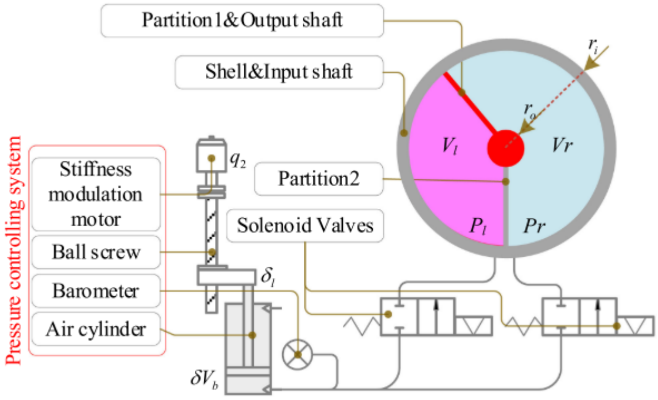

Figure 2.9: An example of a pneumatic variable stiffness actuator (schematic diagram). Figure adapted from [117].

2.1.3 Energy Harvesting Exoskeletons

Energy-harvesting exoskeletons are devices designed to harness and convert biomechanical energy generated during movement into electrical energy. Unlike usual actuators that consume energy, these devices employ actuators that use regenerative braking principles, similar to hybrid cars, to capture energy that would otherwise be dissipated. By selectively engaging energy harvesting during specific phases of movement, such as deceleration at negative joint power intervals, actuators assist in slowing down joints while simultaneously generating electricity [120]–[122]. Figure 2.10 illustrates an example of an exoskeleton equipped with a biomechanical energy harvester designed for electricity generation. Energy harvesting can also be done with pneumatic mechanisms, in such cases the biomechanical energy is converted to compressed air [55], [123].

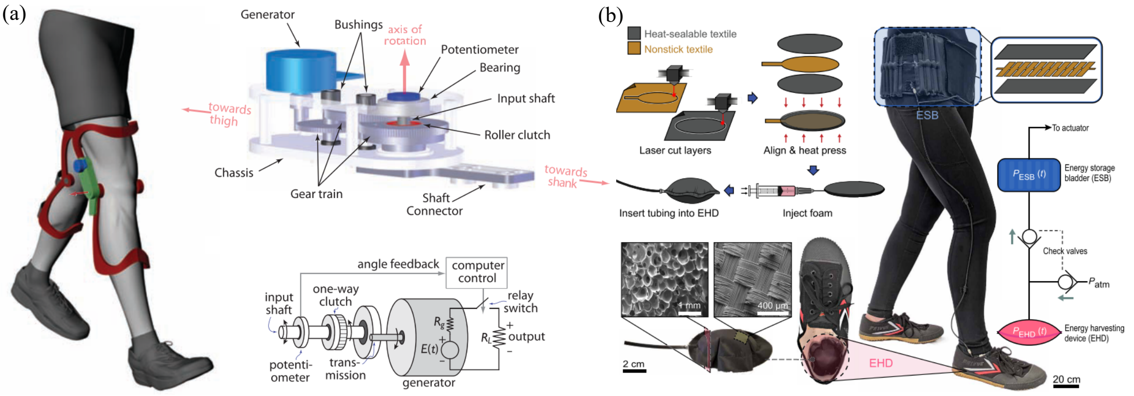

Figure 2.10: Exoskeletons for biomechanical energy harvesting: (a) Illustrates a device that converts biomechanical energy into electrical energy [122]. (b) Shows a device that generates compressed air from biomechanical energy [55].

2.1.4 Passive and Quasi-Passive Exoskeletons

Passive exoskeletons employ mechanical structures to enhance human movement without requiring external power sources. These systems utilize springs, dampers, and other passive elements to store and release energy, aiding in tasks such as lifting heavy loads or reducing muscle fatigue during repetitive motions (see Fig. 2.11). One significant advantage of passive solutions over active ones is their typically lower weight, as they lack bulky motors or batteries. However, they can not be controlled and have limited output power.

Passive exoskeletons may incorporate mechanisms like clutches to store energy during one phase of a task, later releasing it in another phase. This approach is frequently seen in the literature, particularly at the ankle joint [26], [27], and in combinations of ankle-knee systems [29]. Two examples of ankle exoskeletons with passive clutches are shown in Fig. 2.12. These passive clutches typically utilize mechanisms to engage or disengage the elastic element at specific joint angles. In the review paper on locking mechanisms in robotics by Plooij et al. [125], locking devices are divided into three main categories based on different locking principles: 1) mechanical locking, e.g. ratchet-pawl, 2) friction-based locking between two surfaces, and 3) singularity locking.

However, in the case of purely passive clutches, the moments of engagement and disengagement of the passive actuator cannot be controlled and can only be triggered exactly at a specific joint angle. In some cases, exoskeletons utilize electrical power to engage or disengage clutches or also power sensors, placing them in the category of quasi-passive

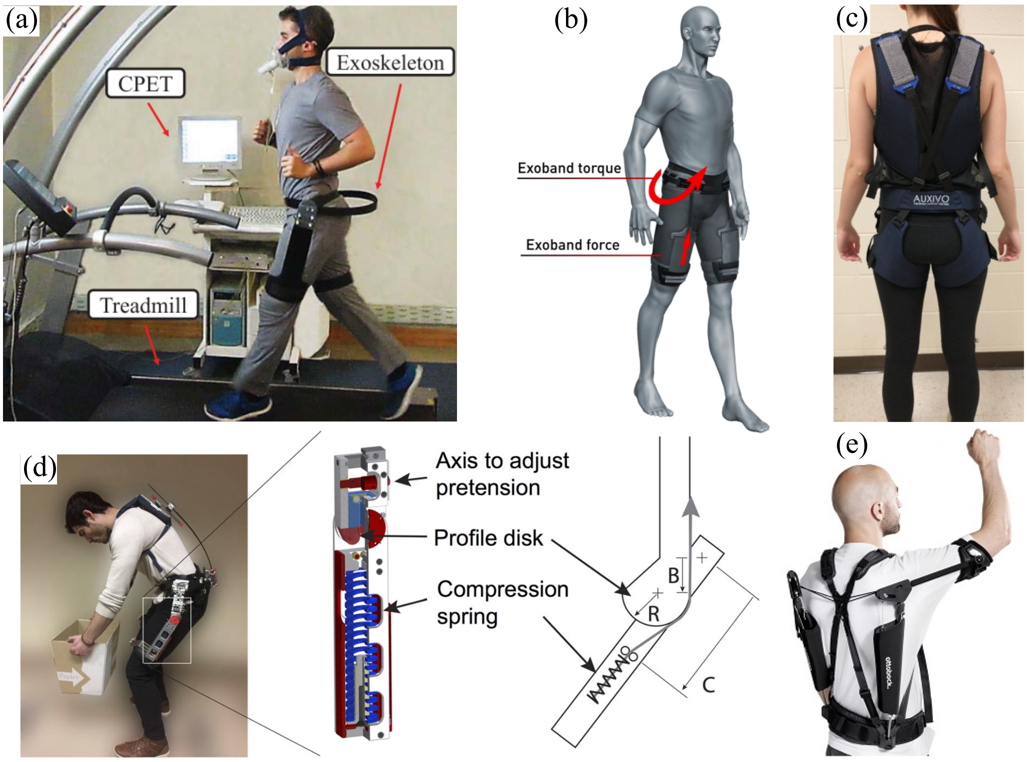

Figure 2.11: Examples of passive exoskeletons without clutches: (a) Hip exoskeleton aiding flexion and extension [30]. (b) Elastic band assisting hip flexion [31]. (c) LiftSuit by AUXIVO AG supports the lower back during lifting tasks or forward-leaning positions [32]. (d) SPEXOR Exoskeleton utilizing MACCEPA variable stiffness mechanics for lower back support [124]. (e) Ottobock Paexo shoulder exoskeleton for industrial workers [28].

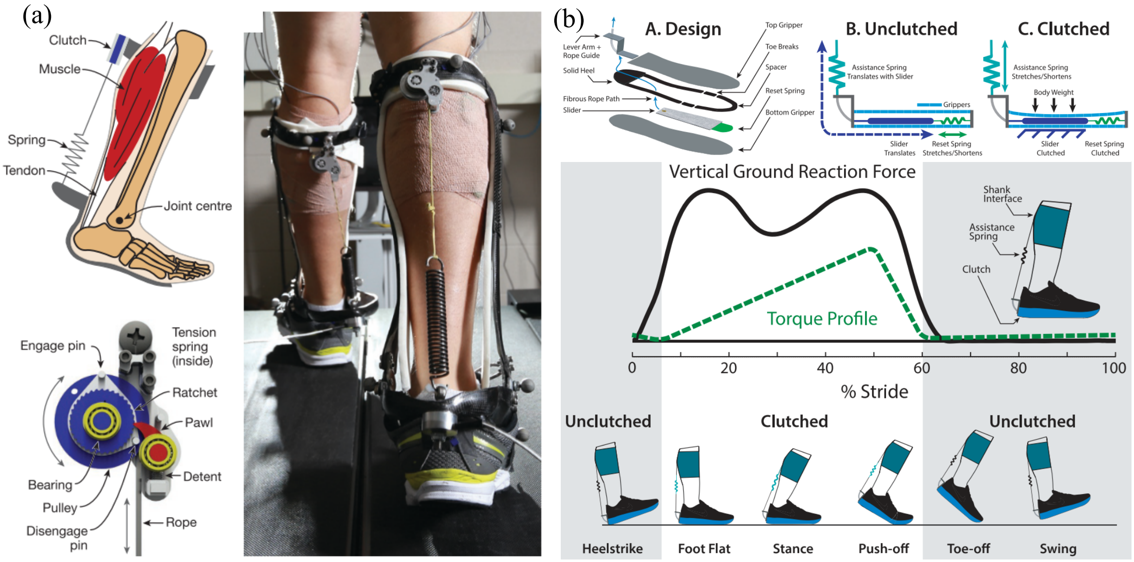

Figure 2.12: Examples of passive exoskeletons with clutches: (a) Ratchet-Pawl-based clutch activated via pin only at specific angles [26]. (b) Low-profile friction clutch mechanism [27].

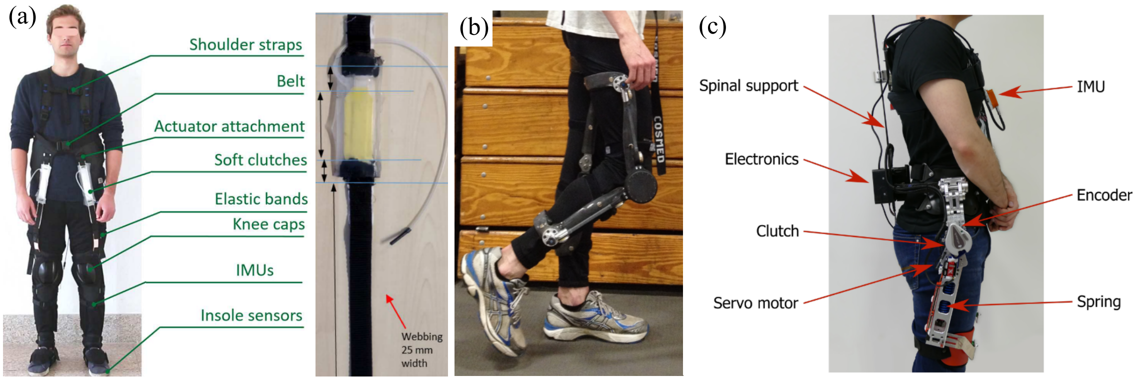

Figure 2.13: Quasi-Passive exoskeletons featuring passive actuators that are engaged or disengaged by actively controlled clutches. (a) Depicts a pneumatic-based friction clutch [34]. (b) Shows a custom interference clutch integrated with a planetary gear transmission [36]. (c) Includes a mechanical ratchet-pawl clutch actuated by a servo motor [35].

exoskeletons. Quasi-passive exoskeletons integrate minimal powered components to complement passive mechanisms or enable controlled activation and deactivation. While they primarily rely on passive technology to generate force or torque, akin to fully passive exoskeletons, they do not actively deliver positive net mechanical work to the user's joints. Instead, they store and release energy in synchronization with movement patterns to enhance performance. These quasi-passive designs strike a balance between energy efficiency and functionality, providing assistance to users while maintaining a lightweight and ergonomic structure. Examples of actively controlled clutches found in the literature include friction generated by air pressure between two surfaces [34], [126], electromagnetically engaged mechanical planetary gear clutches [36], servo motor-actuated mechanical ratchet-pawl systems [35], [127], and solutions such as electroadhesive clutches [128], [129]. Some examples of exoskeletons with actively controlled clutches are shown in Fig. 2.13.

2.1.5 Rigid Exoskeletons and Soft Exosuits

In the review so far, some devices are rigid or utilize rigid frames, while others are fabric-based and closely resemble clothing. This concept, known as exosuits, distinguishes itself from traditional exoskeletons by offering greater flexibility and comfort, akin to wearing a garment rather than a rigid mechanical device. In Figure 2.14a, the pioneering Hardiman exoskeleton, developed in 1967, exemplifies an early effort to amplify human strength for industrial applications using exoskeleton technology. Although it had massive strength, its adaptation to the human body was limited, and actually the robot was never tested with a human pilot. Nevertheless, the project sparked an ongoing interest in robots that could enhance or assist human motor performance, through a mechanical structure that mapped to the human anatomy [130]. With advancing technology, the transition toward more ergonomic designs was evident, as depicted in Fig. 2.14b with the HAL Cyberdyne exoskeleton. Rigid exoskeletons feature load-bearing structures made from materials like metal or carbon fiber, providing robust support and protection to the wearer, and are especially beneficial on joints where sustaining the weight is crucial. However, while offering high levels of mechanical support, rigid exoskeletons are often bulky and restrictive, limiting natural movement and agility. Over the years a new concept of exosuits has emerged that are intrinsically soft as they use textile-based parts to closely adhere to the body's contours. An example from Harvard suit [11] is shown in Fig. 2.14c. These exosuits are lightweight, comfortable, and offer a more natural range of motion compared to rigid exoskeletons. In a recent perspective on developments in wearable technology, J.L. Pons highlighted the trend towards less restrictive, more biomimetic designs for wearable robots [131]. This shift involves a preference for compliant materials that more effectively adapt to the complex anatomical features of the human body. Figure 2.15 showcases some of the latest exosuits developed in academia. The first one (a), developed by the Harvard Biodesign Lab, aids in hip flexion for patients with Parkinson's disease. The total weight of the exosuit is 2.31 kg, with only 0.22 kg distributed on each thigh. The second exosuit (b) aids in hip extension and has shown effectiveness in reducing sprint time. While the specific weight of the device is not provided in the paper, it is apparent that the exosuit places minimal mass around the limbs, focusing instead on placing it at the back. Lastly, in (c), a lightweight fabric-based inflatable exosuit, weighting 1.8 kg, provides assistance for both hip flexion and extension, although it is not portable.

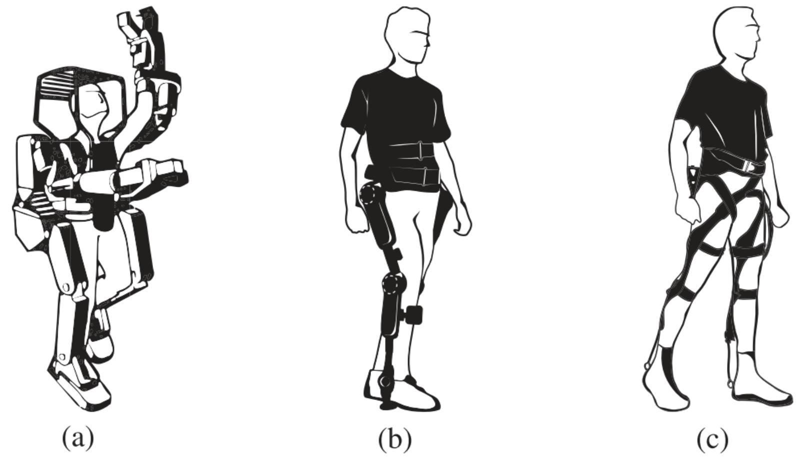

Figure 2.14: From Hardiman to more ergonomic rigid exoskeletons to exosuits. The figure is adapted from Xiloyannis et al. [57].

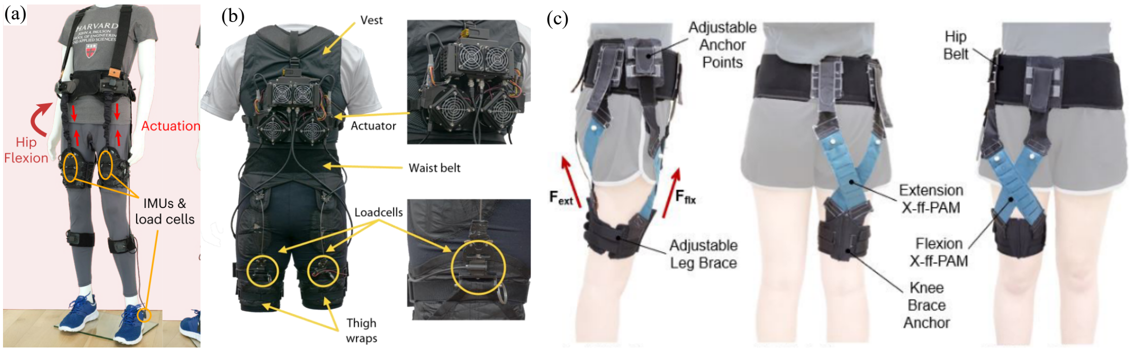

Figure 2.15: Latest advancements in exosuits. (a) Exosuit targeting hip flexion to treat freezing in Parkinson's disease patients [132]. (b) Exosuit aiding hip extension, resulting in reduced sprinting time [10]. (c) Pneumatic inflatable exosuit facilitating both hip flexion and extension [133].

2.1.6 Control of Lower-Limb Exoskeletons

Many lower-limb exoskeletons have been developed to assist gait, exhibiting a large range of control methods. The section is based on the review paper by Baud et al. [50]. The prevailing method involves a hierarchical structure comprising high, middle, and low levels. The high-level control governs the overall behavior of the exoskeleton. Typically, exoskeletons can transition between various operating modes, depending on the intended activity and environmental conditions, such as walking on level ground, ascending stairs, and performing sit-to-stand movements. At the high level, methods include manual user input such as buttons [81], [134] or voice commands [135], brain interfaces [61], [136], [137], automatic mode detection based on terrain [59], [60], [138], [139] or user movements detected from sensors and processed by a machine learning or fuzzy logic algorithm to recognize the situation [2], [140], [141]. The mid-level refers to the ongoing behavior of the robot, where it calculates the target torque or position for each joint at every step of the primary control loop. The mid-level controller significantly influences the interaction between the device and the user, and a considerable portion of exoskeleton control research focuses on this aspect. While the output of the high-level controller also impacts the behavior, it typically modifies certain parameters of the mid-level controller without fundamentally changing the essence of the interaction with the user. The low level operates close to the actuators, thus being dependent on the unique features of the actuator. Although many methods are adaptable across different robotic applications, their implementation in a gait assistance device does not deviate from the primary objective: accurately tracking a reference input or effectively controlling the valves in the case of pneumatic actuators, or engaging or disengaging clutches in quasi-passive systems. Examples encompass position/speed controllers with a proportional-integral-derivative (PID) regulator, and torque controllers [142]. The block diagram of the control strategies classification in lower-limb exoskeletons by Baud et al. [50] is given in Fig. 2.16.

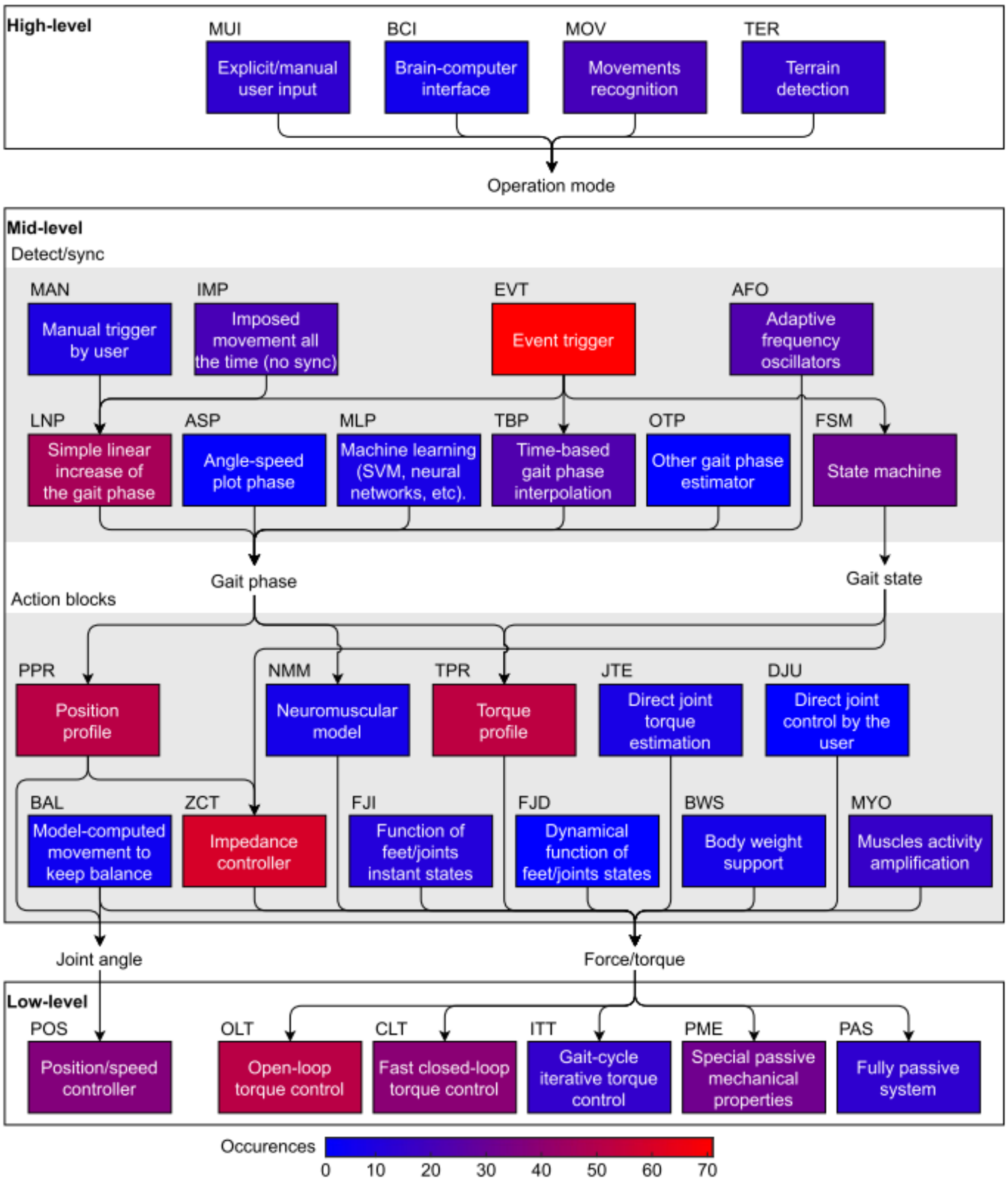

Figure 2.16: Control strategies classification diagram for lower-limb exoskeletons by Baud et al. [50]. Red indicates higher occurrences in literature, and blue is the opposite.

2.2 Proposed Methodologies

In the introduction, major ongoing challenges in the field were highlighted. However, this work does not attempt to address all of them; instead, it identifies specific challenges for targeted investigation. The focus areas of this work include:

- Variable stiffness mechanisms and how to make them simpler, lighter and better integrated in exoskeletons. In addition, how biomechanical energy can be utilized to change their stiffness.
- Investigating innovative approaches for delivering and recovering pneumatic energy.
- Exploring the potential synergies between soft exoskeleton designs and conventional designs to enhance the functionality of exoskeleton systems.

The methodology includes the design, control, and experimental evaluation of mechanisms, along with human studies with a newly developed exoskeleton. Figure 2.17 illustrates the key research milestones achieved in this dissertation, each supported by a corresponding peer-reviewed publication.

Figure 2.17: Key milestones in the dissertation. (a) Pneumatic quasi-passive variable stiffness mechanism for energy storage applications, published in [143]. (b) Pneumatic exoskeleton joint with a self-supporting air tank and stiffness modulation, published in [144]. (c) Active, quasi-passive, pneumatic and portable knee exoskeleton with bidirectional energy flow for efficient air recovery, published in [145]. (d) Hybrid rigid-soft and pneumatic-electromechanical exoskeleton for multi-joint lower limb assistance, published in [146].

The first milestone, depicted in Fig. 2.17a, is discussed in Chapter 3: "Quasi-Passive Pneumatic Variable Stiffness Mechanism" and is published in [143]. This chapter introduces a novel pneumatic quasi-passive mechanism designed for integration into exoskeletons. It consists of an air cylinder and three fast-switching valves, which are the only powered components. By strategically switching these valves on and off, the mechanism can be either fully deactivated, mimicking the functionality of a clutch, or activated to accumulate air within the cylinder. This unique feature enables stiffness modulation without the need for an external air supply. In essence, the mechanism functions as a quasi-passive spring, with its stiffness adjustable through the manipulation of the air valves.

The second milestone, depicted in Fig. 2.17b, is discussed in Chapter 4: "Pneumatic Exoskeleton Joint Mechanism" and is published in [144]. This chapter focuses on the mechanical design of the Pneumatic Exoskeleton Joint Mechanism (PEJM), which integrates the previously developed quasi-passive mechanism with a Pneumatic Artificial Muscle (PAM) acting as the air tank. The inclusion of the PAM not only influences stiffness but also allows the joint to generate compressed air internally, eliminating the need for an external air supply. Moreover, the PAM can store compressed air for subsequent use.

The third milestone, depicted in Fig. 2.17c, is elaborated in Chapter 5: "Knee Exoskeleton with Bidirectional Energy Flow" and published in [145]. This chapter introduces the complete mechatronic concept of the pneumatic portable bilateral knee exoskeleton, capable of operating in both active and quasi-passive modes. In the quasi-passive mode, the previously developed mechanism is utilized, while the active mode incorporates an integrated air pump for supplying compressed air. These multimodalities are expected to enhance energy efficiency while simultaneously efficiently assisting the user.

The fourth milestone, depicted in Fig. 2.17d and detailed in Chapter 5: "Hybrid

Rigid-Soft Exoskeleton for Multi-joint Lower Limb Assistance" is published in [146]. This milestone introduces a novel hybrid assistive device design, incorporating tendon-driven electromechanical actuation for the hip joint and a pneumatic rigid exoskeleton for the knee joint. The advantages of the novel design are discussed in detail in this chapter. Human studies are conducted to assess the impact on metabolic cost, kinematics, and muscular activity.

Chapter 3

Quasi-Passive Pneumatic Variable Stiffness Mechanism

Recent research has demonstrated the feasibility of augmenting humans while walking without delivering positive net mechanical work to the limbs which is achieved through passive lower limb exoskeletons that accumulate energy in elastic elements during negative joint power intervals and release it to support the limbs during positive joint power intervals [30], [31], [147], [148]. To improve the timing of energy accumulation during the gait cycle, clutches are often introduced in exoskeletons to store and reuse the energy, assisting the user with zero net mechanical work delivered [26], [27]. Even when some components, such as clutches or sensors, are powered, the exoskeleton relies fully on passive elastic components for assistance. This concept is known as quasi-passive exoskeletons [34], [36], [127]. This approach has proven to be a practical solution for reducing weight, significantly enhancing the system's energy efficiency and autonomy.

However, all quasi-passive exoskeletons appearing in the literature feature elastic elements with a fixed stiffness, typically a spring, selected heuristically by physically replacing the spring with another one and measuring the best outcome. The maximum energy that can be stored in these fixed stiffness elastic elements changes with the deflection. A low-stiffness element can store only a small amount of energy, while a high-stiffness element has a greater energy storage capacity but requires a higher force to deflect it meaning it could impede the motion during the energy-storing phase. In quasi-passive exoskeletons, this means a cumbersome and time-consuming heuristic process to approach the optimum stiffness. Moreover, even when the optimum stiffness is achieved, changes in task conditions, such as walking speed, necessitate adjusting the stiffness of the spring again. Consequently, quasi-passive exoskeletons that exist are optimized only for specific conditions. Furthermore, transitioning between tasks, such as walking and jumping, would require physically replacing the elastic element with one suited to the specific task. Therefore, the ability to actively vary stiffness in quasi-passive exoskeletons and their elastic elements is crucial for enhancing performance in highly dynamic human activities, such as running or jumping [149]. Recent efforts by [33] have focused on developing an actively controlled stiffness of the spring for a quasi-passive ankle exoskeleton. Their mechanism adjusts the attachment point of a single stiffness spring using an electric motor and slider mechanism, thereby altering the lever arm and torsional stiffness. While innovative, this approach introduces additional mechanical complexity and increases the mass on the distal limbs, which is not ideal for exoskeleton design [11]. Stiffness modulation in robotic electromechanical actuators is generally accomplished through various methods, as detailed in the literature review of this dissertation and outlined in the review article by Wolf et al. [99]. Although some actuators have found success in robotics applications, their integration into exoskeletons is often hindered by ergonomic challenges stemming from their dimensions or mechanical complexity. Stiffness adjustment mechanisms remain complex, and the resulting devices tend to be bulky.

Exploiting the compressibility of air is another effective method for achieving stiffness modulation in exoskeleton robots. Soft, pressurizable actuators offer significant advantages due to their high strength-to-weight ratio [45], [150]–[152]. In these actuators, stiffness is typically controlled by adjusting the air pressure [5], [94], [153]. Studies on variable stiffness pneumatic actuators, such as those by [116], [117], have demonstrated controlling stiffness by varying the amount of compressed air supplied to the chambers of either a linear pneumatic cylinder or a rotary pneumatic actuator from a remote air source. However, the aforementioned pneumatic actuation systems rely on a remote air pressure supply to modulate stiffness, which is not well-suited for exoskeletons. Recently, [111] demonstrated a method to modulate stiffness in an air cylinder for quasi-passive use without a remote air supply. By adjusting the initial volume to be compressed, this method affects the compression force, thereby increasing both the stiffness range and the storable energy capacity. Adjusting the initial volume involves changing the position of the piston's rod using an external device. Despite these advancements, air cylinders have a limited stroke length, and changing the initial position affects the range of motion. In the discussion, the authors suggest another method to increase the amount of air in the chambers is to use an air pump. In this chapter, we propose an innovative solution to modulate the amount of air inside the air cylinder's chamber to adjust the stiffness. This method requires no additional air pump, instead, it utilizes a vacuum of the pneumatic cylinder to accumulate air. We propose a pneumatic quasi-passive mechanism for application in quasi-passive exoskeletons, consisting of an air cylinder and three fast-switching valves. The two main **contributions** can be summarized as:

1. A novel quasi-passive pneumatic mechanism, which can be entirely deactivated, i.e. mimics a mechanical clutch's functionality and requires a minimum power input for operation. Moreover, it is lightweight, offers a compact integration, and has a high mass-energy storage capacity.
2. A novel method of stiffness modulation, by accumulating air in the chamber using the passive dynamics of the air cylinder. This is achieved without a separate supply of compressed air. Additionally, a mathematical description of the method is given, which is validated through experiments.

The chapter is organized as follows. Section 3.1 mathematically describes the mechanism and the new methodology for stiffness modulation. Section 3.2 presents the experimental setup and two procedures for validating the theoretical concept: by modifying the initial position and by modifying the initial pressure. Our results are discussed in Section 3.3. Next, a comparison and an example of practical applicability are given in Section 3.4. Finally, Section 3.5 concludes the chapter.

The work of this chapter was published in IEEE Robotics and Automation Letters [143], and presented at the IEEE International Conference on Robotics and Automation in Philadelphia in 2022.

3.1 Mathematical Model

The pneumatic quasi-passive mechanism consists of a pneumatic cylinder and three air solenoid valves connected in the configuration as shown in Fig. 3.1 and it represents the initial phase in the exoskeleton's development (see Fig. 2.17a). This mechanism is quasi-passive, meaning that electrical power is only needed to control the valves, which in turn changes the behavior of the elastic element, in this case, the pneumatic cylinder. The cylinder accumulates atmospheric air when the valves are switched in a timed sequence and the piston rod is deflected from its initial equilibrium position, typically by human limbs, as seen in quasi-passive exoskeletons. Accumulating additional air in the pneumatic cylinder increases the pressure, thereby increasing the stiffness. Thanks to the configuration of the valves, the mechanism can operate in various modes, as shown in the table of possible states in Fig. 3.1. In the nonlinear spring mode, the force of the air cylinder is proportional to the stiffness k_n, which can be adjusted by either changing the initial position z_0, thereby increasing the volume, or by adding an additional amount of air inside the chambers. The latter is achieved through timed valve control in M steps, where n indicates the current step. Adding more air into the same volume increases the air cylinder's initial (equilibrium) pressure at position z_0. The following text will mathematically describe this process.

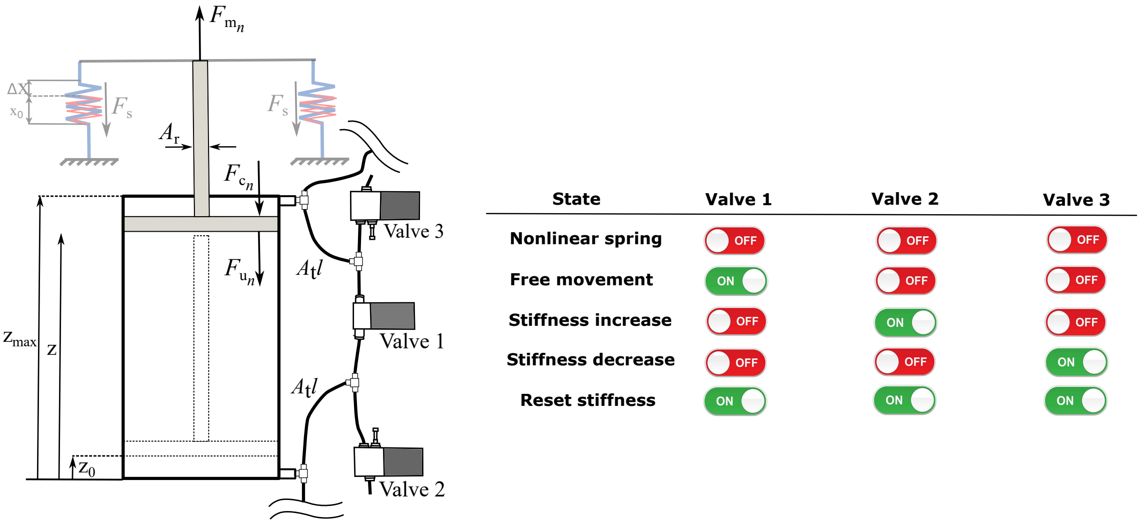

State	Valve 1	Valve 2	Valve 3
Nonlinear spring	OFF	OFF	OFF
Free movement	ON	OFF	OFF
Stiffness increase	OFF	ON	OFF
Stiffness decrease	OFF	OFF	ON
Reset stiffness	ON	ON	ON

Figure 3.1: Possible states of the quasi-passive mechanism, where ON denotes that the valve is open and vice versa, OFF indicates that the valve is closed.

3.1.1 Modeling the Stiffness of the Quasi-Passive Mechanism

The total force required to deflect the air cylinder from the initial position z_0 to position z is formulated according to Fig. 3.1:

$$F_{\mathrm{m}n}(k_{\mathrm{n}}, z) = F_{\mathrm{c}n} + F_{\mathrm{u}n}, \quad z \in [z_0, z_{max}], n \in [0, M] \tag{3.1}$$

where $F_{\mathrm{c}n}$ denotes the force produced by the compressed air pressure $p_{\mathrm{c}n}$ acting on the surface area A_{c}, and $F_{\mathrm{u}n}$ the pulling force produced when below atmospheric air pressure $p_{\mathrm{u}n}$ acts on the surface A_{u} in the low vacuum chamber

$$F_{\mathrm{c}n} = p_{\mathrm{c}n} A_{\mathrm{c}}, \tag{3.2}$$

$$F_{\mathrm{v}n} = p_{\mathrm{u}n} A_{\mathrm{u}}. \tag{3.3}$$

Assuming that the air cylinder deflects from the initial position z_0 at an adequately low frequency, the process can be observed as isothermal compression where the forces before increasing the stiffness are shown in Fig. 3.2. Considering the isothermal assumption, the

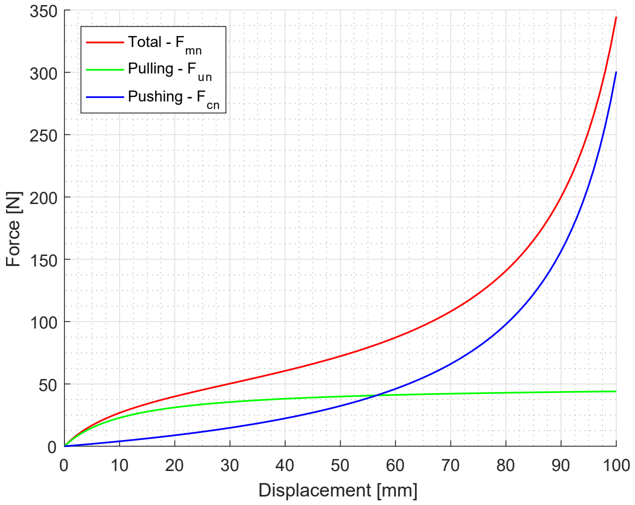

Figure 3.2: Theoretical forces in both chambers and total force when functioning as a nonlinear spring. $F_{\mathrm{m}n}$ is the total force to pull the rod from its initial position, $F_{\mathrm{u}n}$ is the pulling force due to vacuum, $F_{\mathrm{c}n}$ is the pushing force due to compressed air. Forces shown are before the stiffness increase ($p_{\mathrm{i}0} = p_{\mathrm{atm}}$).

pressure in the chamber containing compressed air or another ideal gas is given by

$$p_{\mathrm{c}n} = p_{\mathrm{i}n} \frac{A_{\mathrm{c}}(z_{\mathrm{max}} - z_0) + A_{\mathrm{t}} l}{A_{\mathrm{c}}(z_{\mathrm{max}} - z) + A_{\mathrm{t}} l}, \tag{3.4}$$

where $p_{\mathrm{i}n}$ is the initial pressure at the equilibrium position z_0 in the n^{th} step of iterative stiffness increase through air accumulation. We assume that in the beginning $p_{\mathrm{i}0} = p_{\mathrm{atm}}$, where the p_{atm} is the atmospheric pressure. Note that the plastic tubes as illustrated in Fig. 3.1 add extra volume to the two chambers, expressed by the product of the tube's cross-sectional area and its length ($A_{\mathrm{t}} l$).

Similarly, the below atmospheric air pressure in a low vacuum chamber can be expressed as follows

$$p_{\mathrm{u}n} = p_{\mathrm{i}n} \frac{A_{\mathrm{u}} z_0 + A_{\mathrm{t}} l}{A_{\mathrm{u}} z + A_{\mathrm{t}} l}. \tag{3.5}$$

Stiffness modulation through steps is illustrated in Fig. 3.3. Assuming that at the initial step $n = 0$, there is no previously added additional amount of air from the atmosphere, i.e., $\Delta N_0 = 0$ gives

$$N_{\mathrm{tot}0} = \cancel{\Delta N_0} + N_{\mathrm{u}0} + N_{\mathrm{c}0}. \tag{3.6}$$

Increasing the amount of air $N_{\mathrm{tot}n}$ inside the air cylinder is a two-step process in which we must first open valve 2 during below atmospheric pressure in the blue-colored chamber, as shown in Fig. 3.3b, and then close valve 2 and open valve 1, as shown in Fig. 3.3c. By repeating these two steps, we can increase the total pressure in the air cylinder. The total amount of air is now given by

$$N_{\mathrm{tot}n} = \Delta N_{n-1} + N_{\mathrm{u}n-1} + N_{\mathrm{c}n-1}, \tag{3.7}$$

where $N_{\mathrm{u}n-1}$ is the amount of air in the low vacuum chamber in the previous step, $N_{\mathrm{c}n-1}$ the amount of compressed air in the previous step, and ΔN_{n-1} the added amount of air in the previous step. Here $N_{\mathrm{u}n}$, $N_{\mathrm{c}n}$ and ΔN_n are given by

$$N_{\mathrm{u}n} = \frac{p_{in} A_{\mathrm{u}} z_0}{R_{\mathrm{m}} T}, \tag{3.8}$$

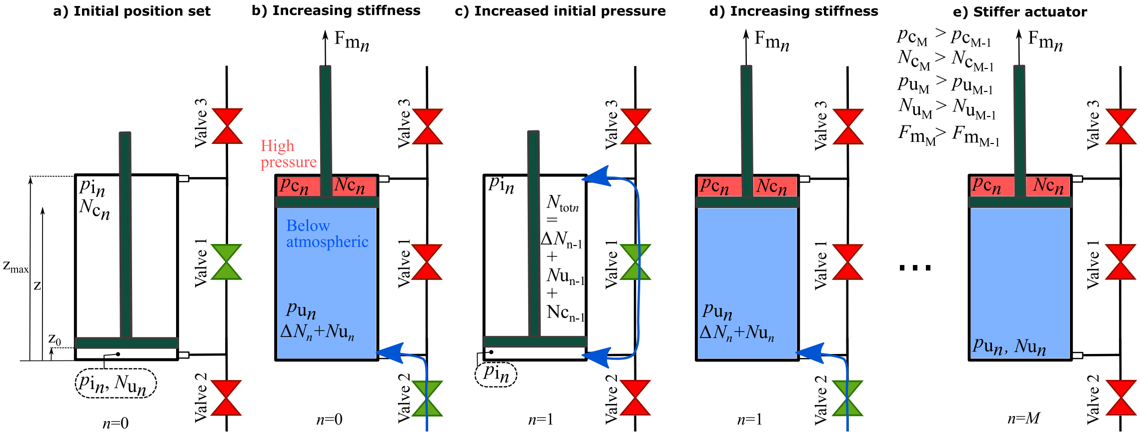

Figure 3.3: Stiffness modulation method in a pneumatic quasi-passive mechanism. Modes are switched in a timed sequence while the piston rod is deflected by an external force to adjust the pressure inside the cylinder. Below atmospheric air pressure is used to draw additional air into the cylinder.

$$N_{cn} = \frac{p_{in} A_c (z_{max} - z_0)}{R_m T}, \tag{3.9}$$

$$\Delta N_n = \frac{p_{un} A_u z}{R_m T}, \tag{3.10}$$

where R_m is the universal gas constant and T is the Kelvin temperature. Note that increasing the amount of air in the same volume leads to an increase in the initial pressure p_{in}. We refer to the initial pressure as the pressure in the air chambers when no external force is acting on the cylinder. The initial pressure p_{in} is given by

$$p_{in} = \frac{N_{totn} R_m T_m}{A_u z_{max} + A_t l}. \tag{3.11}$$

The value of p_{in} is limited, when the p_{un} approaches p_{atm}, the amount of air cannot be increased any further. The increase in pressure p_{in} is shown in Fig. 3.4.

Finally, the force of an air cylinder that can be modulated by changing z_0 or p_{in} is given by

$$F_{mn}(z, z_0, p_{in}) = p_{in} \left(\frac{A_c(z_{max} - z_0) + A_t l}{A_c(z_{max} - z) + A_t l} A_c + \frac{A_u z_0 + A_t l}{A_u z + A_t l} A_u \right). \tag{3.12}$$

Once the force is determined, the stiffness can be readily calculated as

$$k_n = \frac{\partial F_{mn}(z, z_0, p_{in})}{\partial z}, \tag{3.13}$$

and the storable elastic energy of an air cylinder as

$$H_n = \int_{z0}^{z} F_{mn}(z, z_0, p_{in}) dz. \tag{3.14}$$

When modulating the stiffness by increasing p_{in}, both the energy storage and the maximal achievable stiffness increase (Fig. 3.5), while the range of motion remains the same.

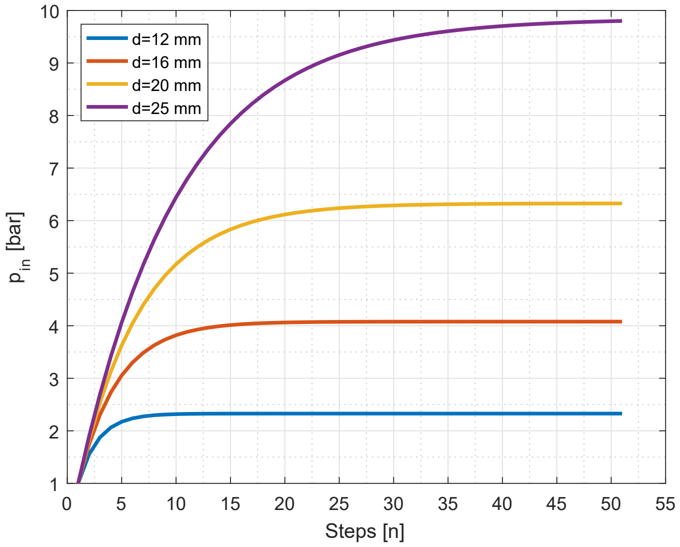

Figure 3.4: Modulation of the initial pressure for different sizes of cylinder diameter and $z = z_{\max} = 100$ mm.

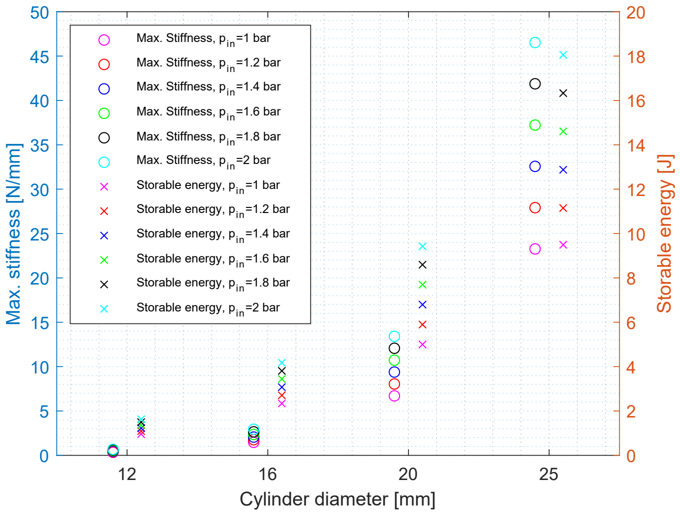

Figure 3.5: Theoretical increase in maximum stiffness and energy storage capacity for different initial pressure and cylinder sizes. Results shown are for the cylinder with a total stroke length of 100 mm.

3.2 Experimental Evaluation

To validate the mathematical models, we employed an experimental setup, as schematically illustrated in Fig. 3.6. The setup comprises three main components: the quasi-passive mechanism, the load, and the control system.

3.2.1 Description of Components

Quasi-passive mechanism: The blue area represents the quasi-passive mechanism. The air cylinder used, DSNU-25-100-PPV-A, has a total stroke length of 100 mm and a bore diameter of 25 mm. Fast switching valve 1, MHJ10-S-2,5-QS-4-LF, operates as a 2/2 normally closed monostable valve, with a switching frequency of 500 Hz. Fast switch-

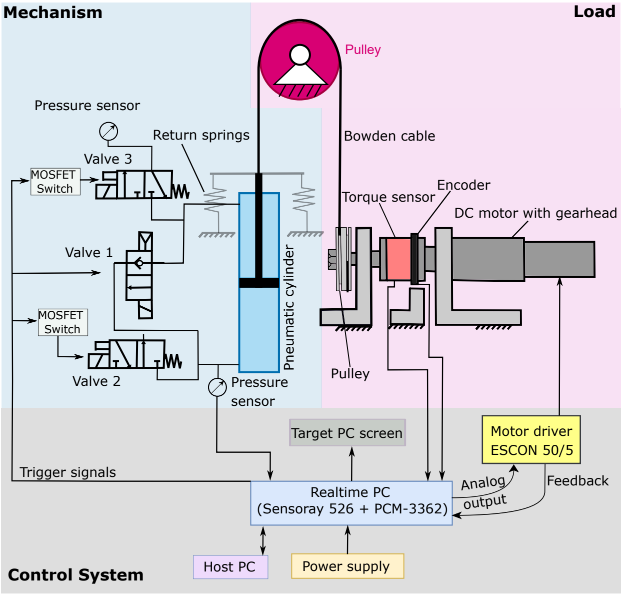

Figure 3.6: Schematic of the experimental setup composed of: Quasi-passive mechanism, Load and Control System.

ing valve 2, MHE2-MS1H-3/2G-QS-4-K, functions as a 3/2 open monostable valve, and valve 3, MHE2-MS1H-3/2O-QS-4-K, operates as a 3/2 closed monostable valve; both have a switching frequency of 330 Hz. Pressure sensors monitor the air pressure changes in both cylinder chambers. Mechanical return springs are added to simplify the automatic experimental procedures by ensuring the cylinder returns fully to the starting position after being pulled. These springs are not considered part of the quasi-passive mechanism. Their stiffness constant is 0.18 N/mm, resulting in a force considerably lower than that of the air cylinder. Nevertheless, their effect was subtracted from the air cylinder's force during post-analysis.

Load: The pink area represents the load that simulates movements from a human joint. This load setup includes a Maxon 80 W DC motor with a 113:1 reduction ratio gearbox. The output shaft is directly connected to an RT-500 torque sensor, which has a rated torque of 55 Nm. For precise angle measurements, an incremental off-axis RLS-RM22 RoLin encoder with a reading head mounted on an angle bracket is included. All non-standard components are either rapid-manufactured or machined. Torque is transmitted via a pulley, around which a flexible Bowden cable is wound.

Control System: The control system comprises the real-time PCM-3362 PC-104 with a Sensoray 526. It is fully compatible with Simulink Real-Time$^{\text{TM}}$, enabling real-time control at 1000 Hz. Data is initially collected on the Host PC and subsequently analyzed.

3.2.2 Experimental Procedure

The experiments aim to validate the theoretically proposed stiffness modulation by altering the initial position z_0 and the initial pressure p_{in}. The experimental setup, depicted in Fig. 3.7, involves pulling the pneumatic cylinder's rod from its initial equilibrium position using force applied to the Bowden cable, generated by the motor to simulate human limb movement. For the experiment, the load, represented by the motor, was position-controlled concurrently with the control of all three valves. With a known pulley diameter (55.5 mm), the torque measured by the torque sensor was converted to the corresponding force.

Likewise, the angular displacement of the encoder was converted to the corresponding linear displacement.

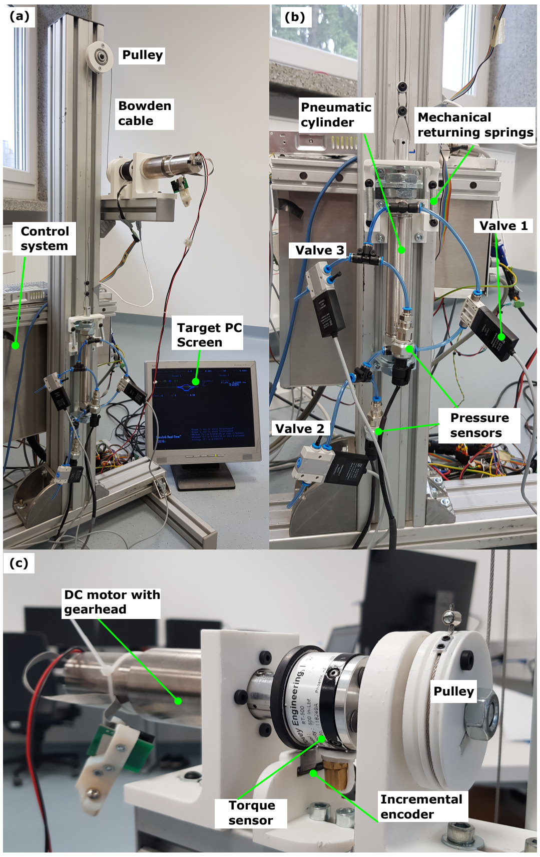

Figure 3.7: Experimental setup. a) Overview, b) Quasi-passive mechanism c) Load

Two distinct series of experiments were conducted. Firstly, to examine how altering the initial position z_0 impacts the total force, stiffness, and energy capacity. Secondly, to demonstrate how varying the initial pressure $p_{\mathrm{i}n}$ influences these parameters.

Modifying the initial pressure: To increase the initial pressure with the air accumulating method $p_{\mathrm{i}n}$, it is necessary to perform several cycles. In each cycle, the piston rod was first pulled with the valves closed (Fig. 3.3-e) to measure the force characteristic with respect to angular displacement. This was followed by a two-step procedure of increasing the initial pressure as shown in Fig. 3.3-a and -b. This procedure was repeated 6 times. In the first step, the pressure was $p_{\mathrm{i}1} = 1$ bar. Ideally, the pressure pi_n is increased by 0.2 bar in each step, so that in the 6th step, the pressure is $pi_6 = 2$ bar. Using equations (4.26), (4.24), (4.25), (4.23), and (3.11), we estimated the z required to increase the pressure by the desired amount in each step. Between each $p_{\mathrm{i}n}$ increase, the piston was pulled from the initial position z_0 to the final position z_{max}. The process is repeated at the same rate in both experiments. A supplementary video with experiments is available for download.

Modifying the initial position: In this experiment, the piston was positioned at five different initial positions: $z_0 = 0$ mm, $z_0 = 20$ mm, $z_0 = 40$ mm, $z_0 = 60$ mm, and $z_0 = 80$ mm, and pulled to the final position z_{max}. The initial position was first set with valve 1 open, and then pulled to the final position with all valves closed. Increasing the initial position z_0 reduces the volume of air to be compressed $N_{\mathrm{c}n}$, and increases the volume of air in the low-pressure chamber $N_{\mathrm{u}n}$. Once the piston was adjusted to the position, all three valves were closed and the pulling of the piston rod was executed. This experiment was conducted with $p_{\mathrm{i}n} = p_{\mathrm{atm}}$ in all five cases.

3.3 Results

Figure 3.8 presents both the theoretical results (a) and measured findings (b), illustrating the modulation of force by the internal pressure $p_{\mathrm{i}n}$, for six different theoretical pressure levels: $p_{\mathrm{i}1} = 1$, $p_{\mathrm{i}2} = 1.2$, $p_{\mathrm{i}3} = 1.4$, $p_{\mathrm{i}4} = 1.6$, $p_{\mathrm{i}5} = 1.8$, $p_{\mathrm{i}6} = 2$ bar, with an ideal increment of 0.2 bar. However, the measured pressure levels were $p_{\mathrm{i}1} = 1$, $p_{\mathrm{i}2} = 1.1$, $p_{\mathrm{i}3} = 1.32$, $p_{\mathrm{i}4} = 1.5$, $p_{\mathrm{i}5} = 1.73$, $p_{\mathrm{i}6} = 1.92$ bar. As anticipated, there were some inaccuracies observed in the initial steps of pressure increment. These inaccuracies may stem from minor air leakage and imprecise air volumes within the plastic tubes and connections. Consequently, determining the precise piston position necessary to achieve the intended pressure increase of 0.2 bar becomes challenging. Nonetheless, the model approximates the expected step increase adequately for quasi-passive exoskeleton applications. Furthermore, our experimental results in (b) indicate a direct correlation that higher initial equilibrium pressure $p_{\mathrm{i}n}$ corresponds to increased force, stiffness (indicated by the slope of the curve), and energy capacity (reflected by the area under the curve), aligning with the predictions of our mathematical model. The accuracy of the mathematical model is also affected by minor variations in the length of the plastic tube, which change the volume and, consequently, impact both pressure and force. Additionally, it's important to acknowledge the possibility that the process may not be entirely isothermal, as assumed in the mathematical model. Theoretical forces obtained by the model were $F_{\mathrm{i}1} = 352$, $F_{\mathrm{i}2} = 420$, $F_{\mathrm{i}3} = 487$, $F_{\mathrm{i}4} = 555$, $F_{\mathrm{i}5} = 622$, and $F_{\mathrm{i}6} = 689$ N, while measured forces are $F_{\mathrm{i}1} = 305$, $F_{\mathrm{i}2} = 392$, $F_{\mathrm{i}3} = 467$, $F_{\mathrm{i}4} = 531$, $F_{\mathrm{i}5} = 607$, and $F_{\mathrm{i}6} = 670$ N. Nevertheless, the measured results exhibit good consistency with the theoretical framework.

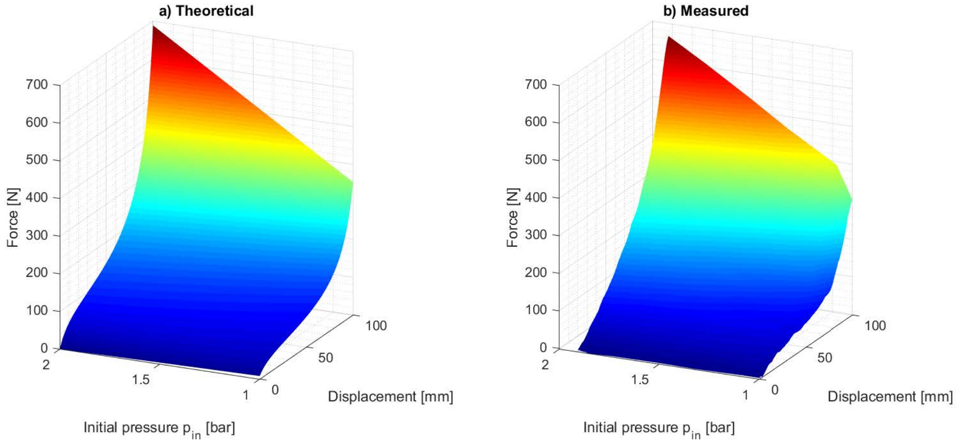

Figure 3.8: Experimental results depicting the force of the quasi-passive mechanism in relation to linear displacement for various stepwise increments of initial pressures $p_{\mathrm{i}n}$. Theoretical results are presented in (a), while (b) displays the measured results.

The results depicting the modulation of initial positions z_0 are presented in Fig. 3.9, where the measured outcomes are compared with our mathematical model represented by the dashed line. Notably, as the initial position z_0 decreases, both the total force and stiffness exhibit an increase. Furthermore, there is a corresponding increase in the stored elastic potential energy, evident from the expanded area under the curves. When z_0 is smaller, it signifies a greater volume of air N_{cn} within the compression chamber, leading to higher pressure p_{cn} and, consequently, a higher pushing force in the compression chamber. Also, smaller z_0 results in a larger negative pressure p_{un} when the piston is pulled, and thus a larger pulling force. These findings suggest that valve 1 can function as a clutch, adjusting the effective length of the pneumatic cylinder when used as a passive air spring.

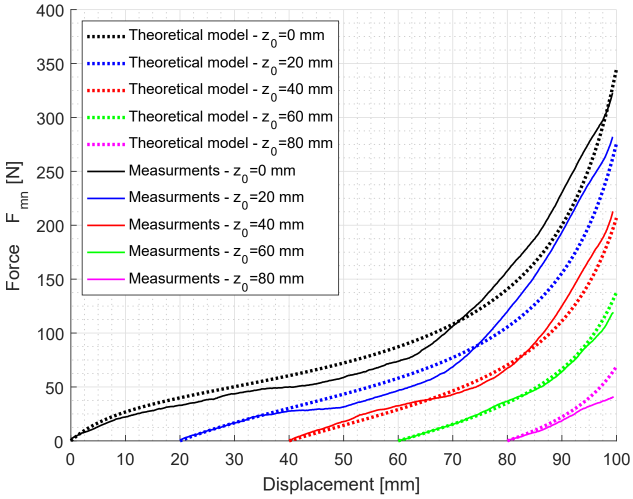

Figure 3.9: Experimental force measurements in the air cylinder versus linear displacement at five initial positions z_0, with constant initial pressure $p_{in} = 1$ bar and a cylinder stroke of 100 mm. The dashed curve depicts theoretical results.

3.4 Application, Comparison, and Discussion

The measurements demonstrate that the proposed pneumatic mechanism can adjust both the force required to deflect the pneumatic cylinder and the force gradient, commonly known as stiffness. This modulation can be achieved in two demonstrated ways. This section discusses the results in terms of their practical applicability and advantages for exoskeletons. To illustrate these benefits, we compare the technical specifications of the proposed mechanism with those of the recent quasi-passive ankle exoskeletons' mechanism. To contextualize the mechanism within the framework of exoskeleton design, we propose a comparison with recent ankle exoskeletons, as shown in Table 3.2, where the elastic element is positioned parallel to the calf muscle. Hence, the application of the quasi-passive ankle mechanism with our proposed device is depicted in Fig. 3.10.

Technical specifications are summarized in Table 6.1. The overall mass of the mechanism is 443 g, with valve 2 and valve 3 each weighing 60 g, and valve 1 (clutch) weighing 85 g. The selected air cylinder weighs 238 g. At this stage of development, the mass of electronics that would be required to power the valves is not directly comparable since the experiments were conducted in an experimental setup. However, powering the valves would necessitate a battery, with each valve consuming 0.09-0.44 mA of current for the trigger signal. As previously described, valve 1 activates the clutch feature, while the two remaining valves allow for stiffness modulation independently of the exoskeleton's lever arm length. This feature presents the opportunity for a slim design without protrusions at the ankle, which is a common occurrence in ankle exoskeletons to enhance mechanical advantage. Specifically for the selected cylinder, if $p_{in} = 9.8$ bar (theoretical maximum, see Fig. 3.4), the stiffness would theoretically be 228 N/mm. However, this level of stiffness

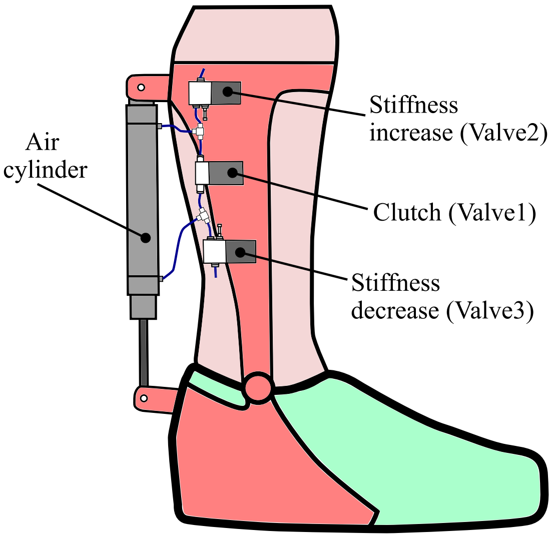

Figure 3.10: Proposed application of a pneumatic quasi-passive variable stiffness mechanism for a portable ankle exoskeleton.

may not be practically achievable due to mechanical constraints. Nonetheless, a maximum force of 670 N was measured at an initial pressure of 1.92 bar. When computing stiffness as the gradient of force using Eq. (3.13), a maximum stiffness of 20.8 N/mm was attained through the experiments. Similar reasoning applies to the maximum energy storage capacity, which theoretically peaks at 85 J with $p_{in} = 9.8$ bar. However, in our experiments, the maximum energy of 22 J was stored. This was calculated using Eq. (3.14) applied on the measured force-deflection curve. While this value could potentially be further increased in experiments, the used experimental setup did not allow such high forces.

Table 3.1: Technical specifications Pneumatic Quasi-Passive Variable Stiffness Mechanism

Total mass[1]	443 g
Air cylinder's dimensions	∅25x100
Air cylinder's mass	238 g
Valve 1 mass	85 g
Valve 2 and 3 mass	60 g each
Valve operating voltage	24 V
Mass at waist or back	N/A
Quasi-passive	Yes
Variable stiffness	Yes
Lever arm length	Independent of stiffness
Stiffness range	0-20.8 N/mm, (0-228 N/mm Theoretical)
Energy capacity	22 J, (85 J Theoretical)

[1] The mass of the whole mechanism without the exoskeleton frame.

3.4.1 Comparison with Existing Solutions

Table 3.2 reveals that both Collins et al. and Yandell et al. have lower overall weights, while Kumar et al. have introduced a stiffness modulation mechanism where the spring

Table 3.2: Technical specifications of recent Quasi-Passive Ankle Exoskeletons

	Collins et al. 2015 [26]	Yandell et al. 2019 [27]	Kumar et al. 2020 [33]
Mass per leg	408 - 503 g	459 g	1323 g
Clutch's mass	57 g	186 g	N/A
Mass of electronics	0 g	0 g	1750 g
Quasi-passive	Yes	Yes	Yes
Variable stiffness	No	No	Yes (Torsional)
Lever arm length	0.152 m	0.1 m	0.17-0.25 m
Spring stiffness	7.9 N/mm[1]	6.1 N/mm[1]	5.8 N/mm
Energy capacity[2]	N/A	N/A	N/A

[1] Heuristically found optimal stiffness.

[2] Unknown total spring travel.

attachment slides on a ball screw driven by a stepper motor. While this solution is pragmatic, it increases the weight and dimensions of the system, particularly the lever arm length, which in our case is independent of stiffness. Comparing the specifications of our newly proposed mechanism with those of other studies, it becomes apparent that the mass of our mechanism would be reasonable in actual implementation. One drawback is the need for a battery to operate the valves, which require a small amount of power. We have maintained quasi-passivity and added a variable stiffness feature of the elastic element. The major advantage of our proposed mechanism is that the change in stiffness is independent of the length of the lever arm, enabling the design of a smaller exoskeleton. All three studies have a spring with similar stiffness, falling within the range of the proposed device. It's important to note that the optimal stiffness changes based on the manner of walking, and the devices in Collins et al. and Yandell et al. require a manual exchange of springs. Since our range of stiffness can be adjusted, a smaller cylinder diameter and possibly a shorter stroke length can be chosen. This further reduces the overall weight, supporting the hypothesis that the mechanism is suitable for application in exoskeletons.

3.5 Chapter Conclusion

In this chapter, we introduced and analyzed a novel pneumatic quasi-passive mechanism capable of modulating stiffness using a unique method employing three valves. These valve combinations allow for transparent behavior, meaning that the pneumatic cylinder can be "deactivated". Moreover, the mechanism exhibits a high mass-energy storage capacity. A novel stiffness modulation method was theoretically presented, which accumulates air in the chamber without the need for a separate air supply. Through two experiments, we validated the theoretically presented method in the experimental setup by showing that accumulated air pressure simultaneously increases both the maximum stiffness and energy capacity in the quasi-passive mode of operation. This differs from linear helical springs, which are characterized by an inverse relationship between stiffness and energy storage capacity. Specifically, reducing the active length of the spring decreases its energy storage capacity. This is also true for current variable stiffness actuators used in robotics, as they predominantly use mechanical springs. Consequently, increasing spring stiffness results in decreased energy storage capacity. This relationship constrains the effectiveness of variable stiffness actuation technology in enhancing human performance in natural tasks, such as jumping, weight-bearing, and running, which require a spring exoskeleton with both a wide range of stiffness and high energy storage capacity. The first experiment confirmed changing the initial pressure with the proposed method, while the second experiment involved altering the position and thus confirmed the successful utilization of the air valve as a clutch in this application, demonstrating its ability to alter the effective length of the cylinder. Measurements obtained from the experimental setup were compared with the mathematical model, showing that the model provides a reasonable approximation of the behavior in each case. For certain precise applications, additional refinement of the theoretical pressure increments may be required. Furthermore, we conducted a quantitative comparison by proposing the mechanism's application to ankle exoskeletons and comparing it with existing solutions. This comparison strongly corroborates our findings. The presented results mark an important initial step, addressing several limitations of variable stiffness springs utilized in exoskeletons. The next chapter concentrates on devising a customized mechanical design to integrate this mechanism into an exoskeleton.

Chapter 4

Pneumatic Exoskeleton Joint Mechanism

The previous chapter introduced the fundamental concept of stiffness modulation within a pneumatic cylinder using three air valves to control the quantity of air inside without an external air supply. Building on this concept, this chapter details the design of an exoskeleton joint, incorporating additional components such as a pneumatic artificial muscle (PAM) to modify the lever arm and additionally shape the stiffness profile. Besides, the PAM functions as a soft air tank for accumulated air, with the hypothesis that this stored air can be reused. The pneumatic exoskeleton joint mechanism (PEJM), primarily designed for the knee, remains quasi-passive at this stage. This means electricity is only required to power the air valves, and there is no need for an external air supply. The hypothesis is that this mechanism can achieve a high energy storage capacity and modulate stiffness more effectively compared to the previous mechanism.

Exoskeletons found in the literature are often designed for clinical applications or augmenting healthy individuals [1]. They often incorporate variable stiffness actuators (VSA) to enhance adaptability and performance. The vast majority of VSAs have adopted the electromechanical manner of stiffness modulation, where usually, in addition to the main motor, a smaller one adjusts the stiffness [99]. Typically, stiffness variation in electromechanical VSA is achieved in several ways. The most commonly known ways are by changing the spring pretension [100]–[104], and by modifying the transmission between the load and the spring [107]–[110]. Variable stiffness actuators, in addition to providing active torque, can also store elastic energy in the spring and release it when needed, thereby increasing locomotion efficiency if used in exoskeletons or legged robots. This is analogous to human biological muscles, which generate active torque, and tendons, which store and reuse elastic energy to enhance the efficiency of locomotion.

However, these mechanisms to change the stiffness are often complex and thus have increased weight, which may consequently hinder exoskeleton performance [154]. Furthermore, most of variable stiffness actuators and mechanisms rely on linear helical springs, which are characterized by an inverse relationship between stiffness and energy storage capacity. Specifically, reducing the active length of the spring decreases its energy storage capacity. The stiffness range and energy storage capacity of a spring can be increased simultaneously by adding mass to the spring, for instance, in coil and leaf springs, this can be achieved by increasing the spring's thickness. However, in practical design, increasing the thickness of a coil or leaf spring is a complex task. This inverse relationship constrains the effectiveness of variable stiffness actuation technology in enhancing human performance in natural tasks, such as jumping, weight-bearing, and running, which require a spring with both a wide range of stiffness and high energy storage capacity, as theoretically described by Sutrisino et al. [149].

As an alternative to electromechanical actuators, pneumatic actuators offer a very attractive solution. The properties of pneumatic actuators resemble biological muscles due to the inherent compliance and high weight-to-power ratio, where stiffness is usually varied by applying different pressures to the actuator. One type of actuators used in pneumatic exoskeletons are pneumatic muscles (PAM) arranged in an antagonistic configuration [155], with on-board compressor [46], and custom designed with variable stiffness [94]. Work by [116], [156] showed how air can be used as a compressible elastic medium and that the stiffness of the actuator can be modulated by feeding controlled air masses into the chambers. Although these actuators offer many appealing options, the need for an air tank is often a challenge for the portability of exoskeletons.

To advance the current state of variable stiffness mechanisms, we developed the Pneumatic Exoskeleton Joint Mechanism (PEJM), which features stiffness modulation without the need for an external air supply, operating in a quasi-passive mode. This chapter presents an upgraded method of stiffness modulation. In this novel joint mechanism, accumulated air can be pumped to the pneumatic artificial muscle (PAM) to adjust the lever arm length and can also be reused from the PAM for further use.

The chapter is structured as follows: Section 4.1 details the design, theoretical analysis, and operating principle. Section 4.2 outlines the method of novel improved stiffness modulation. Section 4.3 delves into the experimental evaluation, while Section 4.4 discusses the results obtained. Section 4.5 provides a comparative analysis and discusses the application. Finally, the chapter concludes in Section 4.6.

The work from this chapter has been published in the IEEE Transactions on Mechatronics and Robotics [144].

4.1 Design and Operating Principle

In this section, the PEJM is presented by elaborating on the working principle and the mathematical model.

4.1.1 System Overview

The PEJM mechanism is shown in Fig. 4.1 integrated with the knee exoskeleton design. The working principle is based on the timely opening/closing of three air solenoid valves while using a pneumatic cylinder as a passive elastic element, allowing different behaviors, such as pressure increase or transparent motion. For example, transparent movement can be achieved by opening valve 1, or pressure can be increased if valve 2 is timely opened, resulting in air suction due to negative pressure. This valve function design is adopted from our previous work [143]. Furthermore, air can be pumped into the PAM by timely opening valve 3, which is deeper explained later in this paper. The PAM allows for varying the geometry, i.e., the effective length of the pneumatic cylinder. Moreover, the PAM can serve as a reservoir of compressed accumulated air. The synergy of both allows the torque and stiffness of the mechanism to be modified. Crucially, the compressed air needed to pump the PAM is generated within the cylinder by exploiting the dynamics of the body, so no external air supply is required. The upper end of the PAM is fixed, while its lower end can be repositioned on a linear slide. As compressed air is supplied to the PAM, it expands radially, becomes shorter in length, and thereby changes the position of the pneumatic cylinder base. The PAM also introduces additional compliance in the event of a mechanical singularity during joint rotation. Namely, the pneumatic cylinder has a limited stroke length after which a hard stop occurs. In this case, the PAM will begin to stretch when the end of the cylinder is reached.

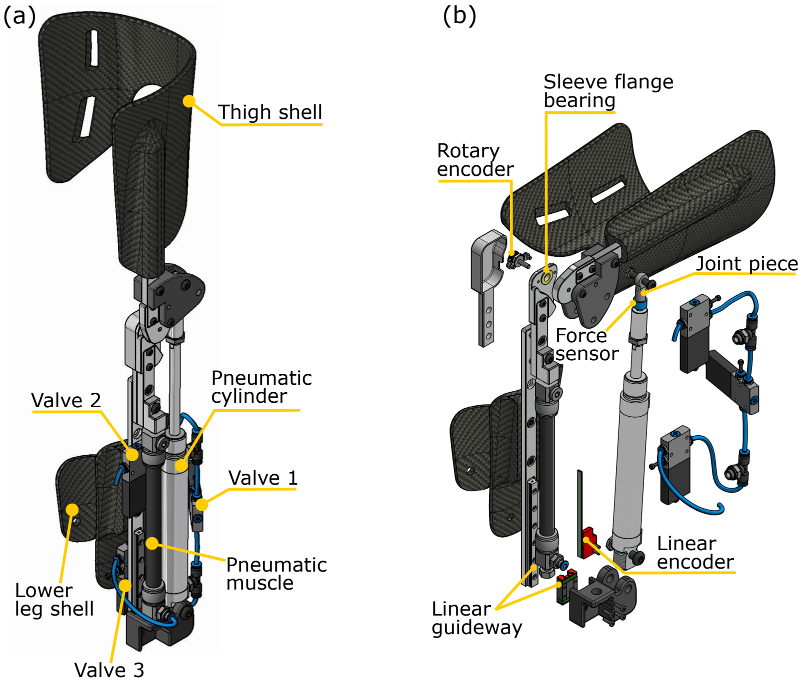

Figure 4.1: In (a) the PEJM CAD model applied to the knee exoskeleton, in (b) an exploded view.

4.1.2 Kinematic Analysis

In order to calculate the theoretical torque of the joint, it is necessary to identify the length change of the moment arm r during the joint rotation (Fig. 4.2). Therefore, this subsection deals with the mathematical modeling of r.

Let us define three points in the Cartesian coordinate system $\mathrm{P_b}(0,1)$, $\mathrm{P_j}(0,0)$ and $\mathrm{P_l}(0,-1)$. Additionally, it is necessary to define the two endpoints of the cylinder; A with coordinates $\mathrm{x_A}$ and $\mathrm{y_A}$, and B with coordinates $\mathrm{x_B}$ and $\mathrm{y_B}$. The coordinate $\mathrm{y_B}$ can be modified by shrinking the length of the PAM, whose length contraction is denoted by $\delta\mathrm{y}$. Bearing in mind that the positive theta angle θ corresponds to the clockwise rotation direction of the joint, the rotation matrix is given by

$$\mathrm{R}(\theta) = \begin{bmatrix} \cos\theta & \sin\theta \\ -\sin\theta & \cos\theta \end{bmatrix}. \tag{4.1}$$

Assuming that the upper leg rotates while the lower leg is stationary, the vectors $\vec{v}_\mathrm{b}$ and $\vec{v}_\mathrm{l}$ are given by the expression

$$\vec{v}_\mathrm{b} = \mathrm{R}(\theta)(\mathrm{P_b} - \mathrm{P_j}), \tag{4.2}$$

$$\vec{v}_\mathrm{l} = (\mathrm{P_l} - \mathrm{P_j}). \tag{4.3}$$

The coordinates of the point A' are obtained by adding the vectors $\vec{v}_\mathrm{r}$ and $\vec{v}_\mathrm{o}$ which are formulated as

$$\vec{v}_\mathrm{r} = \mathrm{y_A}\vec{v}_\mathrm{b}, \tag{4.4}$$

$$\vec{v}_\mathrm{o} = \mathrm{x_A}\mathrm{R}_{+90}\vec{v}_\mathrm{b}, \tag{4.5}$$

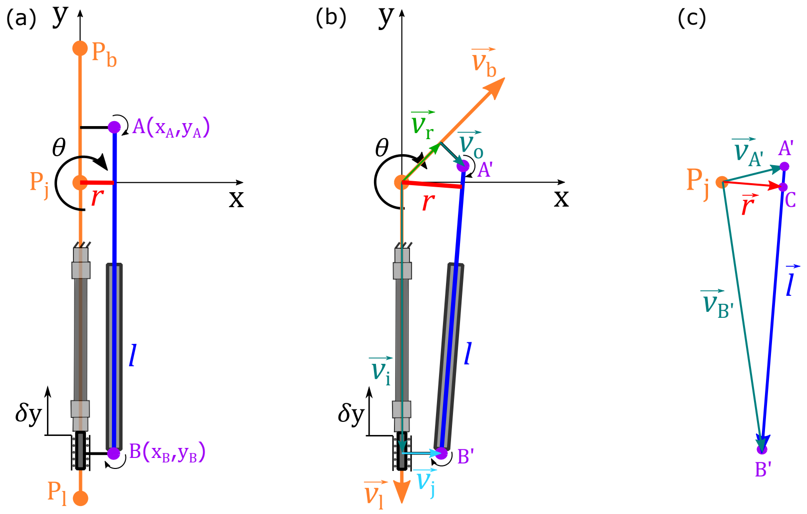

Figure 4.2: Kinematic model of the proposed mechanism. The point $\mathrm{P_j}$ marks the center of rotation and the origin. The perpendicular distance, denoted by r, between $\mathrm{P_j}$ and l represents the moment arm, and l is the length between the endpoints of the cylinder. (a) With $\theta = 0°$, (b) with $\theta \neq 0°$, and (c) the triangle $\Delta \mathrm{A'B'P_j}$ shows a more detailed representation of vectors.

where $\mathrm{R_{+90}}$ is the rotation matrix for 90 degrees clockwise, therefore the vector $\vec{v}_\mathrm{o}$ is perpendicular to $\vec{v}_\mathrm{b}$. Finally, the vector $\vec{v}_\mathrm{A'}$ is given by

$$\vec{v}_\mathrm{A'} = \vec{v}_\mathrm{r} + \vec{v}_\mathrm{o} = \mathrm{y_A}\vec{v}_\mathrm{b} + \mathrm{x_A}\mathrm{R_{+90}}\vec{v}_\mathrm{b}. \tag{4.6}$$

By following similar steps, the vector $\vec{v}_\mathrm{B'}$ can be expressed as the sum of the vectors $\vec{v}_\mathrm{i}$ and $\vec{v}_\mathrm{j}$ as follows

$$\vec{v}_\mathrm{i} = \mathrm{y_B}\vec{v}_\mathrm{l}, \tag{4.7}$$

$$\vec{v}_\mathrm{j} = \mathrm{x_B}\mathrm{R_{-90}}\vec{v}_\mathrm{l}, \tag{4.8}$$

$$\vec{v}_\mathrm{B'} = \vec{v}_\mathrm{i} + \vec{v}_\mathrm{j} = \mathrm{y_B}\vec{v}_\mathrm{l} + \mathrm{x_B}\mathrm{R_{-90}}\vec{v}_\mathrm{l}, \tag{4.9}$$

where $\mathrm{R_{-90}}$ is the 90 degree counterclockwise rotation matrix. Subtracting the vectors $\vec{v}_\mathrm{A'}$ and $\vec{v}_\mathrm{B'}$ gives the vector $\vec{l}$

$$\vec{l} = \vec{v}_\mathrm{B'} - \vec{v}_\mathrm{A'}, \tag{4.10}$$

whose length can be calculated using the Euclidean norm

$$\|\vec{l}\| = \sqrt{(\vec{v}_\mathrm{B'} - \vec{v}_\mathrm{A'})^2}. \tag{4.11}$$

To obtain the coordinates of point C, so that $\vec{r}$ is always perpendicular to $\vec{l}$, the expression for the minimum vertical vector between the point and the line is used

$$(\mathrm{P_j} - \mathrm{A'}) \cdot \hat{l} = |\mathrm{C} - \mathrm{A'}|, \tag{4.12}$$

where $|\mathrm{C} - \mathrm{A'}|$ means magnitude, and the unit vector $\hat{l}$ is given

$$\hat{l} = \frac{\vec{l}}{\|\vec{l}\|} = \frac{\vec{v}_\mathrm{B'} - \vec{v}_\mathrm{A'}}{\sqrt{(\vec{v}_\mathrm{B'} - \vec{v}_\mathrm{A'})^2}}. \tag{4.13}$$

Since the point $\mathrm{P_j}$ is the origin of the coordinate system, the coordinates of the point C are equal to the components of vector $\vec{r}$. Thus, by extracting C from Eq. (4.12) and drawing the vector $\vec{r}$ between the points $\mathrm{P_j}$ and C the expression for $\vec{r}$ is given

$$\vec{r} = \underbrace{\vec{v}_{\mathrm{A'}} + \big((\mathrm{P_j} - \vec{v}_{\mathrm{A'}}) \cdot \hat{l}\big)\hat{l}}_{\mathrm{C}} - \mathrm{P_j}, \tag{4.14}$$

whose length is computed as

$$\|\vec{r}\| = \sqrt{|r_{\mathrm{x}}|^2 + |r_{\mathrm{y}}|^2}. \tag{4.15}$$

4.1.3 Torque modeling

The torque $T_{\mathrm{tot}n}$ of the PEJM can be modified in steps denoted by the subscript n, which is introduced for easier distinction in the stiffness modulation strategy. In this subsection, the analytical torque model is derived, and the next subsection explains its modulation with steps and the PAM influence.

To analytically model the torque $T_{\mathrm{tot}n}$, it is first necessary to establish the correlation between the cylinder force and the chamber pressure during the joint rotation. The force $F_{\mathrm{tot}n}$ necessary to compress the pneumatic cylinder from the initial position z_0 to position z, with all three valves closed, is formulated according to Fig. 4.3:

$$F_{\mathrm{tot}n}(z, z_0, p_{\mathrm{in}}) = F_{\mathrm{c}n} + F_{\mathrm{u}n}, \quad z \in [z_0, z_{max}], n \in [0, M] \tag{4.16}$$

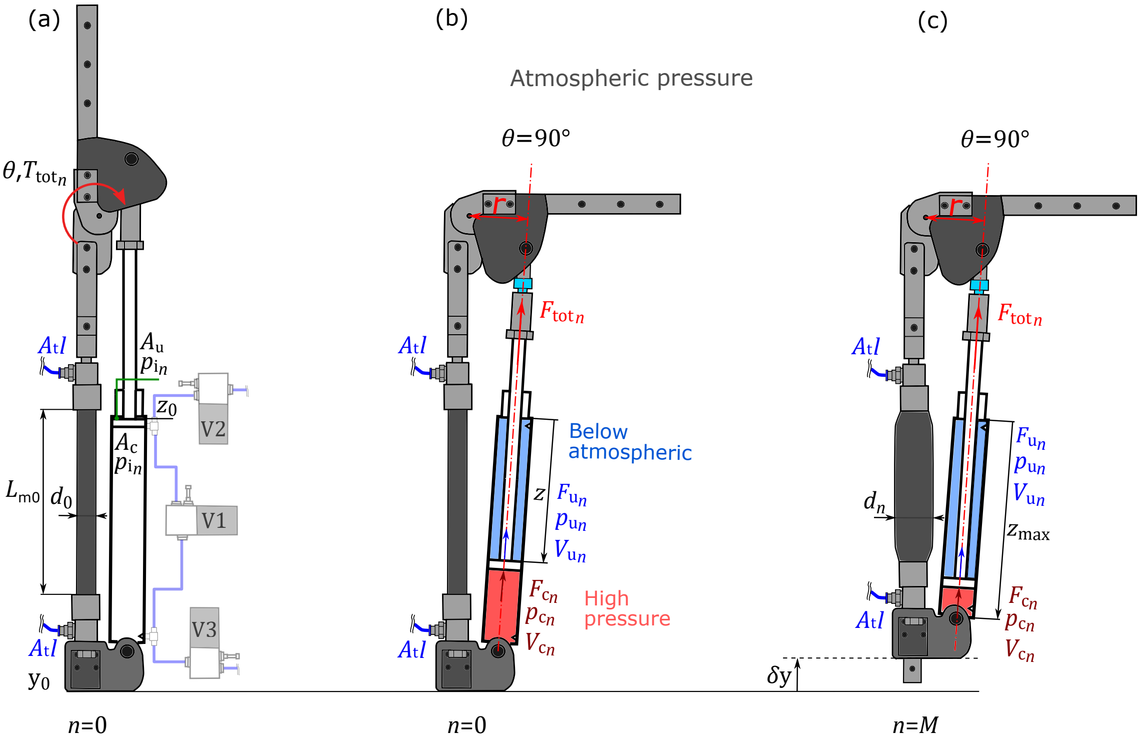

Figure 4.3: Joint rotation (θ) creates negative pressure ($p_{\mathrm{u}n}$) in the blue chamber, generating force $F_{\mathrm{u}n}$, while compressed air in the red chamber ($p_{\mathrm{c}n}$) produces force $F_{\mathrm{c}n}$. The total force ($F_{\mathrm{tot}n}$) generates torque $T_{\mathrm{tot}n}$ at the moment arm r that tends to return the mechanism to its initial state if all valves are closed. Pressurizing the PAM increases contraction (δy), leading to an increased total force $F_{\mathrm{tot}n}$ due to the increased dimension z.

where $F_{\mathrm{c}n}$ denotes the force produced by the compressed air $p_{\mathrm{c}n}$ that acts on the cross-sectional area A_{c}, and $F_{\mathrm{u}n}$ is the pulling force generated due to the underpressure $p_{\mathrm{u}n}$ that acts on the cross-sectional area A_{u} in the blue colored chamber. Supposing isothermal compression and neglecting the thickness of the piston, the pressure $p_{\mathrm{c}n}$ can be written as

$$p_{\mathrm{c}n} = p_{\mathrm{i}n} \frac{A_{\mathrm{c}}(z_{\mathrm{max}} - z_0) + A_{\mathrm{t}} l}{A_{\mathrm{c}}(z_{\mathrm{max}} - z) + A_{\mathrm{t}} l}, \tag{4.17}$$

where $p_{\mathrm{i}n}$ is the initial pressure in both cylinder chambers, the numerator equals the initial volume of the red chamber, where $A_{\mathrm{t}} l$ is the volume inside the air hose and the pneumatic connectors, and the denominator equals the final volume of the red chamber after joint rotation, and z_{max} is the maximum stroke of the cylinder. Equivalently, the pressure $p_{\mathrm{u}n}$ in the blue chamber equals

$$p_{\mathrm{u}n} = p_{\mathrm{i}n} \frac{A_{\mathrm{u}} z_0 + A_{\mathrm{t}} l}{A_{\mathrm{u}} z + A_{\mathrm{t}} l}. \tag{4.18}$$

Using the general gas equation, the initial pressure is given by the expression

$$p_{\mathrm{i}n} = \frac{N_{\mathrm{tot}n} R_{\mathrm{m}} T}{V_{\mathrm{cyl}}}, \tag{4.19}$$

where $N_{\mathrm{tot}n}$ represents the total amount of air in both cylinder chambers together, T is the air temperature in Kelvin, $R_{\mathrm{m}} = 8314$ J/kmolK is the universal gas constant, and V_{cyl} equals

$$V_{\mathrm{cyl}} = A_{\mathrm{c}}(z_{\mathrm{max}} - z) + A_{\mathrm{u}} z + 2A_{\mathrm{t}} l. \tag{4.20}$$

The pressure change in the cylinder, starting from $p_{\mathrm{i}n} = p_{\mathrm{atm}}$, is shown in Fig. 4.4.

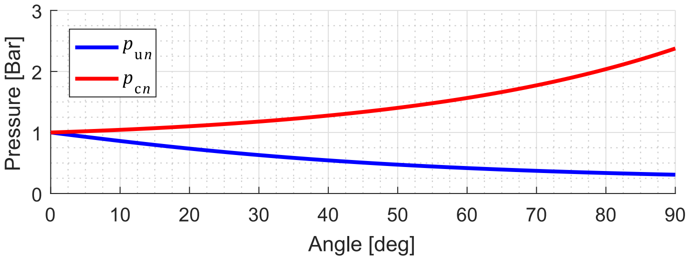

Figure 4.4: Pressure change in both cylinder chambers starting from the atmospheric pressure $p_{\mathrm{i}n} = p_{\mathrm{atm}}$. Underpressure is generated in the blue chamber, while air is compressed in the red chamber.

By inserting $p_{\mathrm{c}n}$, $p_{\mathrm{u}n}$ and $p_{\mathrm{i}n}$ into Eq. (4.16), the pneumatic cylinder force that can be modulated by changing z_0 or $p_{\mathrm{i}n}$ is now given by the following expression

$$F_{\mathrm{tot}n}(z, z_0, p_{\mathrm{i}n}) = p_{\mathrm{i}n} \left(\frac{A_{\mathrm{c}}(z_{\mathrm{max}} - z_0) + A_{\mathrm{t}} l}{A_{\mathrm{c}}(z_{\mathrm{max}} - z) + A_{\mathrm{t}} l} A_{\mathrm{c}} + \frac{A_{\mathrm{u}} z_0 + A_{\mathrm{t}} l}{A_{\mathrm{u}} z + A_{\mathrm{t}} l} A_{\mathrm{u}} \right). \tag{4.21}$$

The initial position z_0 is subject to changes depending on the length $L_{\mathrm{m}n}$ of the pneumatic muscle, while the $p_{\mathrm{i}n}$ can be varied by adding the extra air quantity in the pneumatic cylinder. Finally, the torque of the mechanism is given by

$$T_{\mathrm{tot}n} = F_{\mathrm{tot}n} \|r\|. \tag{4.22}$$

The change in force, moment arm, and torque with respect to the angle are shown in Fig. 4.5.

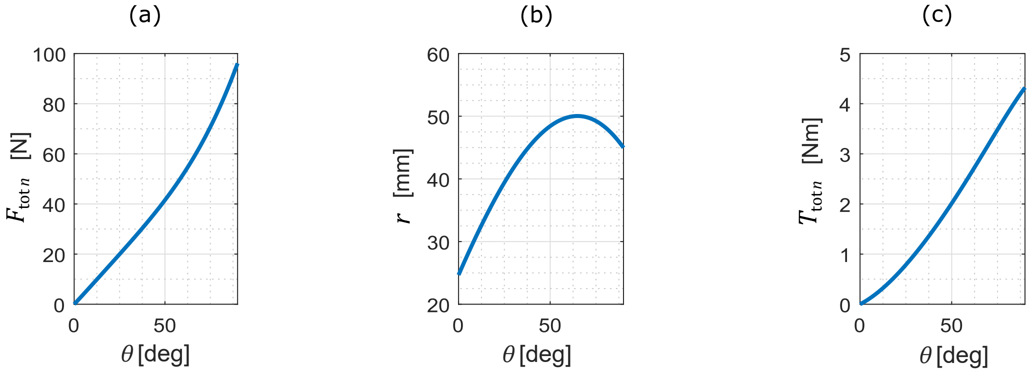

Figure 4.5: Theoretical profiles without stiffness increase ($p_{\text{i}n} = p_{\text{atm}}$, $\delta\text{y} = 0$); (a) Force in the cylinder, (b) Moment arm length, (c) Torque of the PEJM.

4.2 Novel Variable Stiffness Method

Stiffness modulation in the proposed mechanism is possible in two ways: 1) by changing the effective length of the pneumatic cylinder, i.e., by shortening the PAM, and 2) by changing the pressure $p_{\text{i}n}$ inside the pneumatic cylinder. Usually, both are combined and allow tuning of joint stiffness and torque. The behavior of the mechanism is determined by the valves, which open and close in a timely manner as the joint rotates (Fig. 4.6). The change in pressure of the cylinder chambers during rotation is exploited to modulate the initial pressure. As $p_{\text{i}n}$ increases, the joint becomes stiffer and can store more energy when deflected. The pressure increase is a process done in n steps where it is necessary to open valve 2 when the underpressure occurs, so that the atmospheric air ΔN_n enters the blue chamber at a pressure p_{atm} (see Fig. 4.6). Thus ΔN_n is given by the expression

$$\Delta N_n = \frac{p_{\text{atm}} A_{\text{u}} z}{R_{\text{m}} T}. \tag{4.23}$$

A new amount of air ΔN_n is now added to $N_{\text{u}n}$ that was already inside, given by the expression

$$N_{\text{u}n} = \frac{p_{\text{i}n} A_{\text{u}} z_0}{R_{\text{m}} T}, \tag{4.24}$$

where $N_{\text{u}n}$ is the amount of air in the blue (underpressure air) chamber. The amount of compressed air in the red chamber $N_{\text{c}n}$ can be analogously expressed as

$$N_{\text{c}n} = \frac{p_{\text{i}n} A_{\text{c}} (z_{\max} - z_0)}{R_{\text{m}} T}. \tag{4.25}$$

By returning to the initial position and opening valve 1, the air from both chambers is merged. Now the total increased amount of air in the whole pneumatic cylinder is

$$N_{\text{tot}n} = \Delta N_n + N_{\text{u}n} + N_{\text{c}n}. \tag{4.26}$$

An increased amount of air in the same volume will cause a change in pressure. Fig. 4.7 depicts an increase in the initial cylinder pressure $p_{\text{i}n}$ with steps. The value converges as soon as the pressure in the blue chamber becomes equal to p_{atm}, after which the air can no longer be sucked in. After the desired number of steps, the pressure can be pumped and stored in the PAM by opening valve 3. As the PAM is inflated, its volume increases and can be calculated using the expression given in [157], as follows

$$V_{\text{m}n}(L_{\text{m}n}) = \frac{L_{\text{m}n} L_{\text{f}}^2 - L_{\text{m}n}^3}{4\pi n_{\text{tu}}^2}, \tag{4.27}$$

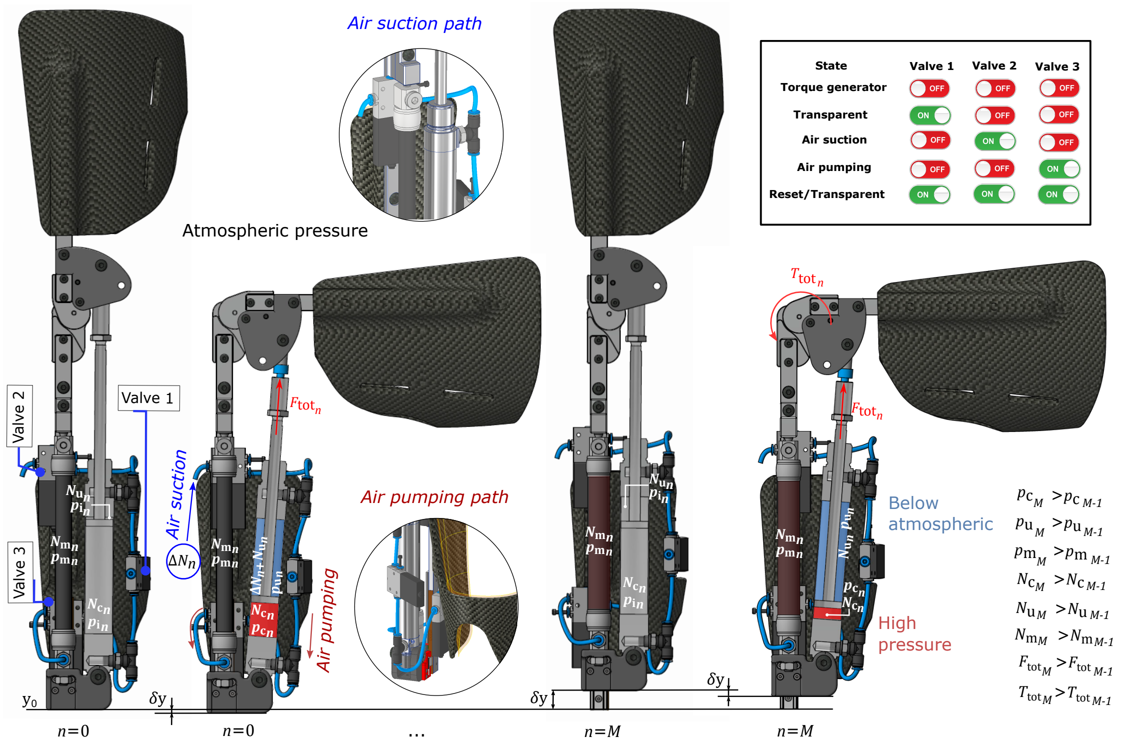

State	Valve 1	Valve 2	Valve 3
Torque generator	OFF	OFF	OFF
Transparent	ON	OFF	OFF
Air suction	OFF	ON	OFF
Air pumping	OFF	OFF	ON
Reset/Transparent	ON	ON	ON

Figure 4.6: Mechanism's stiffness modulation is a process done in n steps. For different valve combinations, different mechanism behavior is obtained. The blue marked cylinder chambers represent underpressure, while the red represents compressed air. When underpressure is generated, air ΔN_n enters the blue chamber by opening valve 2. When the amount of air in the cylinder increases, it can be pumped and stored in the pneumatic muscle by timely opening valve 3. Valve 1 acts as a clutch, by allowing free movement without generating force, as the air passes from one chamber to the other.

where n_{tu} is the number of thread turns, L_{f} is the thread length which can be calculated according to [47]. Assume that the initial pressure in the PAM is equal to p_{atm}, and $\delta \mathrm{y} = 0$, meaning that the length of the PAM is at the initial length $L_{\mathrm{m}0}$ and volume $V_{\mathrm{m}0}$. Then the initial amount of air in the PAM can be calculated as

$$N_{\mathrm{m}0} = \frac{p_{\mathrm{atm}} V_{\mathrm{m}0}}{R_{\mathrm{m}} T}. \tag{4.28}$$

By merging the volume of the cylinder V_{cyl} and assuming the volume of the PAM in the moment of opening valve 3 equals $V_{\mathrm{m}n} = V_{\mathrm{m}0}$, the total pressure in the system after n steps can be calculated as

$$p_{\mathrm{m}n} = \frac{(N_{\mathrm{m}0} + N_{\mathrm{tot}n}) R_{\mathrm{m}} T}{V_{\mathrm{m}0} + V_{\mathrm{cyl}}}. \tag{4.29}$$

Now the initial pressure in the cylinder and also the pressure in the PAM is $p_{\mathrm{m}n}$. Fig. 4.7 shows the increase in pressure when the PAM is pressurized in a volume-coupled manner. This means that the PAM maintains the pressure in the cylinder once increased and is acting on the cross-sectional area A_{c}. If now valve 3 closes, the PAM pressure can be computed only if the exact relation $V_{\mathrm{m}n}(L_{\mathrm{m}n})$ is known where $L_{\mathrm{m}n} = f(p_{\mathrm{m}n}, F_{\mathrm{m}n})$. With a known PAM pressure its length $L_{\mathrm{m}n}$ can be estimated by using the FESTO table or any other PAM models [47], [157]. However, once the force in the cylinder exceeds the static

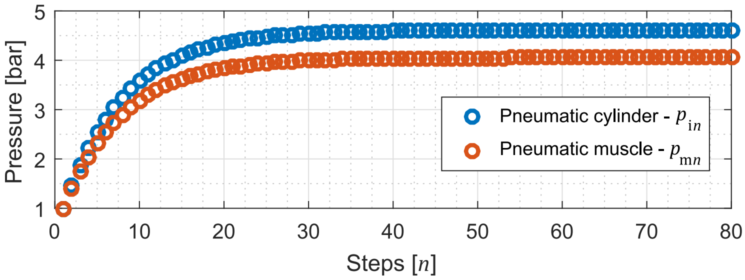

Figure 4.7: As air is gradually drawn in, the initial cylinder pressure $p_{\text{i}n}$ rises until $p_{\text{u}n}$ equals p_{atm}, indicating no more air can enter the chamber. The pressure can be increased in desired steps n, followed by valve 3 opening to share the pressure with the pneumatic muscle, denoted as $p_{\text{m}n}$.

force of the PAM, it starts to stretch in a non-linear way. Modeling this dynamic behavior is beyond the scope of this thesis. The theoretical model within the scope of this thesis does not consider the dynamics of the PAM, but only considers the PAM as an element that has the role of modifying the effective length of the cylinder in the same way as it was a rigid slide without elastic properties. Experimental results will identify the dynamics of the mechanism as a whole.

The derivative of torque with respect to the deflection can be used to determine the stiffness of the mechanism

$$k_n = \frac{\partial T_{\text{tot}n}}{\partial \theta}. \tag{4.30}$$

Finally, to obtain the value of storable energy, the following expression is used

$$H_n = \int_0^\theta T_{\text{tot}n} d\theta. \tag{4.31}$$

The figures illustrate theoretical torque, stiffness, and energy modulation with two methods: 1) by changing the initial pressure $p_{\text{i}n}$, shown in Fig. 4.8, and 2) by changing the effective length of the pneumatic cylinder by shortening the PAM, shown in Fig. 4.9.

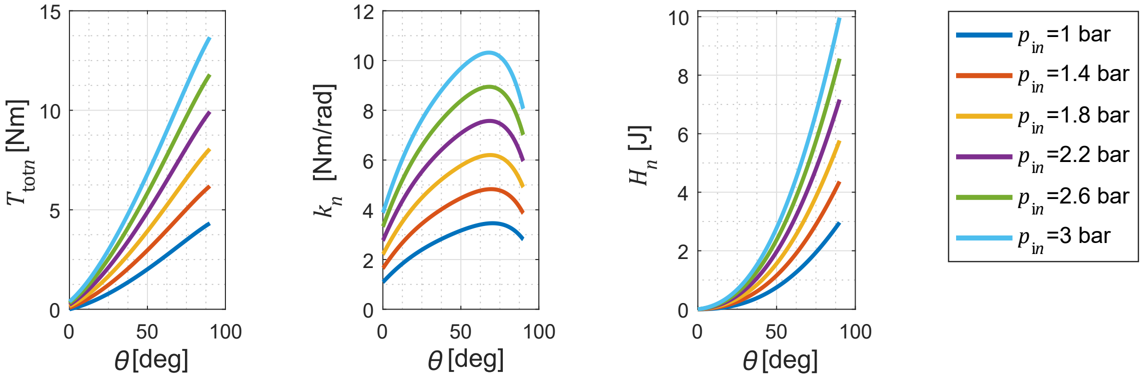

Figure 4.8: The increase in the initial cylinder pressure $p_{\text{i}n}$ increases the torque $T_{\text{tot}n}$, torsional stiffness k_n, and storable energy of the mechanism H_n.

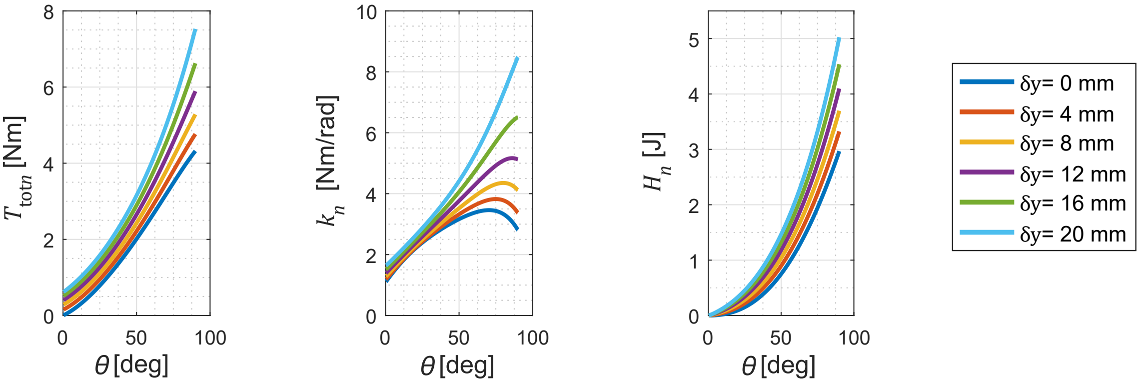

Figure 4.9: The contraction of the pneumatic muscle δy alters the effective length of the cylinder, impacting the force and consequently influencing the torque $T_{\text{tot}n}$, torsional stiffness k_n, and storable energy H_n of the mechanism.

4.3 Experimental Setup for the Joint Mechanism

This section discusses the mechatronic design of the experimental setup, gives an insight into the control, and explains the experiments.

4.3.1 Mechatronic Design of the Experimental Setup

To evaluate the performance of the mechanism and validate the theoretical concepts, an experimental test platform was constructed, with a scheme shown in Fig. 4.10. In the following text, each unit is briefly described.

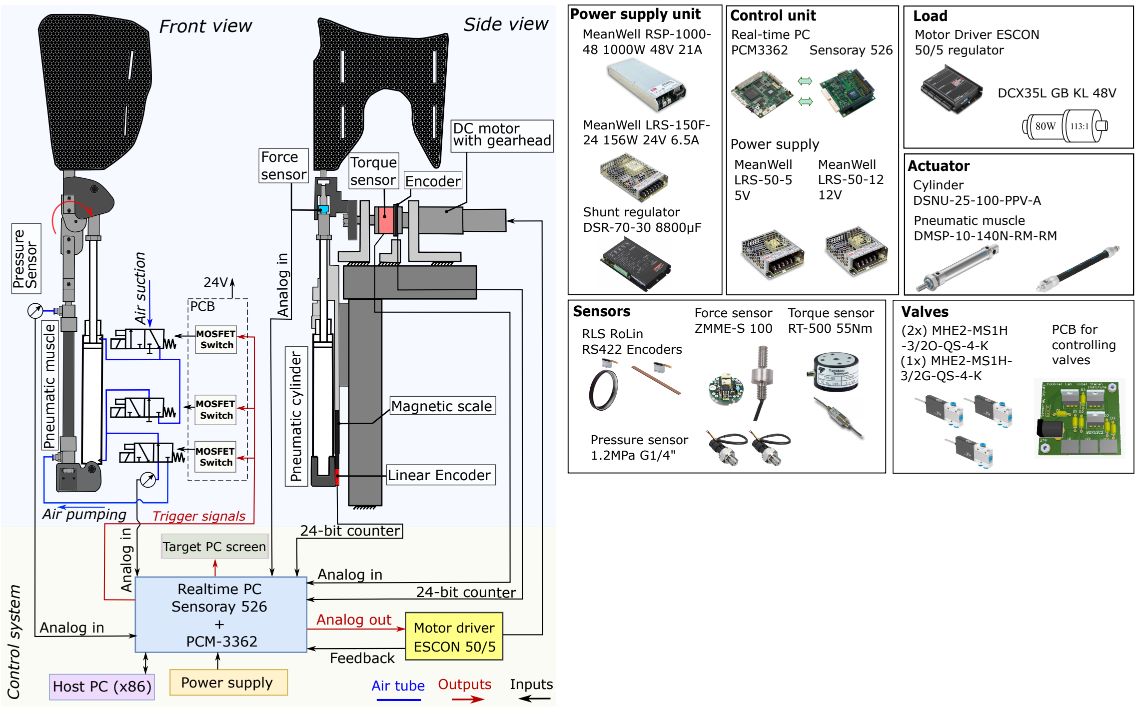

Figure 4.10: Experimental platform schematic with components. The control system is highlighted in yellow, output signals in red, and input signals in black.

Load: A brushed DC motor (DCX35L, Maxon) with planetary gear GPX42C, 113:1 ratio, is rigidly attached to the joint and serves as the load for the PEJM evaluation. The motor driver, ESCON 50/5, allows high-fidelity control in either velocity or current mode as the reference is sent from an external device to its analog input pins.

Sensors: The torque sensor (RT-500, Tovey Engineering) is placed at the output of the gear and connects it to the exoskeleton mechanism. On the same axis, there is also a rotary encoder (RLS RoLin RS422) for measuring the rotation angle. The same type of readhead is mounted to measure the linear displacement of the PAM. A force sensor, ZMME-S 100, with a nominal force of 1000 N is installed on the piston rod to measure the force in the pneumatic cylinder during rotation. Two sensors are set up to monitor the pressure; one to measure the compressed air in the cylinder and the other to measure the pressure in the PAM.

Valves: Three air solenoid valves with a maximum switching frequency of 330 Hz are controlled by MOSFET transistor switches. They are open or closed depending on the signal sent, *"high"* or *"low"*. Valve 2 is 3/2 monostable MHE2-MS1H-3/2G-QS-4, and valve 1 and 3 are 3/2 monostable, MHE2-MS1H-3/2O-QS-4-K.

Control Unit: The central controller consists of PCM-3362 PC-104 with Sensoray 526 data acquisition card, which also provides four programmable counters for the incremental encoders and eight A/D converters. The system is compatible with Simulink Real-Time, which enables real-time control at 1000 Hz. Data is collected on the host computer and analyzed.

Actuator: The pneumatic cylinder used in the mechanism is DNSU-25-100-PPV-A with a 25 mm bore and a total stroke length of 100 mm. The pneumatic muscle (DMSP-10-140N-RM-RM, FESTO) has a diameter of 10 mm, and an initial length of 140 mm.

4.3.2 Controller Structure

In order to facilitate the experiments, the stateflow control logic was devised, shown in Fig. 4.11, which receives as input: the desired mode that determines the experiment, the encoder signal θ_{ext}, the derived encoder signal, i.e., rotation speed $\dot{\theta}_{\text{ext}}$, pressure sensor readings p_{cyl} and p_{m}, and finally the manually selected desired PAM pressure $p_{\text{m,des}}$. The stateflow logic determines, based on the input signals, the timing for opening or closing the solenoid valves and when to switch the motor from the repetitive sequence to the standby state. The motor rotation speed information is acquired by deriving the encoder signal and employing the velocity observer as a filtering mechanism. When the PAM pressure p_{m} is to be increased, the algorithm compares it with the desired pressure $p_{\text{m,des}}$. The cylinder pressure p_{cyl} is compared with p_{m} to find the optimal time to open valve 3 and pump the compressed air, which is further explained in the experiments. Upon the completion of each experiment, the STOP block is automatically set to a high value. The Simulink Real-Time™ system is used in such a way that the desired control block diagram is uploaded from the host PC via an Ethernet cable to the target PC (PCM-3362). A position feedback controller with a feedforward term is used to ensure the motor's positioning accuracy during the measurements. The motor driver, ESCON 50/5, was initially set to velocity mode. The encoder signal is read on the Sensoray 526, stacked on the PCM-3362, where the feedback loop is closed. With the encoder position feedback θ_{ext}, a PD controller outputs the desired motor velocity, which is then sent to the motor driver as an analog signal in the ±10V range. The motor control algorithm can therefore be summarised as

$$u_{pos} = k_f \dot{\theta}_{\text{p,des}} + \text{PD}(\theta_{\text{p,des}} - \theta_{\text{ext}}). \tag{4.32}$$

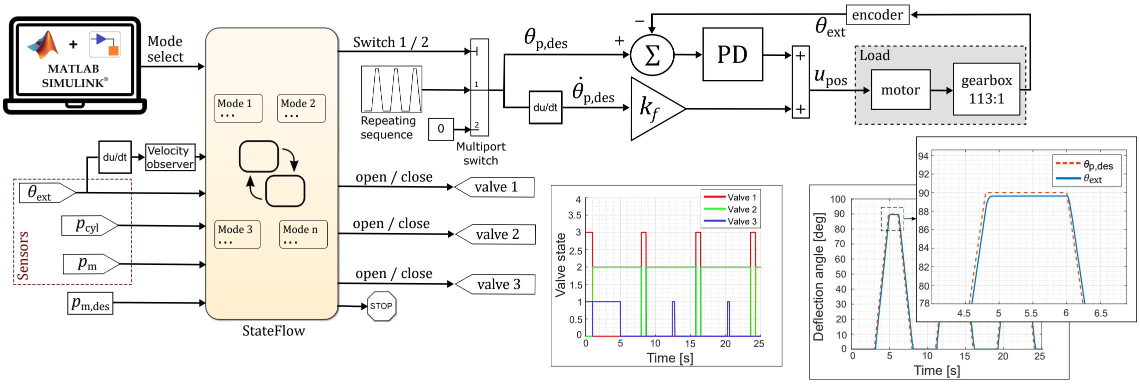

Figure 4.11: Control block scheme of the experimental setup. Sensor signals are inputs to the stateflow, where the algorithm decides when to open/close valves and switch the motor from the repetitive sequence to the standby state. A PD controller with feedforward term achieves the desired motor position, using the encoder signal for feedback. Valve amplitudes are either high or low, but scaled for illustration.

4.4 Experimental Procedure and Results

Multiple experiments were conducted to assess the performance of the mechanism, utilizing the test platform depicted in Fig. 4.12. The desired motor position is a repeated sequence signal, where a rotation from 0° to 90° occurs within 1.8 seconds, followed by a 1.2-second position hold, and a subsequent return to the initial position within 1.8 seconds. A period lasts for 7.8 sec. Simultaneously, the stateflow algorithm determines when to switch valves on and off based on the information provided by the sensors. The sensors collected the data during the experiments. In the post-analysis, the data were filtered using a Butterworth filter, after which stiffness and stored energy were calculated as the derivative and integral of the torque and deflection angle, respectively. In the following text, the

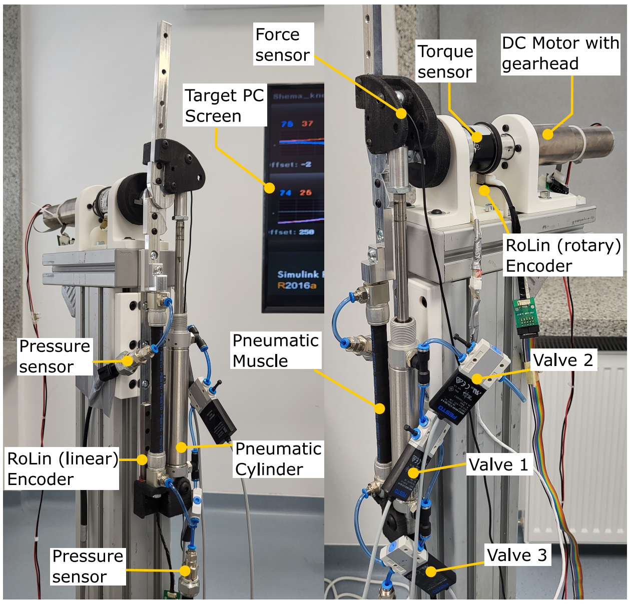

Figure 4.12: Actual experimental setup with all parts marked.

algorithm within the stateflow is provided only for more complex experiments, offering a clearer understanding of valve combinations, while less complex ones are described in words. The remainder of this section explains the conducted experiments and presents the corresponding results.

4.4.1 Basic Mechanism Verification

The basic function of the mechanism was evaluated for different valve states and compared with the theoretical values. The motor followed the above-mentioned desired repeating position trajectory with a) all three valves closed, b) valves 1 and 3 closed, and valve 2 open, c) valves 1 and 2 closed and valve 3 open. The results are shown in (Fig. 4.13). The graphs indicate that the theoretical models closely approximate the experimental results for all three cases. In accordance with theory, when only valve 2 is open, the cylinder force has a progressive characteristic due to compressed air in the bottom chamber, with torque peaking at ∼3 Nm (Fig. 4.13b). However, when only valve 3 is open, the cylinder force has a degressive characteristic with a peak torque of ∼1 Nm (Fig. 4.13c). Finally, in the third case, with all valves closed, the values are the highest with a peak torque of ∼4.5 Nm (Fig. 4.13a). The basic function of the mechanism was further investigated for different initial cylinder pressures with all three valves closed (Fig. 4.14). Between each rotation of the joint, the relative pressure in the cylinder was increased from 0 bar to 1.46,

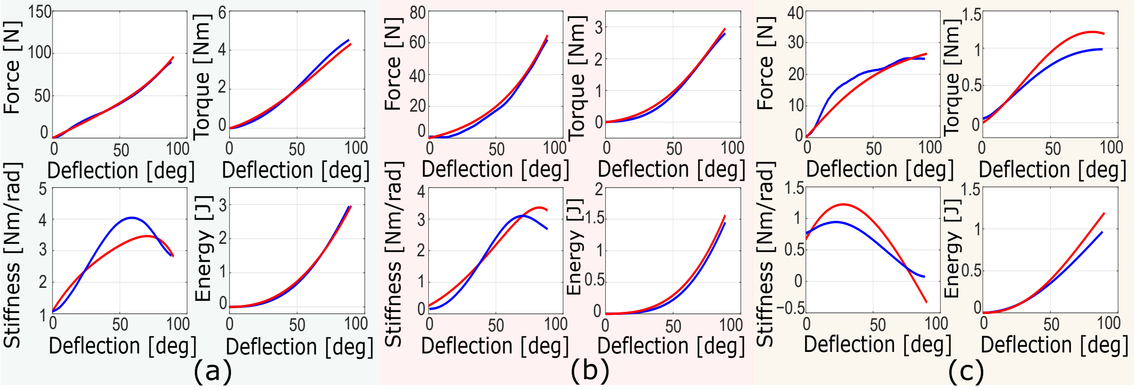

Figure 4.13: Basic mechanism verification; (a) With all three valves closed, (b) valves 1 and 3 closed and valve 2 open, and (c) valves 1 and 2 closed and valve 3 open. Red line: theoretical values, blue line: measured values.

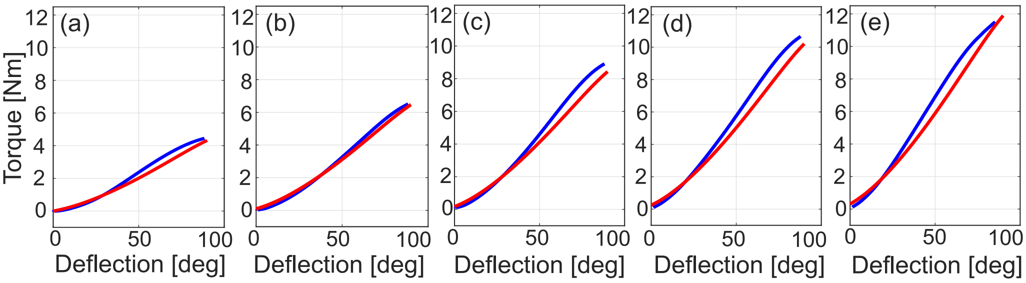

Figure 4.14: Basic mechanism verification with different initial pressures and all valves closed. Blue line: measured torque-deflection profiles, red line: theoretical values. Relative initial pressure in the pneumatic cylinder: (a) 0 bar, (b) 1.46 bar, (c) 1.88 bar, (d) 2.26 bar, and (e) 2.62 bar.

1.88, 2.26, and 2.62 bar. The results are compared with the mathematical model. The values correlate favorably for each pressure increase.

4.4.2 Pneumatic Cylinder Pressure Increase

The great feature of the proposed PEJM is that it can modify the cylinder pressure using human body dynamics or actuated load, as in the present experiment. To accomplish this, the valves must be timely turned on and off. For clarity, the experiment description is given along with the stateflow algorithm depicted in Fig. 4.16a. In this experiment, four sequences were done; with each one, the air was sucked into the cylinder, to increase pressure. The results are given in Fig. 4.15a and Fig. 4.15b, where the first one shows

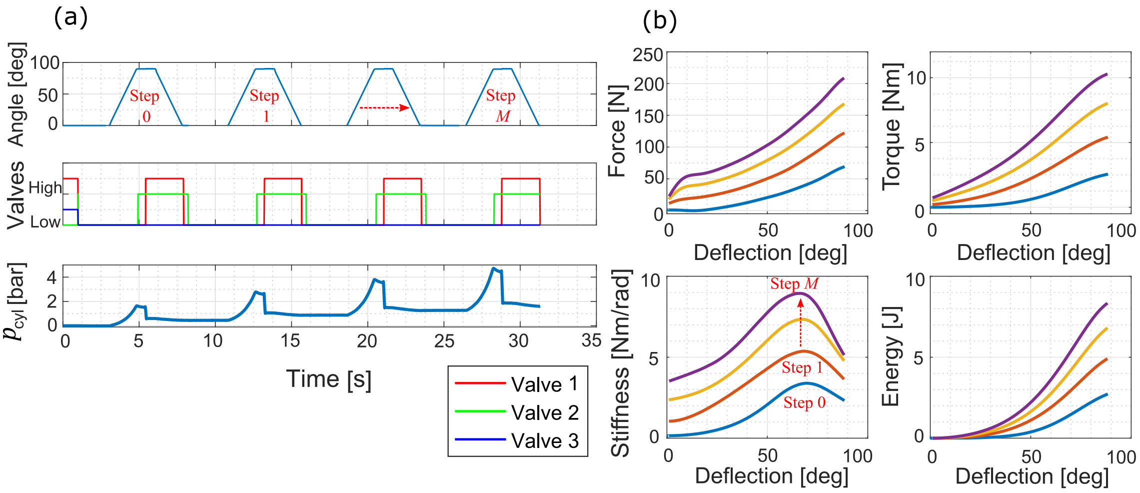

Figure 4.15: Pneumatic cylinder pressure increase. In (a) motor angle, valve states, and pressure in the cylinder. In (b) measured force and torque with the calculated torsional stiffness and stored energy versus deflection.

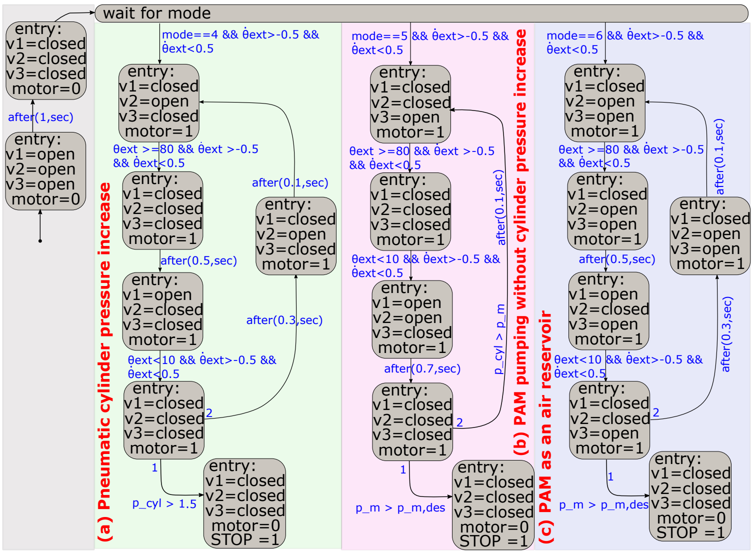

Figure 4.16: Stateflow algorithm for experiments: (a) Pneumatic cylinder pressure increase, (b) PAM pumping without cylinder pressure increase, (c) PAM as an air tank.

the motor angle, the state of the valves, and the pressure in the cylinder, while the latter delivers the measured force and torque as well as the calculated torsional stiffness and stored energy. A *"high"* state of valve 1 means open airflow, while a *"low"* state means airflow is closed. The same applies to valve 3, as the valve is the same. Conversely, a *"high"* state of valve 2 means the airflow is closed, while a *"low"* state means an open airflow. In the experiment, the target cylinder pressure was set to higher than 1.5 bar, after which the experiment stopped. After four steps, the pressure in the cylinder increased from 0 bar to ∼1.6 bar (relative pressure) in equilibrium and to ∼4.7 bar in compression due to joint rotation. In four steps, the stiffness increased ∼164% from a peak value of ∼3.4 Nm/rad to ∼9 Nm/rad and torque from ∼3 Nm to ∼10 Nm. A step-wise stiffness modulation by adding air in the pneumatic cylinder is stressed with red arrows from Step 1 to Step M. Each step corresponds to one rotation of the motor, offering a graphical representation of the stiffness adjustment speed through step increments. These values support the concept of cylinder pressure increase.

4.4.3 PAM pumping

There are various methods to pump the PAM. For instance, one can pump it immediately after increasing the cylinder pressure, increase the cylinder pressure multiple times before pumping, or not increase the cylinder pressure at all. Two different ways of pumping PAM have been experimentally performed: without increasing the cylinder pressure and by increasing the cylinder pressure for two strokes beforehand, where the target cylinder pressure was set to higher than 0.8 bar. The algorithm for the first experiment is given in Fig. 4.16b, while the second experiment can be understood as a combination of (a) and (b) in Fig. 4.16. In addition, the opening time of valve 3 is conditioned by $p_{\mathrm{cyl}} > p_{\mathrm{m}}$, which ensures smooth pumping without jerking of the PAM during rotation. The results for the former are shown in Fig. 4.17a, and for the latter in Fig. 4.17b. The results indicate that when the cylinder pressure was increased, PAM pumping occurred faster (peak ∼3.4 bar at 68 sec), while when there was no previous pressure increase, the PAM pressure peaks ∼1.6 bar at 68 sec. In (a), the slight increase in cylinder pressure with each stroke is finely seen. This was due to the PAM contraction δy, which also progressively increased. The

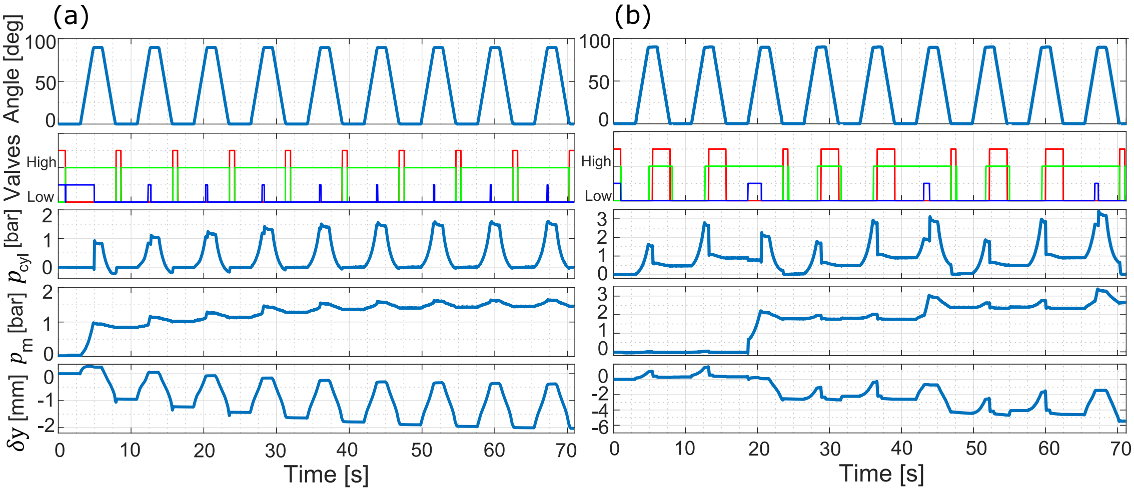

Figure 4.17: Two different ways of PAM pumping. In (a) without cylinder pressure increase, and in (b) with two strokes of cylinder pressure increase. Valve 1 is shown in red, valve 2 in green, and valve 3 in blue.

PAM contraction δy peaks ∼2.1 mm at 70 sec without cylinder increase, while with the previous increase, it peaks ∼5.9 mm at 70 sec. These results further extend our knowledge of PAM pumping.

4.4.4 PAM as an Air Tank

The third variant of PAM pumping is where the PAM keeps the cylinder constantly pressurized, effectively acting as a compressed air tank. The algorithm used in the experiment is given in Fig. 4.16c. The target PAM pressure was pre-set to 2 bar (relative pressure) and was reached after six steps (Fig. 4.18a). The results in Fig. 4.18b show the measured cylinder force and joint torque with stiffness and stored energy, where the stiffness-deflection graph indicates the step-wise stiffness modulation with red arrows highlighting the joint rotations, thus providing insight into the stiffness adjustment speed. In six steps, the joint torque increased from a peak of ∼1.3 Nm at zero PAM pressure to ∼10 Nm at 2 bar PAM pressure. In the same number of steps, stiffness increased from ∼1.4 Nm/rad to ∼6.5 Nm/rad, indicating a ∼364% increase. The stiffness peak has shifted from ∼72° to ∼52°, accounting for a ∼28% change.

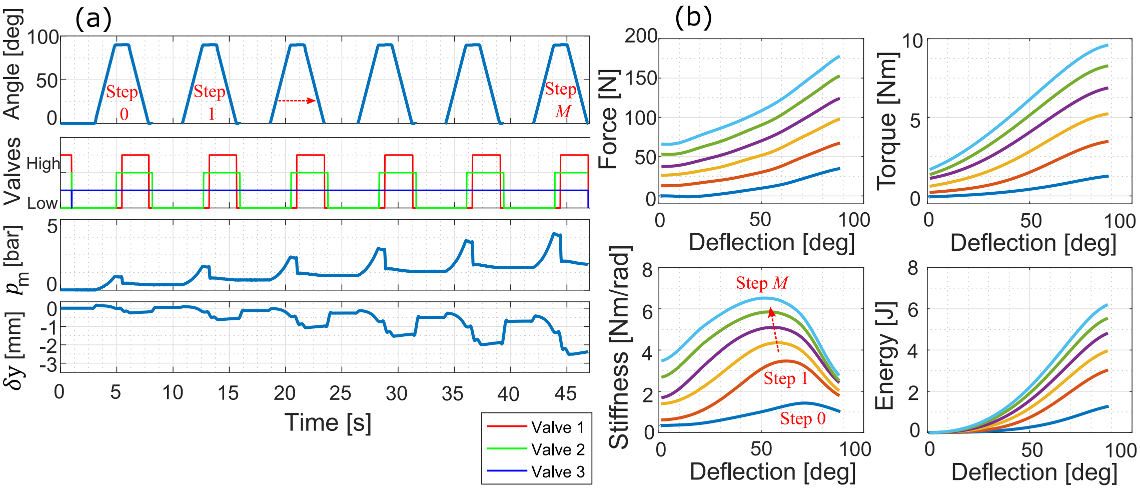

Figure 4.18: PAM as an air tank. In (a) with shown motor angle, valve states, pressure in PAM, and contraction. In (b), measured force and torque with the calculated torsional stiffness and energy stored versus deflection.

4.4.5 Pumping PAM Using an External Pump

To determine the extent to which shortening the PAM influences stiffness compared to air accumulation via the pneumatic cylinder, we decoupled the two methods and used an external pump to inflate the PAM without involving the air accumulation with the pneumatic cylinder. The joint was rotated seven times, with PAM pumping occurring between each rotation (except the first one). The measured force, torque, calculated stiffness, and stored energy with deflection are shown in Fig. 4.19b, while Fig. 4.19a shows the measured pressures in the cylinder and PAM, along with the PAM contraction. The pressure in the cylinder increased from ∼1.6 bar in the first rotation to ∼2.3 bar in the last joint rotation due to the change in the effective length of the cylinder. The PAM was pumped to 5 bar, with a maximum contraction of ∼15 mm. Between each rotation, the cylinder force and joint torque increased at the angle of 0° as the PAM contraction compressed the air inside the cylinder without rotating the joint. The stiffness increased from ∼3.8 Nm/rad to ∼4.8

Nm/rad by shortening the PAM by 15 mm. This suggests that stiffness can be adjusted more rapidly by increasing the initial pressure in the pneumatic cylinder rather than by altering the length of the cylinder.

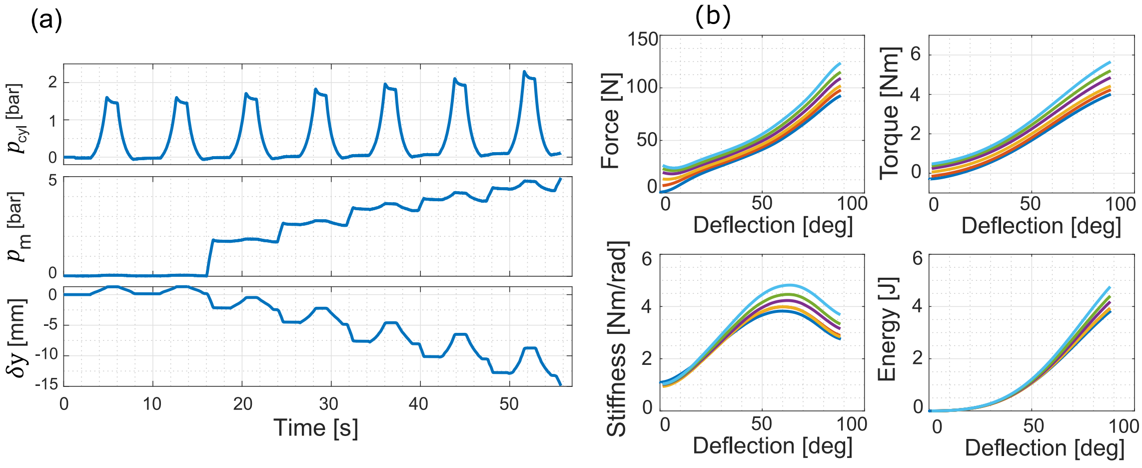

Figure 4.19: PAM inflation by a cordless pump. In (a) the experimental setup is illustrated. In (b) measured force and torque with calculated torsional stiffness and stored energy versus deflection.

4.4.6 Temperature Variation Effect

To examine the effect of temperature on the joint torque, a temperature experiment was conducted on the PEJM. The mechanism was heated from an initial room temperature of ∼22°C to ∼65°C over a duration of 60 seconds. The heating was performed using a hair dryer, with all valves closed and the joint angle set at 0°. An analog temperature sensor, TMP36, was used to monitor temperature variations. The pressure in the cylinder, PAM, and temperature are shown in Fig. 4.20. The results show the relative pressure increase from 0 bar to ∼0.07 bar in the cylinder and to ∼0.04 bar in the PAM. Since the PAM inflates the volume due to the pressure increase, its pressure increase was lower than in the hard shell pneumatic cylinder with a constant volume. These values show that the temperature change has a low impact on the mechanism's pressure.

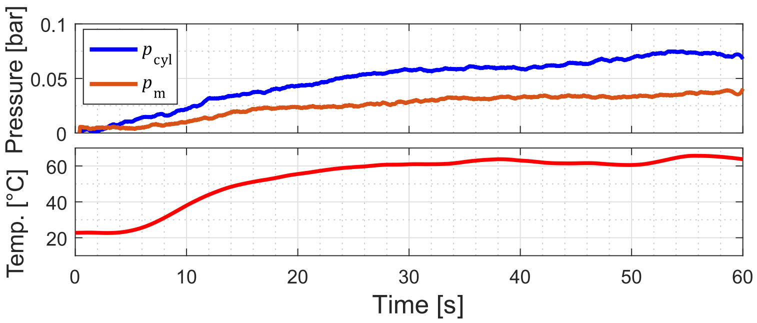

Figure 4.20: Temperature variation effect on cylinder and PAM pressure.

4.4.7 Leak Analysis

The leak test was performed for 180 minutes with a constant joint rotation, where the initial pressure was atmospheric. The motor was set to a repeating sequence as before. The maximum pressure at the end of compression was monitored during the experiment to check if the pressure decreased with time. The results in Fig. 4.21 show that the pressure decreased from ~1.55 bar to ~1.47 bar over 180 min, suggesting that the air leakage has a small impact on the performance of the device, especially considering that the air can be recovered from the atmosphere by opening the valve.

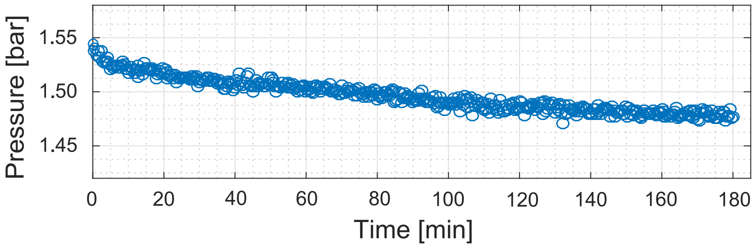

Figure 4.21: Cylinder pressure loss by constant joint rotation over 180 min.

4.5 Discussion

This section presents a comparative analysis to discuss the advantages and disadvantages of the proposed mechanism in relation to existing work.

Table 6.1 details the relevant parameters of the proposed PEJM mechanism. The initial observation of particular note is the remarkably low weight, only 0.76 kg for one side. This encompasses the entire exoskeleton, excluding the leg shells and electronic system. Nonetheless, it's important to acknowledge that achieving portability necessitates a compact 24V battery to power the valves. These valves operate on minimal current for trigger signals (0.09-0.44 mA). The peak torque is attained with a maximum pressure in the cylinder of 8 bar, coinciding with the peak stiffness and energy storage capacity.

Table 4.1: Parameters of the proposed PEJM

PARAMETER	**VALUE**	**UNIT**
Total weight[1]	0.76	[kg]
Max. Pressure	8	[bar]
Max. Torque[2]	15.94	[Nm]
Stiffness range	0 - 13.19	[Nm/rad]
Energy storage capacity	0 - 10.3	[J]
Deflection angle	0-135	[deg]
Size	551x38x75	[mm]

[1] Exoskeleton weight breakdown: air cylinder (238g), valves (60g,3x), PAM (80g), mechanical parts, without leg shells (264g).

[2] Obtained at max. pressure of 8 bar.

A comparison is made with the variable stiffness actuators listed in Table 4.2, and graphically illustrated in Fig 4.22. The comparison focuses on their characteristics rather than their specific application contexts and types. Among these actuators, only the PVSA and PEJM are pneumatic, while the others use mechanical stiffness modulation methods.

Table 4.2: Comparison with different variable stiffness actuators

Actuator	**Stiffness [Nm/rad]**	**Weight [kg]**	**Max. Torque [Nm]**	**Deflect. range [deg]**	**Max. Energy [J]**
vsaSDR [101]	127-2095	4	18	±1.3	0.45
BAVS [102]	3.9-146.6	0.75	8	±18.2	0.9
VSA-Cube [103]	3-14	0.26	3	±15.8	0.047
MACCEPA [104]	5-110	2.4	70	±60	27.9
PLVL-VSA[107]	0-49	1.9	22.5	±20	3
AwAS-II [108]	0-∞	1.4	80	±17	5.8
vsaUT-II [109]	0.7-948	2.5	60	±40.1	0.19
SVSA [110]	1.7-150	2.4	22.11	±45	3.7
PVSA [156]	0.86-5.04	1.95	10.6	±120	5.8
PEJM	**0-13.19**	**0.76**	**15.94**	**±135**	**10.3**

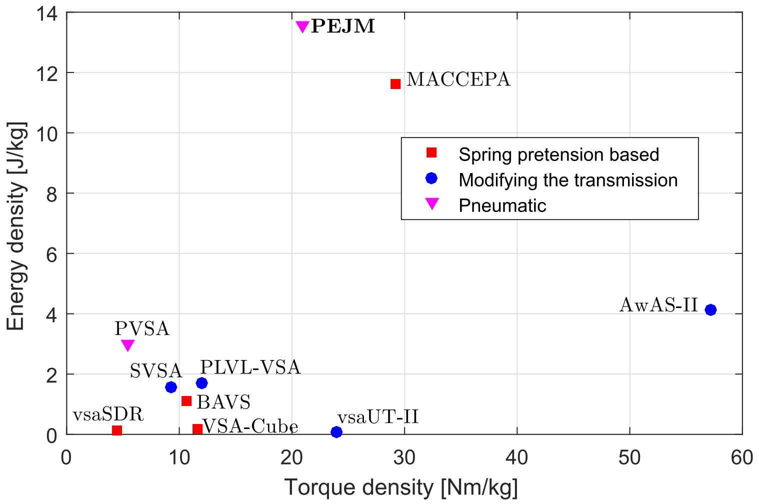

Figure 4.22: Graphical comparison of other VSAs with PEJM.

Although VSAs with mechanical stiffness modulation have the advantage of a wide torque bandwidth and precise stiffness control, they require the integration of many additional mechanical components, such as an additional motor and mechanical springs, which can increase the weight and thus the inertia of the joint. Pneumatic actuators generally require an external air supply to change stiffness. However, the PEJM is an exception, as it can accumulate air internally and use it to adjust stiffness. Moreover, mechanical VSAs are limited in geometry. Typically, mechanisms that provide a large stiffness variation do not allow a large deflection from the equilibrium position. With a large deflection, the mechanism to vary the stiffness must also be larger, and therefore it is sometimes technically impossible to achieve both a large stiffness variation and a large deflection. It is therefore a trade-off between stiffness variation and deflection and thus stored energy. The advantage of the proposed PEJM is that it requires very little energy to hold the stored energy and can be safely discharged by opening the valve, which is usually difficult with VSAs. Additionally, the mechanism exhibits a high energy storage density, which is 16.5% higher than the second-highest, MACCEPA. This feature is especially beneficial for exoskeletons and legged robots that store and return energy to improve efficiency. Notably, the PEJM is solidly in the middle range for torque density. While the weights of other actuators are listed without a power source, the same applies to the PEJM. However, unlike the others, the PEJM requires only minimal power, allowing for a lighter power source. In contrast, DC motors typically need larger and heavier power sources due to the significant power required to drive them. The mechanism and method of stiffness modulation are not without limitations. One drawback of the PEJM is the slower time required to increase stiffness, which must be done incrementally, making it impractical in some scenarios. However, this can be mitigated by adding an external pump to pre-inflate the PAM. However, experimental results showed that accumulating air in the pneumatic cylinder increases stiffness much faster than pumping the PAM. Additionally, mechanical VSAs can precisely control stiffness using an external motor, while the PEJM does not have a motor and instead relies on controlling the cylinder's engagement position and increasing pressure to modulate stiffness.

4.5.1 Application

In practical applications, the proposed knee exoskeleton is envisioned to provide knee support in individuals with various neurological or musculoskeletal conditions. The concept is illustrated in Fig. 4.23, where stiffness adjustments could be tuned to different body weights and levels of impairment. Using the stiffness modulation methods presented in this chapter, a suitable stiffness profile could be achieved. This application shares similarities with the Ottobock C-Brace® (Fig. 2.5), a commercially available device employing a hydraulic actuator. Pneumatic systems offer some potential advantages, including smaller weight, easier maintenance, safety, and cost-effectiveness. However, pneumatic devices generally exert lower forces compared to hydraulic systems. Therefore, they may be more suitable for individuals with mild to moderate impairments. In contrast, the Ottobock C-Brace® accommodates a broader spectrum, including severe impairments, despite being heavier at 3.2 kg compared to our device.

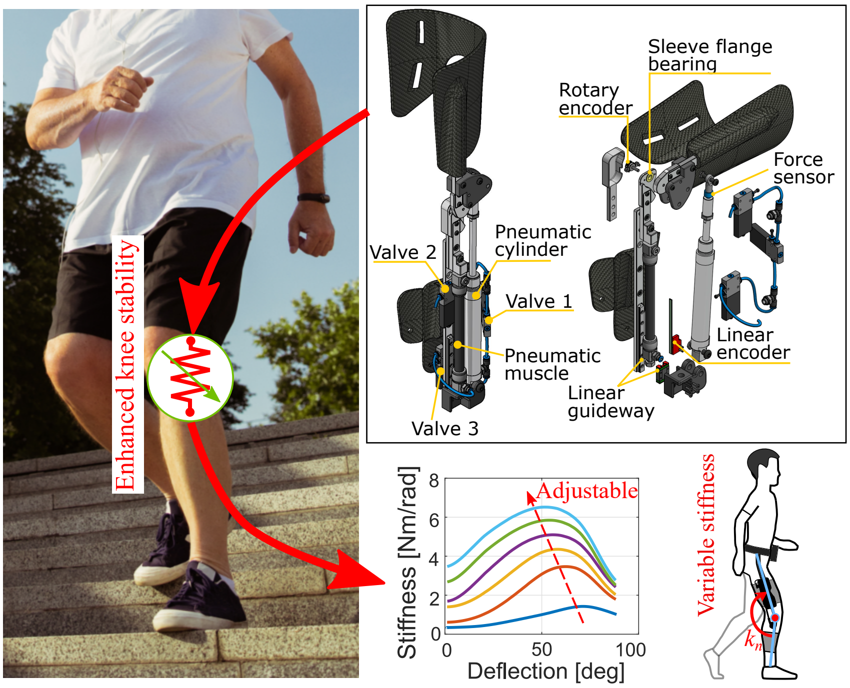

Figure 4.23: Application of the PEJM in a knee exoskeleton. Left image source: www.freepik.com

4.6 Chapter Conclusion

In this chapter, a newly proposed pneumatic exoskeleton joint mechanism (PEJM) for an exoskeleton was evaluated. The goal was to develop a lightweight pneumatic mechanism with a self-sufficient air tank capable of modulating stiffness. In practical applications, this translates to the knee exoskeleton with an adjustable level of support for stability. The mechanism can also accumulate air incrementally, a process feasible during walking as one example. The mathematical model of the mechanism was given. The results of the experiments confirmed the theoretical model with only minor deviations. We found an innovative method to modulate the stiffness, in which the air can be accumulated in the pneumatic cylinder and stored in the PAM, making the mechanism independent of an external air supply and therefore portable. In addition, the results have shown that the mechanism has excellent energy density and favorable torque density. However, the stiffness modulation might be slower than in the electromechanical VSA-a, due to the step-wise modulation. The results so far have been promising and support our hypothesis that the PEJM is a good candidate for knee or other types of exoskeleton. The following chapter will detail the complete prototype of the exoskeleton and test it on humans.

Chapter 5

Knee Exoskeleton with Bidirectional Energy Flow

This chapter introduces the knee exoskeleton prototype, which operates in both active and quasi-passive modes. In quasi-passive mode, energy can flow bidirectionally between the exoskeleton and the user, allowing for energy harvesting in the form of compressed air and thereby increasing energy efficiency. This functionality is demonstrated through sit-stand tasks. While existing literature encompasses exoskeleton-assisted sit-stand tasks [38], [158]–[161], the integration of energy recovery mechanisms remains unexplored. To push the boundaries further, this study introduces a portable pneumatic knee exoskeleton that operates in both quasi-passive and active modes, where active mode is utilized for aiding in standing up (power generation), thus the energy flows from the exoskeleton to the user, and quasi-passive mode for aiding in sitting down (power absorption), where the device absorbs and can store energy in the form of compressed air, leading to energy savings in active mode. The absorbed energy can be stored and later reused without compromising exoskeleton transparency in the meantime. In active mode, an air pump inflates the pneumatic artificial muscle (PAM), which stores the compressed air, that can then be released into a pneumatic cylinder to generate torque.

Figure 5.1: A person wearing the JSI-KneExo, published in [145].

Efficient energy utilization is a crucial consideration in every technical system. Human joints can both generate and absorb power, which opens up the space for energy recovery. For example, regenerative exoskeletons can capture otherwise wasted human energy and produce electricity when backdriven by joint movements during negative power intervals [54], [120], [122], [162], [163]. While most of these devices primarily target energy recovery during walking, Laschowski et al. [164] highlighted the potential of energy recovery during sitting transfers where the hip, knee, and ankle power is almost entirely negative, while standing up requires positive joint power [87]. Existing solutions cover exoskeletons-assisted stand-to-sit tasks, yet without any energy recovery [38], [158]–[161]. This absence in the literature may be attributed to the large number of required sitting repetitions in order to notice the effect, mainly because of the limited efficiency in converting mechanical to electrical power. Namely, robotic exoskeletons could theoretically regenerate ∼26 joules per single sitting task, meaning that with 60 repetitions, this merely extends the exoskeleton operation by around ∼0.7% [164]. Another, more efficient, type of energy storing and reusing is found in quasi-passive exoskeletons which absorb kinetic energy within elastic components during negative power intervals and subsequently return it to the joints in positive power intervals with the help of clutches [23], [26], [33], [34], [54], [143], [149]. This process minimizes losses as kinetic energy is directly converted into elastic energy and vice versa. Yet, even though highly efficient in energy recovery, they cannot produce net positive work like robotic actuators, and relying solely on recovered energy may sometimes be insufficient.

However, pneumatic actuators, like cylinders, exhibit the versatility to function as both elastic components (air springs) and force-generating actuators. This implies they could provide a good pathway for combining efficient energy recovery with the ability to produce positive net mechanical work. Moreover, the air is a lightweight elastic medium that can be easily passed to another energy reservoir and stored. Therefore, when positive power generation is required, a portion of the stored air can be retrieved from a storage tank, minimizing the need for additional compressed air generation by the pump, thus reducing energy consumption.

In an optimal scenario, exoskeleton-assisted sit-stand task include: assistance with energy absorption (in the Exo) when sitting down, efficient energy storing for future use, enabling transparency without energy loss, and actively assisting in standing up partially reusing stored energy, which would reduce overall consumption. To achieve this, we design a portable pneumatic exoskeleton that operates as active, quasi-passive, and transparent while keeping energy. In the literature, pneumatic actuators have been utilized in the active [165], [166] and quasi-passive exoskeletons [34], [143], [144]. They are appealing due to their high weight-to-power ratio, inherent compliance, and high brackdrivability. Still, when used as active the necessity for an air tank poses portability challenges for pneumatic exoskeletons. Notably, a few prior studies have successfully devised active portable pneumatic exoskeletons integrating onboard air compressors and metal air tanks; [46] weighing 9.12 kg, [41] weighing 9.95 kg. Our previous work developed a method for modulating air spring stiffness by drawing air from the atmosphere without an air pump or supply. The method was applied in the variable stiffness joint mechanism [144]. Here we introduce, the JSI-KneExo with key **contributions** as follows:

1. Introducing an Exo that enables bidirectional energy flow between the user and exoskeleton, allowing highly efficient energy recovery in the form of compressed air while simultaneously assisting the user. Energy recovery ultimately leads to big overall energy savings.

2. Design is enabled by a pneumatic air regenerative actuator integrated into a lightweight,

> slim, and portable knee exoskeleton that can switch between different modes, such as active, quasi-passive, or transparent, which is mathematically described.

The chapter is structured as follows: Section 5.1 describes the mechatronic design. The mathematical model is introduced in Section 5.2. The concept of energy recovery is explained in Section 5.3. Section 5.4 presents a pilot study involving an able-bodied subject performing sit-to-stand tasks, along with the results. The discussion is provided in Section 5.5. Finally, the chapter concludes in Section 5.6.

The work was published at the IEEE International Conference on Robotics and Automation (ICRA) and presented in Yokohama, Japan in 2024 [145].

5.1 Overview of the Exoskeleton

5.1.1 Exoskeleton Design

The JSI-KneExo (Fig. 5.2a) is a modular system made up of three major components: the left-leg exoskeleton with an actuator, the right-leg exoskeleton with an actuator, and the control unit. Depending on the application, one or both legs of the exoskeleton may be used simultaneously. The whole system weighs 3.9 kg (each leg of the exoskeleton 1.25kg and the control unit 1.4kg). The range of motion is 0 - 135°.

5.1.1.1 Actuator Unit

The actuator (Fig. 5.2b) comprises a pneumatic cylinder (DNSU-25-100-PPV-A, FESTO, Germany), which generates force when pressurized air enters its chamber. As the cylinder is attached to the shank and thigh levers, the force in the cylinder causes torque in the

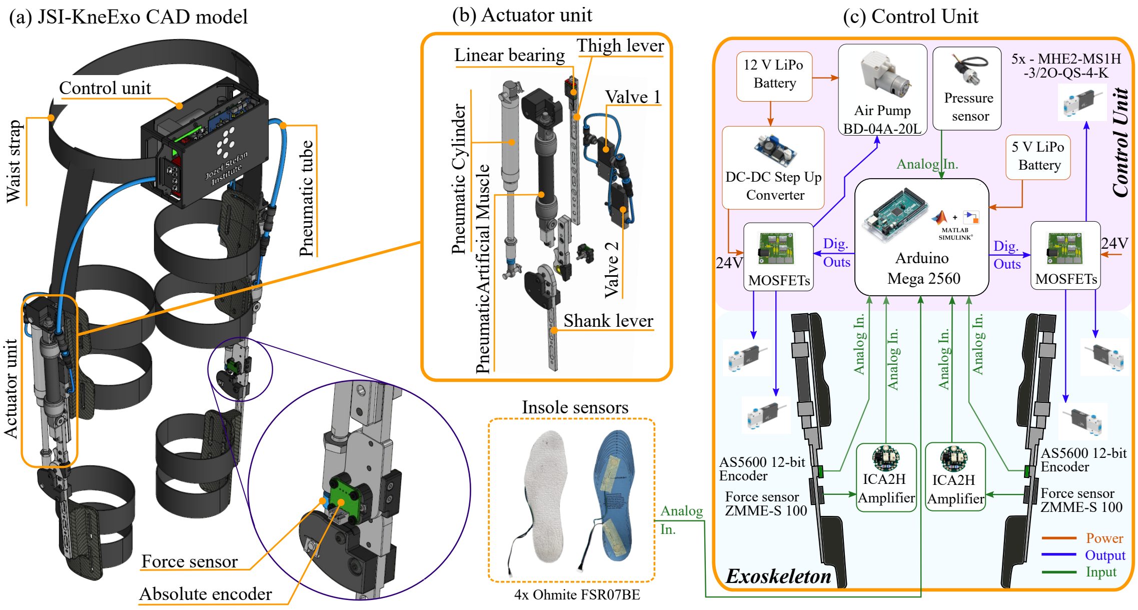

Figure 5.2: (a) The JSI-KneExo comprises three modular parts: control unit, left-leg exoskeleton, and right-leg exoskeleton. (b) The actuator unit incorporates air solenoid valves, PAM, pneumatic cylinder, force sensor, absolute encoder, shank and thigh lever, and a linear bearing facilitating linear PAM deflection. (c) Pink background highlights control unit components, while light blue denotes exoskeleton (leg side) components; optional insole sensors can be added.

joint with a maximum value of 20 Nm at a maximum pressure of 8 bar. The cylinder has a maximum stroke of 100 mm and a bore diameter of 25 mm. The compressed air generated by the air pump is stored in the pneumatic artificial muscle (PAM), DMSP-20-100N-RM-RM (initial diameter 20mm, initial length 100mm), which when inflated shrinks its length and increases its diameter. The PAM's lower end is fixed, upper-end slides on the linear bearing. Each unit contains two solenoid air valves (MHE2-MS1H-3/2O-QS-4-K, FESTO, Germany) for state change, as detailed further in the chapter. The absolute encoder AS5600 (ams-OSRAM AG, Austria) measures the joint angle, while the cylinder force is measured by the force sensor ZMME-S100 (Zhiminsensor, China).

5.1.1.2 Control Unit

The control unit is shown in (Fig. 5.2c). The JSI-KneExo is fully portable as the compressed air is supplied by the air pump BD-04A-20L, BodenFlo, China, powered by a 12 V LiPo battery with a capacity of 3.4 Ah. If running continuously, the pump has an autonomy of ∼3.4 h. Six MOSFET switches, arranged in two PCBs control solenoid valve positions. An extra solenoid valve is included in the control unit box, the function of which is explained in the next section. A pressure sensor is integrated to continuously monitor the pressure in both PAMs. The voltage is converted to 24 V for the solenoid valves by the DC-DC converter. The main microcontroller is an Arduino Mega 2560.

5.1.1.3 Pneumatic Multimodalities

The portable pneumatic circuit is shown in Fig. 5.3. All five solenoid valves are identical and monostable, transitioning smoothly between '1' and '2' positions with a ∼2 ms frequency. The air pump generates compressed air, which charges the PAM, and pressure is tracked using a sensor. The valve P depressurizes the tube after air pumping; otherwise,

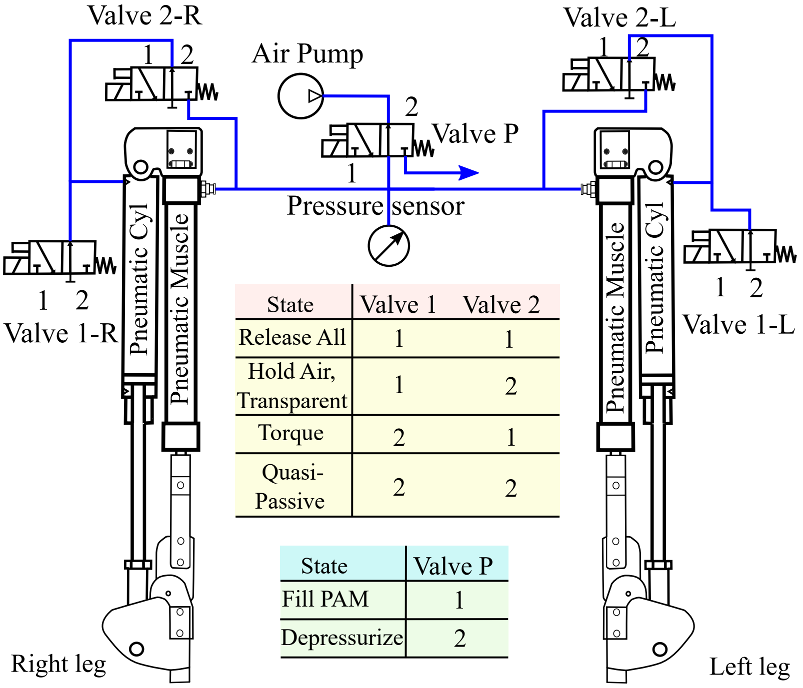

State	Valve 1	Valve 2
Release All	1	1
Hold Air, Transparent	1	2
Torque	2	1
Quasi-Passive	2	2

State	Valve P
Fill PAM	1
Depressurize	2

Figure 5.3: Pneumatic circuit of the JSI-KneExo. Different valve positions achieve different exoskeleton states.

by restarting the pump the reverse pressure holds the pump back when it needs the most power. Symmetrical pneumatic connections exist on both sides (left and right). Different valve combinations achieve various states. For example, in "Release all" both valves 1 and 2 are set to ’1’, allowing atmospheric pressure to enter the cylinder and PAM, resulting in air release. The second state, "Hold Air, Transparent," involves the air pump filling the PAM to the desired pressure set in the control algorithm, but valve 1 has a clutch function, meaning that if in position ’1’ the pneumatic cylinder appears transparent as the chamber is connected to the atmosphere and air cannot be compressed. After being in the transparent state, by setting valve 2 to ’1’, compressed air enters the cylinder chamber, producing force and joint torque. It’s crucial to revert valve 1 to ’2’ to prevent air discharge. This state is called "Torque" or active mode. The last state is the "Quasi-passive", in which both valves are set to position ’2’. Torque is generated as the air inside the cylinder is compressed by knee flexion, acting as a nonlinear progressive compression spring resisting rotation. Furthermore, in this state, compressed air can be returned to the PAM by flexing the joint and switching valve 2 to ’1’ so that air flows back into the PAM.

5.2 Mathematical Model

5.2.1 Air Pump

The air pump has the function of charging the PAM with compressed air to the desired pressure. Commercially available air pumps are rated for no-load air flow at 0 bar pressure. Therefore, it is hard to calculate the time required to fill the PAM as the pressure increases. Another approach involves experimentally identifying the pressure-time profile. Hence, two air pumps were experimentally identified and compared: BD-04A-20L (maximum pressure: 3.32 bar, 20 L/min flow rate at 0 bar) and the air piston pump BD-07A-35L (maximum pressure: 6.5 bar, 35 L/min flow rate at 0 bar). Fig. 5.4 depicts the measured pressure-time profile when filling the pneumatic muscle DMSP-20-100N-RM-RM for both pumps.

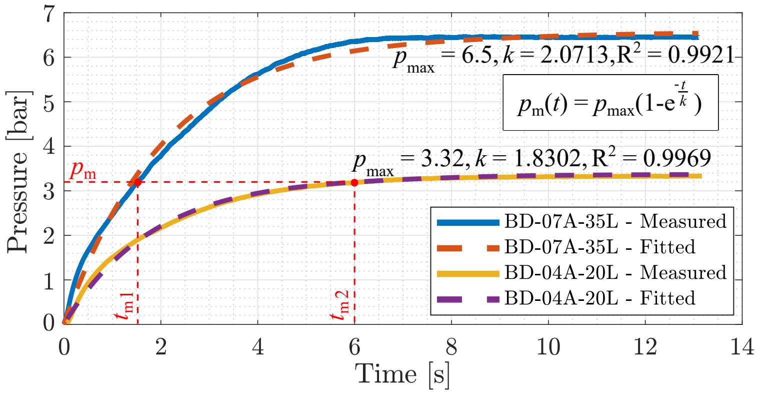

Figure 5.4: Filling compressed air into the PAM with two different pumps, the larger BD-07A-35L and the smaller BD-04A-20L. The equation fitted through measured data has the form: $p_{\mathrm{m}}(t) = p_{\max}(1 - e^{-t/k})$. For the larger pump: $p_{\max} = 6.5$ bar, $k = 2.0713$, and $R^2 = 0.9921$. For the smaller pump: $p_{\max} = 3.32$ bar, $k = 1.8302$ and $R^2 = 0.9969$.

The measured data were fitted with the following exponential function:

$$p_{\mathrm{m}}(t) = p_{\max}(1 - e^{-\frac{t}{k}})\,, \tag{5.1}$$

where $p_{\mathrm{m}}(t)$ is the actual pressure at time t, $p_{\max}$ is the max. nominal pressure for the pump, and k is the pump constant identified for both pumps. The coefficient of determination is $\mathrm{R}^2 = 0.9921$ for BD-07A-35L and $\mathrm{R}^2 = 0.9969$ for BD-04A-20L. The time t_m required to reach the desired pressure p_m in the PAM can now be determined using Eq. (5.1).

5.2.2 Pneumatic Artificial Muscle (PAM)

When the air gets compressed inside the PAM, its length L_m and volume V_m change. The analytical dependency $V_\mathrm{m}(L_\mathrm{m})$ is known and adopted from [157]. However, with a known PAM pressure p_m its length L_m can only be estimated from the FESTO datasheet for the exact PAM or other existing PAM models [47], [157]. Since FESTO does not provide an analytical model, the PAM model was determined experimentally. The dependency between the pressure p_m, length L_m, and the volume V_m is needed to compute the actuator's torque. Therefore, the model was determined experimentally by compressing air into the PAM and measuring the contraction ε. The PAM force was zero during the identification as the linear bearing allows unrestrained contraction. The experimental identification is shown in Fig. 5.5, where (a) shows the measured contraction ε as a function of PAM pressure p_m, and (b) shows the analytical model linking PAM volume V_m and contraction ε, given in Eq. (5.3), for different contractions where the maximum contraction for the chosen PAM is equal to 25%.

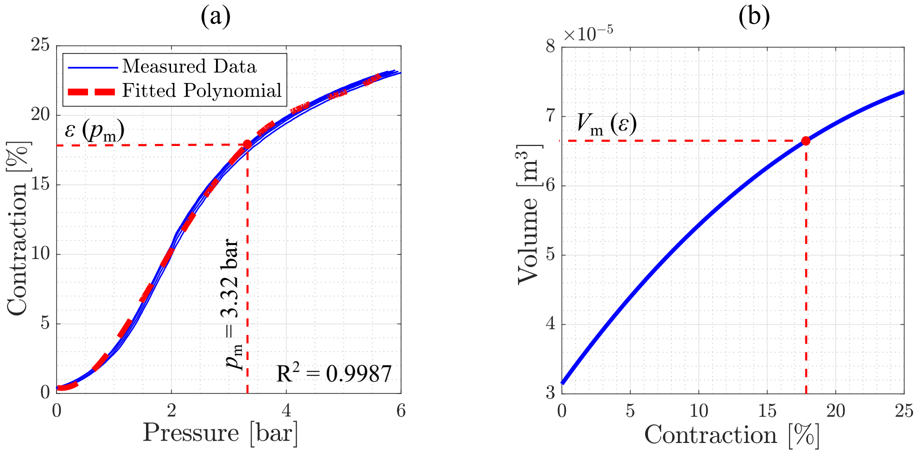

Figure 5.5: Model-identification of the PAM DMSP-20-100N-RM-RM. In (a) PAM contraction versus pressure. In (b) PAM volume versus contraction.

The measured data were fitted with a fourth-degree polynomial, formulated as

$$\varepsilon(p_\mathrm{m}) = c_1 p_\mathrm{m}^4 + c_2 p_\mathrm{m}^3 + c_3 p_\mathrm{m}^2 + c_4 p_\mathrm{m} + c_5\,, \tag{5.2}$$

where the coefficients are $c_1 = 0.1022, c_2 = -1.3370, c_3 = 5.1426, c_4 = -0.8131, c_5 = 0.4189$, with the coefficient of determination $\mathrm{R}^2 = 0.9987$. Using the identified relation $\varepsilon(p_\mathrm{m})$, the contraction ε and hence the length L_m of the PAM for each pressure p_m can be obtained as $L_\mathrm{m} = L_0 - \varepsilon$, where L_0 is the initial PAM length. This also allows the determination of the PAM volume, V_m, for each length L_m, which was previously unknown. The PAM volume can be calculated according to [157] as follows

$$V_\mathrm{m} = \frac{L_\mathrm{m} L_\mathrm{f}^2 - {L_\mathrm{m}}^3}{4\pi n_\mathrm{tu}^2}\,, \tag{5.3}$$

where n_{tu} is the number of thread turns, and L_{f} is the thread length calculated according to [47]. Now this relationship can be used to calculate the actuator parameters explained in the next subsection.

5.2.3 Actuator Pressure, Force, and Torque

The mathematical model of the actuator is given for one side exoskeleton leg and is further derived according to Fig. 5.6, where the transition from (a)→(b) implies standing up and reversely sitting down, meaning that in (a)→(b) the pressure is released from the PAM and shared with the pneumatic cylinder, while in (b)→(a) the pressure is returned to the PAM. The initial angle in (a) is $\theta = 107°$, as this is the angle at which the piston rod comes to the end of the cylinder, for contraction $\varepsilon(p_{\mathrm{m}} = 3.32\,\mathrm{bar})$, which is identified as a maximum pressure for the selected air pump BD-04A-20L. At the point where the angle θ starts decreasing, the air valve connecting the cylinder and the PAM is switched to position '1' as explained earlier. This results in two volumes merging, and the common volume is defined as:

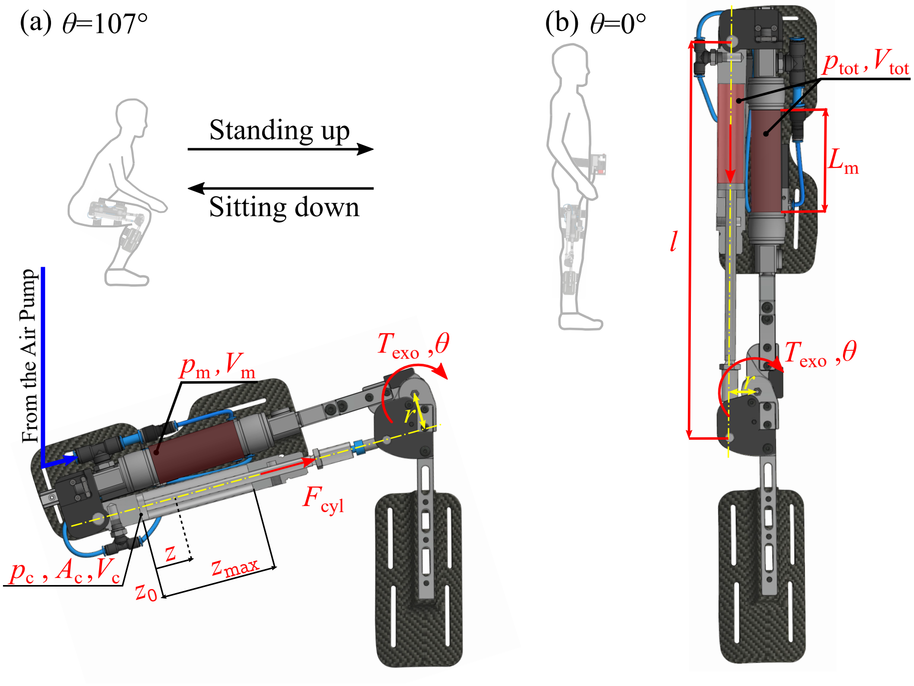

Figure 5.6: (a) Exoskeleton flexed at $\theta = 107°$, the angle where $z = z_0$ for $\varepsilon(p_{\mathrm{m}} = 3.32, \mathrm{bar})$ contraction. (b) Exoskeleton at $\theta = 0°$ for user standing.

$$V_{\mathrm{tot}} = V_{\mathrm{c}} + V_{\mathrm{m}}\,, \tag{5.4}$$

where V_{c} is the volume of the cylinder with the volume of the pneumatic tube added and is equal to

$$V_{\mathrm{c}} = A_{\mathrm{c}} z + A_{\mathrm{tc}} l_{\mathrm{tc}}\,, \quad z \in [z_0, z_{max}]\,, \tag{5.5}$$

where A_{tc} is the cross-sectional surface area of the pneumatic tube and l_{tc} is its length from the cylinder to the PAM. The current position of the piston z is expressed as

$$z = z_{\mathrm{max}} \frac{l - l_{\mathrm{min}}}{l_{\mathrm{max}} - l_{\mathrm{min}}}\,, \tag{5.6}$$

where l is the cylinder length (Fig. 5.6b), which was previously derived in our article [144], and l_{min} is the length when the piston touches the end of the cylinder ($z = z_0$). The maximum actuator length l_{max} is the length for $z = z_{\mathrm{max}}$.

The PAM volume was given in Eq. (5.3), but now the volume of the pneumatic tube ($A_{\mathrm{tm}} l_{\mathrm{tm}}$) is added for the actuator as follows

$$V_{\mathrm{m}} = \frac{L_{\mathrm{m}} L_{\mathrm{f}}^2 - {L_{\mathrm{m}}}^3}{4\pi n_{\mathrm{tu}}^2} + A_{\mathrm{tm}} l_{\mathrm{tm}} \,. \tag{5.7}$$

Once the total volume is known, and isothermal expansion is assumed, the air pressure p_{tot} expanding from the initial pressure $p_{\mathrm{tot}}^{\mathrm{init}}$ and the initial volume $V_{\mathrm{tot}}^{\mathrm{init}}$ to the current volume V_{tot} can be computed as

$$p_{\mathrm{tot}} = p_{\mathrm{tot}}^{\mathrm{init}} \frac{V_{\mathrm{tot}}^{\mathrm{init}}}{V_{\mathrm{tot}}} \,, \tag{5.8}$$

As volume V_{tot} gradually increases, pressure p_{tot} decreases, which means that as the angle θ approaches 0° (knee fully extended), L_{m} also decreases, consequently affecting the cylinder length l, the current position of the piston z, and finally the volume of the cylinder V_{c}. Therefore, the PAM length must be updated for each new pressure during the transition according to the model identified in Eq. (5.2).

Once the current pressure is known during the transition, the cylinder force F_{cyl} can be expressed as the pressure p_{tot} acting on the piston surface area A_{c}, as follows

$$F_{\mathrm{cyl}} = p_{\mathrm{tot}} A_{\mathrm{c}} \,. \tag{5.9}$$

Finally, with the known cylinder force F_{cyl}, the exoskeleton torque T_{exo} can be computed as follows

$$T_{\mathrm{exo}} = F_{\mathrm{cyl}} r \,, \tag{5.10}$$

where the lever arm r (see Fig. 5.6) was mathematically modeled in the previous chapter (Eq. (4.15)). The computed values of different physical parameters for the joint rotation from $\theta = 107°$ to $\theta = 0°$ are shown in Fig. 5.7. In the case when the angle theta is changed from $\theta = 0°$ to $\theta = 107°$ (sitting down), the process is reversed if the "Torque" state is still active. Therefore, by rotating the joint back to $\theta = 107°$ the air is returned into the PAM

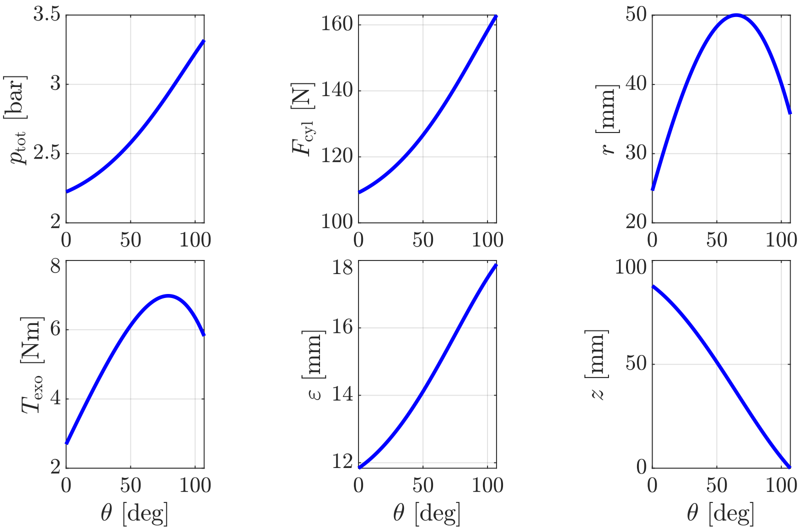

Figure 5.7: Theoretical profiles of different physical parameters for the joint rotation from $\theta = 107°$ to $\theta = 0°$.

while generating the same torque. However, when the "Quasi-passive" state is activated (see Fig. 5.3) at the angle of $\theta = 0°$ and the joint is rotated back to $\theta = 107°$, the air is compressed only in the cylinder's volume, thus the pressure and torque reach higher values than in the active mode. Still, the air can be returned back into the PAM by setting valve 2 in position '1' once the air has been compressed in the cylinder (person sitting). The mathematical model in this paper doesn't account for PAM stretching that occurs beyond $\theta = 107°$, even though rotation can reach $\theta = 135°$. Experimental results will assess the exoskeleton's overall dynamics.

5.3 Concept of Energy Recovery in Sit-Stand

Figure 5.8 depicts the concept of energy recovery in sit-stand tasks. In the transition from standing to sitting, the knee angle changes in the opposite direction of the biological knee torque, resulting in negative knee power and indicating power absorption [87]. Here, the exoskeleton is set to operate in quasi-passive mode, behaving similarly to a passive air spring. The compressed air in the pneumatic cylinder produces torque in the same direction as the biological muscles and assists the user while absorbing some of the biological knee power in the form of compressed air.

Once the user is sitting the part of regenerated compressed air is stored in the pneumatic artificial muscle and the exoskeleton is set in transparent mode to allow unobstructed sitting. The air pump adds additional compressed air, which can be adjusted to the desired pressure depending on the required assistance.

Standing up requires positive biological knee power since the knee angle changes in the

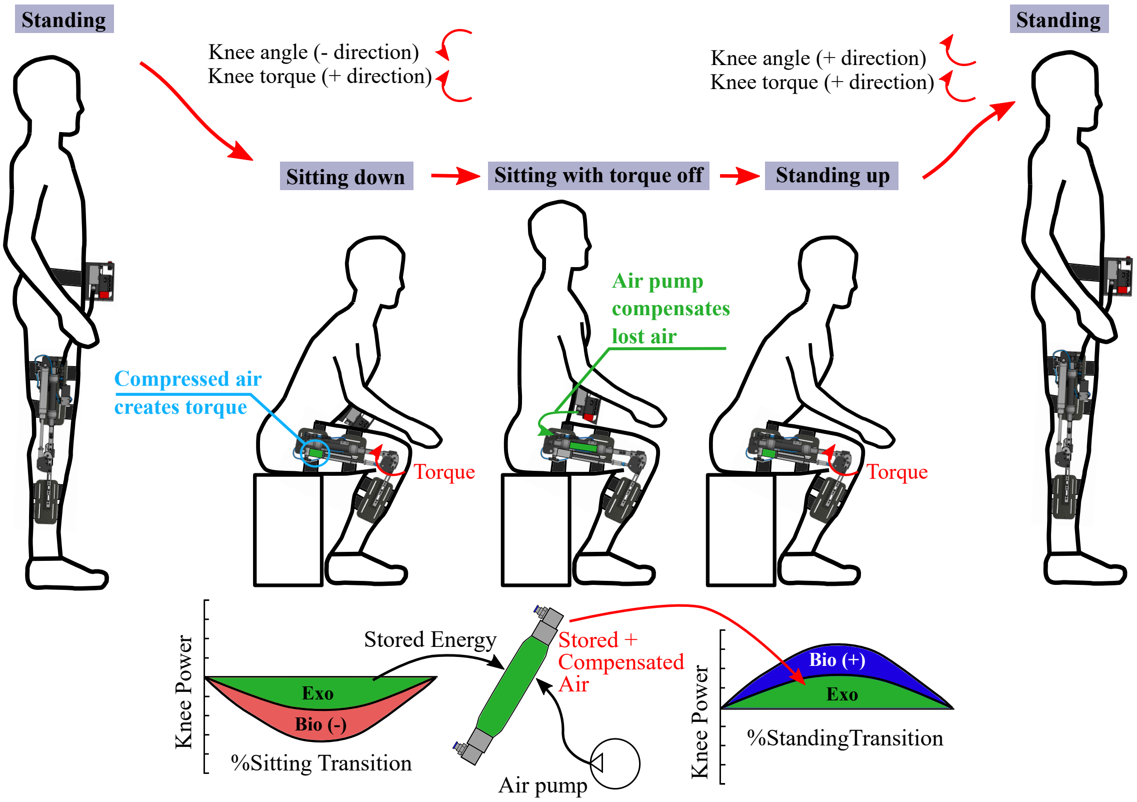

Figure 5.8: Concept of energy recovery in the sit-stand task. The power profile shape and amount are only illustrative.

same direction as the biological knee torque. Compressed air stored from before, plus the added air from the air pump, is now released from the pneumatic artificial muscle to the pneumatic cylinder to actively assist the user and reduce the portion of total biological knee power produced by muscles. Finally, the user stands up and the cycle is complete.

5.4 Human Subject Experimentation

This section presents a pilot study with an able-bodied subject (27 years old, 90 kg, 1.93 m tall), aiming to validate JSI-KneExo's key contributions. The exoskeleton was controlled in Simulink Real-Time™, while the pressure, angle, and force data were collected and analyzed offline in Matlab. The experimental setup is in Fig. 5.9. To determine exoskeleton impact on the subject, a multi-channel Trigno wireless EMG system (Delsys, USA) recorded Vastus Medialis (V. Med.) and Gluteus Maximum (Glut. M.) muscle activity at 2148.15 Hz, following SENIAM guidelines [167]. Prior to experiments, muscle maximum voluntary contractions (MVC) were recorded. Optitrack's 16 cameras (NaturalPoint, USA) at 120 Hz captured joint kinematics. Using 37 markers as per Motive Optical motion capture software, the human skeleton was reconstructed. Visual feedback on a screen ensured subject positioning consistency for repeatable experiments.

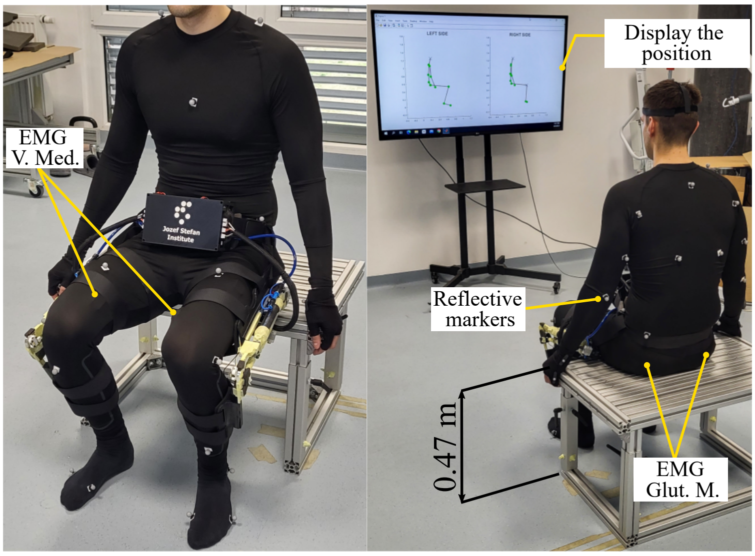

Figure 5.9: Experimental setup: EMG electrodes, reflective markers, and screen for visual feedback.

5.4.1 Experiment

The subject was instructed to perform ten sit-to-stand and stand-to-sit transitions under unassisted (transparent) and assisted conditions. The experiment aims to validate the energy recovery (compressed air return to PAM) while relieving the leg muscles, and to evaluate the exoskeleton operation, highlighting the transparency achieved after every sit-down while storing recovered air. When standing up, the exoskeleton assisted the subject in active mode, and when sitting down, the exoskeleton assisted the subject in quasi-passive mode. In the unassisted trial, the state was set to "Release All" to enable entire transparency.

Strategy and Control:

The controller for the assisted condition involves a state machine with states triggered based on threshold values from a pressure sensor and two encoders, with knee angular velocity derived through knee angle numerical differentiation. Exoskeleton torque was computed offline by multiplying the cylinder force with the lever arm length, calculated from the knee angle and mathematical model. In Fig. 5.10, the average exoskeleton torque (right leg) and its standard deviation across ten repetitions are presented in relation to the transition, with 100% denoting sitting and 0% indicating standing. Figure 5.11 shows the pressure change in both PAMs simultaneously, since the pressure sensor is connected to both PAMs (see Fig. 5.3). The intervals when the pump was switched on and off are indicated, as well as the amount of recovered air. In both figures, the exoskeleton states

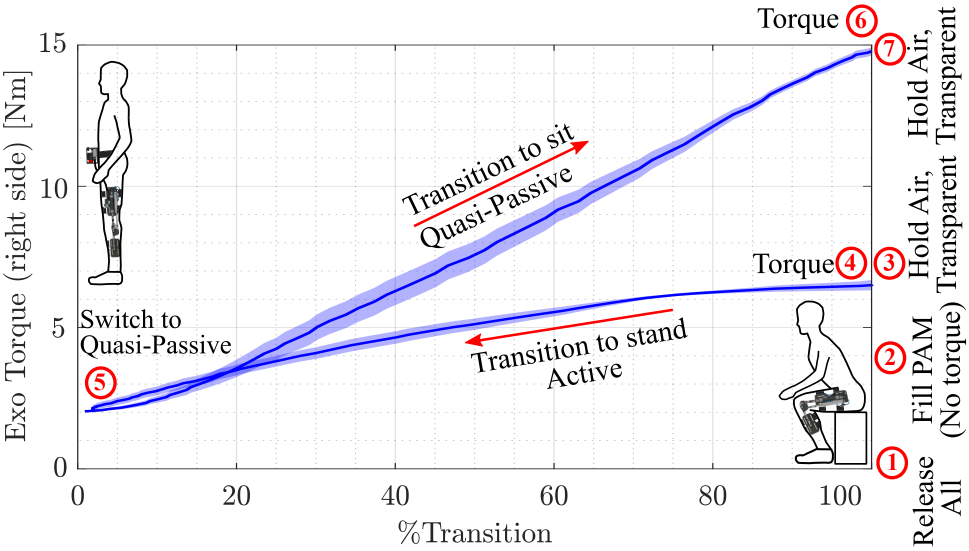

Figure 5.10: Right leg exoskeleton torque during transition, scaled from 100% (sitting) to 0% (standing), with numbered circles indicating different states.

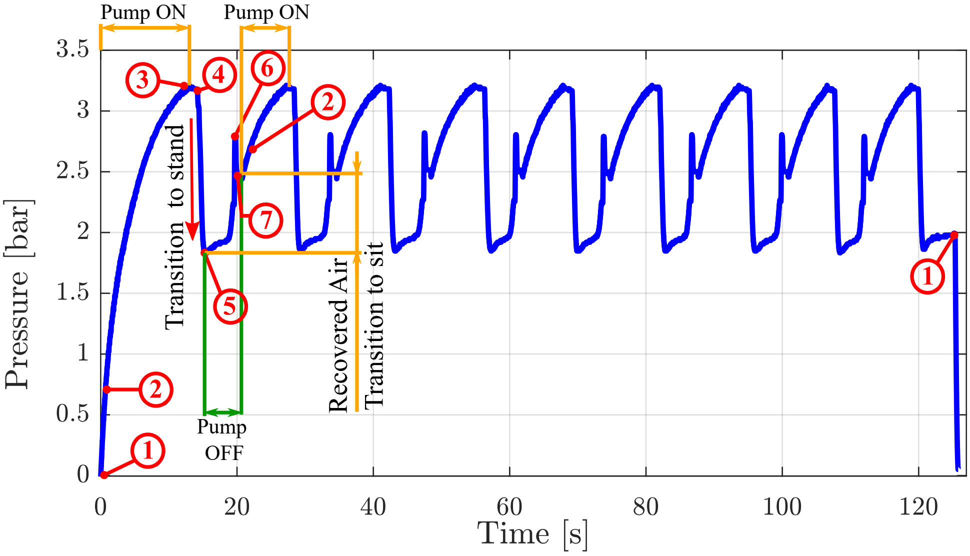

Figure 5.11: Pressure sensor measurements over time with state distinctions using numbers. Pump on-off intervals and air recovery periods are marked.

are indicated by numbers. The experiment is divided into seven parts as follows.

Initial Sitting: The experiment started by equalizing the actuator to atmospheric pressure in ①. The air pump gradually filled the PAM to a set pressure of 3.2 bar in ②. In ③ the air pump was switched off as the PAM was charged with compressed air but had not yet been released into the cylinder and therefore the exoskeleton was still transparent.

Standing Up: In ④, the sensors detected the subject's standing up movement, thus the actuator released the compressed air into the pneumatic cylinder, providing an active torque of ∼6.7 Nm which gradually decreased as the pressure dropped until ⑤ (fully standing), at which point the pressure was equal to ∼1.85 bar and the torque ∼2 Nm.

Sitting Down: Upon sensor detection of the standing position, the mode was changed to "Quasi-passive". Thus, from ⑤ to ⑥, when the subject transitioned to sitting, the air was compressed exclusively in the pneumatic cylinder, reaching a maximum torque of ∼14.88 Nm.

Air Return: By detecting the subjects' full seating in ⑥, and by positioning valve 2 to '1', compressed air from the cylinder had flown back to the PAM, restoring the PAM pressure from ∼1.85 bar to ∼2.5 bar, as the subject went from standing to sitting while the air pump was off.

Transparent Sitting: In ⑦, "Hold Air, Transparent" state holds the remaining air in the PAM but releases the compressed air from the cylinder allowing unobstructed sitting.

Next Repetition: In the next repetition, the air pump only had to compensate for air loss, as the joint hadn't fully rotated to its end position. Thus, the air pump has been restarted (state ②), which allowed compensation for the pressure difference in the PAM up to 3.2 bar.

End: Finally, all the compressed air from the actuator was released in ① and the experiment was completed.

5.5 Discussion

This section discusses the energy recovery of the exoskeleton with the simultaneous muscle activity reduction in sitting transfers. Fig. 5.12 displays average muscle activity over ten repetitions for transitions between sitting and standing, comparing unassisted (ExoOff) and assisted (ExoOn) conditions. The mean envelope of the raw EMG signals was extracted to analyze muscle effort, involving a series of filtering steps: 4^{th} order bandpass Butterworth (20-400 Hz), rectification, and low pass filtering (5 Hz, 4^{th} order Butterworth). EMG amplitude was normalized to the subject's MVC, segmented, and averaged based on %Sitting and %Standing identified from the knee angle. **EMG reduction with simultaneous energy recovery:** Interestingly, returning compressed air to the exoskeleton reservoir not only saved energy and pumping time but also reduced muscular effort. Notably, V. Med. activity decreased by ∼31% (mean effort) when sitting down with assistance compared to unassisted. Glut. M. showed no major changes between the conditions, with low activity normalized to MVC. During standing up, a mean effort was reduced by ∼13% in V. Med. when the exoskeleton assisted.

Actuation frequency relies on the air pump and the desired pressure, set at 3.2 bar during experimentation. To assess energy recovery usefulness, three states with specific pressures are highlighted: state ③ at 3.2 bar, state ⑤ at 1.85 ± 0.01 bar, and state ⑦ at 2.46 ± 0.01 bar. With energy recovery, the air pump has to refill only from 2.46 ± 0.01 up to 3.2 bar. Without energy recovery, the air pump has to refill from the residual PAM pressure after actuation, 1.85 ± 0.01, up to 3.2 bar. The time to restore pressure to the desired level is determined using Eq. (5.1), derived earlier from air pump characterization. The results are listed in Table 5.1.

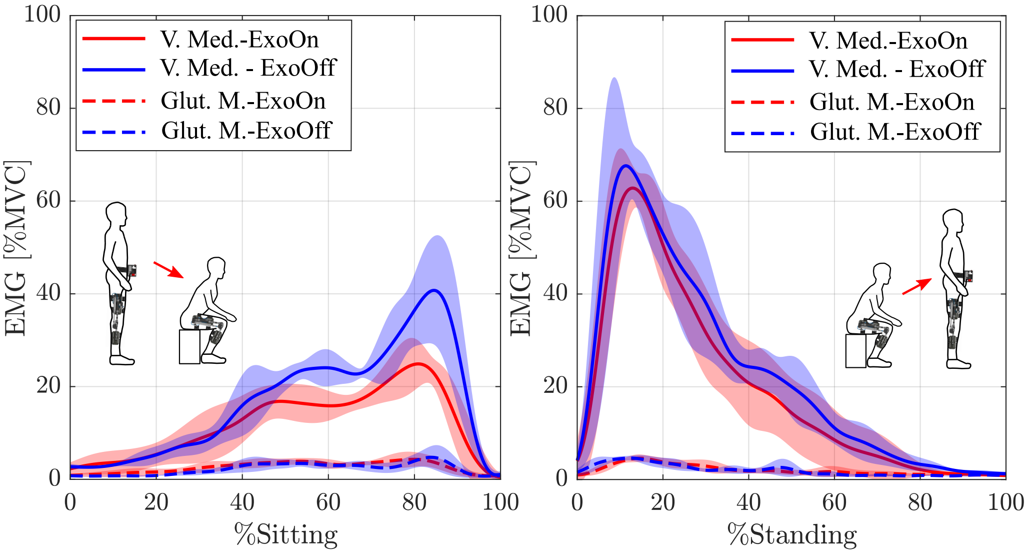

Figure 5.12: EMG recordings of the vastus medialis and gluteus maximus during sitting and standing transfers under assisted and unassisted conditions.

Table 5.1: Maximum Actuation Frequency with and without Energy Recovery

	Air pump: BD-04A-20L	Air pump: BD-07A-35L
Max. Freq. w/ ER[1]	8.32 ± 0.04 min^{-1}	71.53 ± 0.66 min^{-1}
Max. Freq. w/o ER[2]	6.55 ± 0.02 min^{-1}	43.31 ± 0.34 min^{-1}

[1] Time to restore pressure with BD-04A-20L: 3.61 ± 0.02 s (1 leg), 7.21 ± 0.03s (both legs). With BD-07A-35L: 0.42 ± 0 s (1 leg), 0.84 ± 0.01 s (both)

[2] Time to restore pressure with BD-04A-20L: 4.58 ± 0.02 s (1 leg), 9.16 ± 0.03s (both legs). With BD-07A-35L: 0.71 ± 0.01 s (1 leg), 1.42 ± 0.01 s (both)

Yet, this frequency is derived from the air pump's ability. In experiments, the frequency, of course, is also influenced by the user's pace and transfer intervals. When pumping intervals are translated into energy savings through recovery, the exoskeleton's battery endurance extends by 1.27 ± 0.01, ∼27% (small pump), or 1.69 ± 0.02, ∼69% (large pump).

5.6 Chapter Conclusion

In conclusion, the key innovation of the JSI-KneExo is simultaneous human assistance with efficient energy recovery, leading to approximately ∼27% energy savings as the pump only needs to recompensate part of the compressed air. This is enabled by a novel pneumatic circuit design that provides different operation modes, and portable pneumatic actuation using PAM as an air tank. However, this chapter presents only initial results from a single subject and lacks statistical evidence. The next chapter evaluates the exoskeleton for walking.

Chapter 6

Hybrid Rigid-Soft Exoskeleton for Multi-joint Lower Limb Assistance

One of the primary objectives in the domain of exoskeleton research has been to assist the locomotion of either healthy or impaired users by providing external power to the biological muscles through the actuators integrated into rigid exoskeletons or soft exosuits [1]. The difference between the two lies in their design. Rigid exoskeletons employ load-bearing frames, with actuators often aligned with human joints to deliver torque directly at the joints. While rigid exoskeletons provide increased stability and vital support for weight-bearing joints in the lower limbs, their mechanical complexity and bulkiness rise with the higher dimensionality of the joint's active degrees of freedom (DoF), further resulting in misalignment issues and negatively impacting user comfort [168]. Oppositely, soft exosuits do not provide body support as they do not have rigid frames. Instead, they contain textile parts worn on human limbs, with connected tendons actuated by proximally located actuators. The elimination of rigid parts minimizes bulkiness, mechanical complexity, and movement restrictions. This is particularly beneficial for human joints with higher DoF, leading to enhanced comfort and adaptability to the human body [69].

The existing literature covers locomotion augmentation with both rigid exoskeletons [12], [37], [88], [89], [169]–[171] or soft exosuits [11], [20], [158], [172]–[175] in both healthy and impaired individuals. However, it sparks interest in whether an assistive robotic device can combine the advantages of both rigid and soft designs, an area that has received limited exploration. An example can be found in the work by Cao et al. [21], where an exosuit delivers active assistance and is paired with a passive rigid exoskeleton aiding in extra weight carrying. Another study, focusing on single-joint assistance through a rigid-soft system, employs a strategically positioned linear actuator to assist the knee, specifically designed to overcome potential joint misalignment [176]. In [177] a combination of pneumatic and electromechanical actuation was investigated, but the exoskeleton is fully rigid. Therefore, in the current literature, there is no evidence of an exoskeleton integrating soft exosuits and rigid exoskeletons to actively assist multiple lower limb joints. Such a configuration could improve adaptability by utilizing soft exosuits on higher DoF joints such as the hip, overcoming mechanical complexity and movement restrictions. Simultaneously rigid exoskeletons could offer structural stability and body support during the stance on single active DoF joints like the knee, where designing passive joints or mechanisms is not crucial for allowing movement in other directions, though it can sometimes be done for better aligning the non-constant moving axis of the knee [178].

Building upon this premise, the present study introduces a novelty by integrating a soft, tendon-driven hip exosuit with a pneumatic rigid knee exoskeleton in a hybrid assistive device where each joint is assisted independently. The section also investigates its effect on metabolic cost, muscular activation, and kinematic patterns when walking uphill at 15° incline and a speed of 3 km/h. The inclined setup was chosen to increase positive biological power demands of both hip and knee joints, therefore, assisting these joints when they experience higher loads is expected to enhance energy efficiency and thus yield strong human augmentation benefits, as outlined in the theoretical analysis and guidelines for exoskeleton developers by Nuckols et al. [54] and other recent experimental studies involving inclined walking with the hip or knee exoskeletons [12], [88], [171], [173]. During inclined walking, the peak positive biological power phases occur during hip flexion in swing and knee extension in stance [179]. Accordingly, the hip exosuit contributes to hip flexion during the swing phase through a simplified mechanical design using a tendon-driven actuation, while the rigid knee exoskeleton aids in knee extension during stance through load-bearing frames, thereby injecting energy at the joints during the positive biological power phases of the gait. Given that the knee joint bears the load response during this critical phase, it has to exhibit compliance [87]. Therefore, an inherently compliant fast-acting pneumatic actuator might be beneficial during the load response phase to alleviate stress on the knee. Both devices of the integrated system have previously undergone partial individual testing. The hip exosuit demonstrated a significant reduction in hip flexor muscle effort during level ground walking, as reported by Tricomi et al. [180]. Similarly, the knee exoskeleton has been used in sit-stand tasks, as highlighted in the previous chapter.

In the context of metabolic expenditure, existing literature suggests that the energetic expenditure of walking includes supporting body weight (∼28%), generating propulsion (∼48%), swinging the legs (∼10%), and stabilizing laterally (∼6%) [181]. Given the knee exoskeleton's role in partially assisting body support and propulsion and the hip exosuit's role in partially assisting in swinging the legs, it is anticipated that multijoint assistance will yield greater metabolic benefits compared to both unassisted and single-joint assisted scenarios. Additionally, it is expected that assisted muscles will reduce muscular activity without significantly altering kinematics.

The remainder of this chapter is structured as follows: Section 6.1 introduces the hybrid assistive device. Section 6.2 outlines the experiments. Section 6.3 presents the results. Section 6.4 provides a discussion, and the chapter concludes in Section 6.5.

The work of this chapter is published in IEEE Transactions on Medical Robotics and Bionics [146].

6.1 Hybrid Concept

This section provides an overview of the hybrid exoskeletal system (Fig. 6.1a) comprising a soft, tendon-driven hip exosuit (Fig. 6.1b) and a rigid, pneumatic knee exoskeleton (Fig. 6.1c).

6.1.1 Tendon-Driven Hip Exosuit

6.1.1.1 Design

The soft hip exosuit has an underactuated design, meaning it assists the hip flexion of both legs with a single actuator (Fig. 6.1b). It comprises a waist belt carrying the T-Motor AK80-6 actuator, Arduino Mega 2560 control board, and power supply. The actuator, equipped with a double-layer pulley, employs two artificial tendons wound in opposite directions. As the actuator rotates in one direction, it pulls one tendon and brings the proximal anchor point closer to the distal anchor point, causing a flexion moment in the hip joint of one leg. Meanwhile, the other tendon is released, so only one leg is assisted while the other moves freely. When the tendon is loose, it causes zero impedance since the

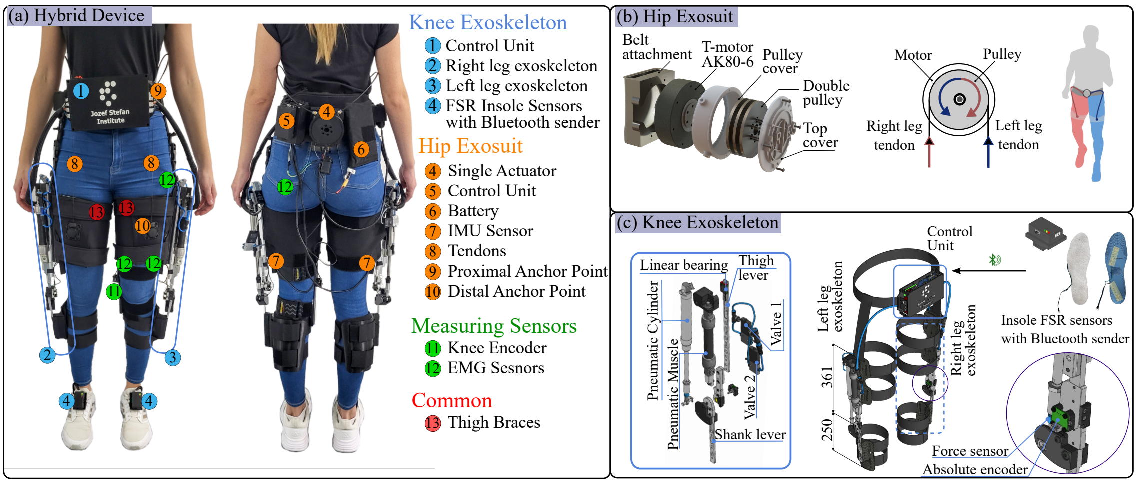

Figure 6.1: (a) Overview of the hybrid exoskeleton with labeled parts. In (b) hip exosuit features a tendon-driven actuation with a double-layered pulley, where each layer contains a tendon so that one direction of motor rotation assists one leg and vice versa assists the other leg. In (c) knee exoskeleton comprises three main parts: the control unit, the left leg, and the right leg exoskeleton. The actuator includes a pneumatic cylinder, pneumatic muscle and two air solenoid valves. Compressed air is supplied from the air compressor. Insoles with FSR sensors inside shoes wirelessly transmit signals to the control unit.

human limb is not connected to the actuator. Thigh braces, made from double-layer soft fabric reinforced with rubber, are a shared component between the exosuit and exoskeleton.

6.1.1.2 Control

The control algorithm is depicted in Fig. 6.2. The algorithm is based on the hip joint kinematics obtained from the IMUs mounted laterally on the thigh (Fig. 6.1a). They provide an approximation of the hip flexion angle. The High-Level Controller estimates in real-time the gait phase via an adaptive oscillator approach [182]–[184] using the hip inter-limb angle $\theta_{\mathrm{IL}(t)}$. The Gait Phase Estimator comprises three modules: the adaptive oscillator's dynamical system, the gait event detector, and the phase error correction. The three of them are meant to estimate a continuously increasing gait phase variable and to normalize it in a range between $[0\ 2\pi]$ after alignment with the beginning of each gait cycle. A motor reference position trajectory is built upon the gait phase estimated through cubing spline interpolation. In the Low-Level controller, a PID controller transforms the position error into a motor velocity command. Assistance is provided to each leg exclusively during the swing phase, with no assistive forces during stance.

6.1.2 Pneumatic Rigid Knee Exoskeleton

The subsection provides a concise overview of the knee exoskeleton, illustrated in Figure 6.1c. For a detailed mechatronic description of the knee exoskeleton refer to Miskovic et al. [145]. In the referenced study, the pneumatic muscle stores accumulated air from negative work motion. In this study, the pneumatic muscle serves a minimal function, acting solely as an auxiliary component for pre-storing compressed air.

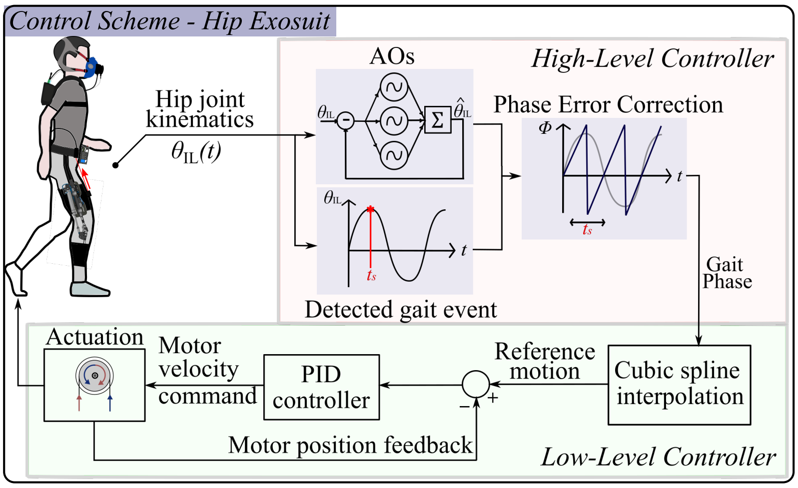

Figure 6.2: The hip exosuit control involves a high-level controller and a low-level controller. The adaptive oscillator layer in high-level uses the inter-limb hip flexion angle to derive a motor reference position trajectory and identify the gait phase. In the low-level, a PID controller transforms the position error into a motor velocity command.

6.1.2.1 Design

The knee exoskeleton aids knee extension by applying torque directly to the knee joint during the stance phase. The torque is controlled by adjusting the air pressure in the compressor. The pneumatic cylinder with a 25 mm bore diameter, generates force when supplied with compressed air, and with the mechanical advantage provided by the lever arm length (70 mm), torque is produced between the thigh and shank levers, with a hard stop preventing hyperextension. The torque-generating and transparent intervals are switched by two monostable air solenoid valves. The system uses an Arduino Mega 2560 and custom-made PCBs with MOSFETs for controlling valves. Switching valve 1 releases the compressed air, and valve 2 allows the compressed air to enter the cylinder.

6.1.2.2 Control

The exoskeleton's controller (Fig. 6.3) functions as a Deterministic Finite State Machine (DFSM). State transitions are governed by input signals from FSR sensors in the insoles (HS - Heel Sensor, FS - Finger Sensor), together with feedback from the exoskeleton's encoder signal (θ_K). The thresholds for the FSRs are individualized heuristically. Upon reaching the predefined heel sensor threshold T_1, the assisting torque activates. The torque deactivates (through air release) upon detection of the opposite leg's knee swing, identified by the zero crossing of velocity, specifically set to detect the falling direction ($\dot{\theta}_{KO} = 0$), along with the condition that the opposite foot is in the air, detected by FSR sensors as $HS_o < T_3$, $FS_o < T_4$, where thresholds are individualized heuristically. The subscript "o" denotes the opposite leg. To prevent false torque activation, state transitions involving torque activation or deactivation are conditioned by the knee encoder threshold angle, T_2. This ensures torque activation only within the appropriate knee angle range, corresponding to typical values from the literature. Additionally, to prevent hyperextension, a threshold T_5 is implemented at $0°$, prompting the actuator to immediately release air when the angle reaches this value. If any state remains inactive beyond the designated "timeout" threshold, the system automatically transitions to the "Stand still" state.

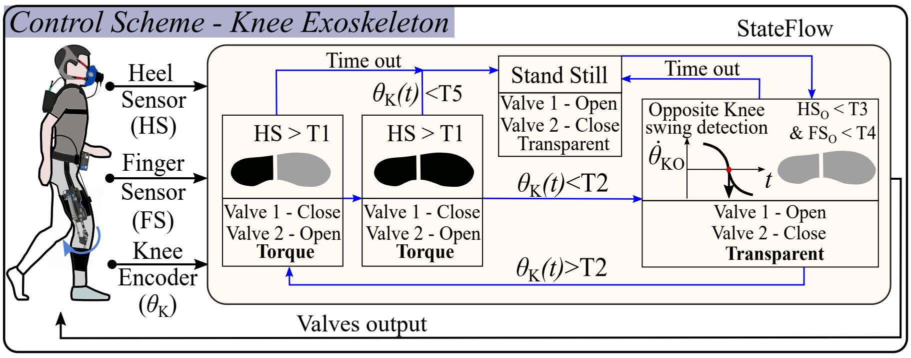

Figure 6.3: The knee controller operates as a Deterministic Finite State Machine (DFSM): The thresholds are individualized for users. Valve1 - clutch valve, Valve2 - torque enabling valve, T - Thresholds, HS - Heel sensor, FS - Finger sensor, θ_K - Knee encoder. The subscript "o" denotes the opposite leg.

6.1.3 Technical Metrics and Hybrid Gait Assistance

Figure 6.4 shows an example of torque provided by the right leg knee exoskeleton and the hip motor torque assisting both legs across the gait cycle. Negative motor torque values for the hip graph indicate support during left hip flexion, whereas positive torque values signify assistance during right hip flexion, complying with the underactuated nature of the device. For instance, with reference to the right leg, exosuit assistance is provided from 60% to 100% of the gait cycle, while the knee exoskeleton assists the right leg in the initial ~30% of the gait cycle. Table 6.1 details the relevant parameters of the hybrid exoskeleton.

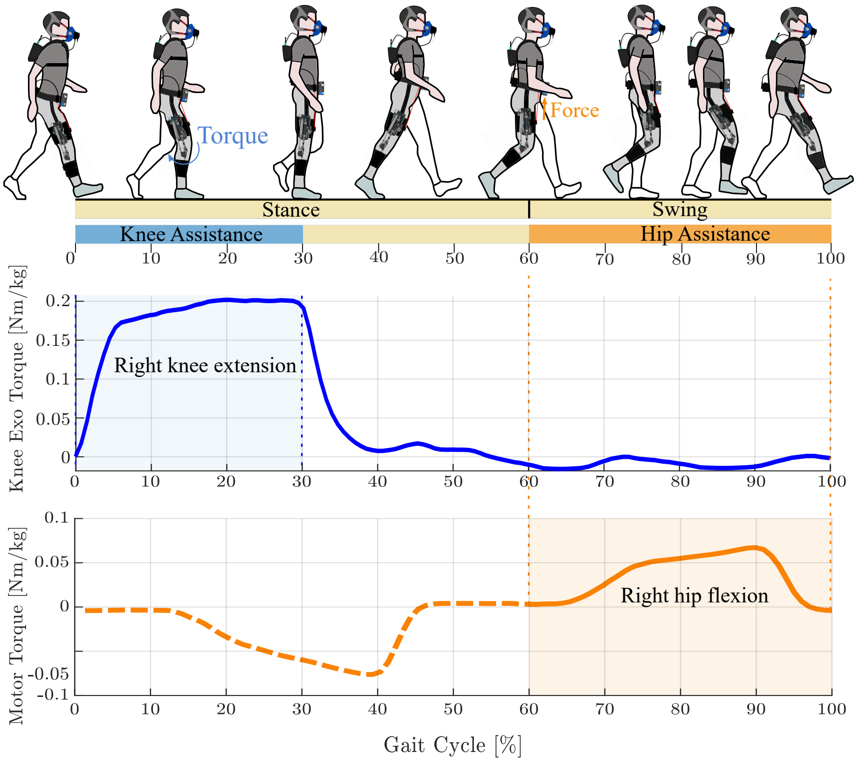

Figure 6.4: An example of knee and hip assistance profiles with the gait cycle.

Table 6.1: Parameters of the Hybrid Exoskeleton

PARAMETER	VALUE	UNIT
Total weight[1]	5.6	kg
Knee Exo Weight[2]	3.4	kg
Knee Exo RoM	0-90	°
Upper Knee Link Dimensions	361x91x39	mm
Lower Knee Link Dimensions	250x108x43	mm
Max. Knee Torque[3]	20.6	Nm
Hip Exo Weight	2.2	kg
Max. Hip Motor Torque[4]	12	Nm

[1] The total weight of the device carried on the person. The air is supplied externally and is not contained in the device.

[2] Weight breakdown: Control Unit (0.9 kg), Unilateral Exoskeleton Mass (1.25 kg).

[3] Obtained at max. pressure of 6 bar.

[4] Max. tendon force ∼480 N (with pulley diameter 50 mm).

The entire system weighs 5.6 kg, with 3.4 kg attributed to the rigid knee exoskeleton, and the remainder to the hip exosuit. A detailed kinematic analysis of the knee mechanism is reported in our previous work [144]. The knee exoskeleton can generate a maximum torque of 20.6 Nm at a pressure of 6 bar. This corresponds to ∼27% of the maximum biological knee torque for an individual weighing 75 kg, in the sagittal plane during load response while walking on a 15° slope at 1.34 m/s [185]. The range of motion 0°- 90° covers the full range of motion of the human knee joint during walking. The hip actuator can produce a maximum torque of 12 Nm corresponding to a tendon force of 480 N with a pulley diameter of 50 mm. This corresponds to ∼35% of the maximum biological hip torque estimated using the same reference as for the knee.

6.2 Experimental Evaluation with Human Subjects

6.2.1 Experimental Setup

The hybrid exoskeleton was assessed in an experimental setup (Fig. 6.5) involving inclined walking at 15° and a speed of 3 km/h on a TechnoGym Run Live 500 treadmill (Cesena, Italy). Muscle activity was analyzed using a Trigno wireless multi-channel surface EMG system (Delsys, Natick MA, USA) on four left leg muscles: Vastus Medialis, Vastus Lateralis, Tensor Fasciae Latae, and Gluteus Maximus. Electrode placement followed SENIAM guidelines [167]. Thigh braces limited EMG placement on hamstrings and Rectus Femoris due to increased skin-brace pressure during exoskeleton force transfer. EMG signals, sampled at 1 kHz, were acquired using a Quanser QPIDe DAQ board (Markham, Ontario, Canada). Oxygen and carbon dioxide consumption data were gathered using a portable gas analyzer (K5, COSMED, Rome, Italy) to evaluate metabolic energy expenditure. Hip kinematics was recorded with IMU sensors (Bosch, BNO055, Gerlingen, Germany) mounted laterally on the thigh harnesses, while knee kinematics was recorded with an absolute encoder AS5600 (ams AG, Premstätten, Austria), mounted on the inside of the left knee. The MATLAB/Simulink Real-Time was used to acquire data from the knee, hip, and EMGs, while K5 COSMED data was sent through Bluetooth to the COSMED Omnia proprietary software.

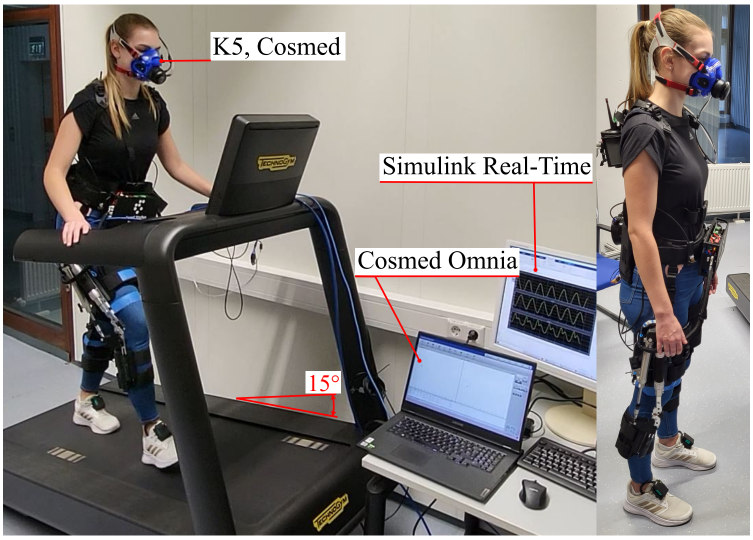

Figure 6.5: Experimental setup during inclined walking at 15° and 3 km/h speed.

6.2.2 Experimental Protocol

The goal of the experiment is to validate the hypothesis that hybrid assistance yields greater benefits to the user compared to single-joint assistance. A group of seven individuals was recruited, that met the criterion of a height exceeding 175 cm, to align with the exoskeleton's designed proportions. The participant group comprised one female and six males, with an average age of 27.57±2.37 years (mean ± SD), body weight of 75±6.95 kg, and height of 183.29±4.95 cm. All participants had no prior history of musculoskeletal or neurological conditions. Prior to commencing the experimental procedures, each participant provided explicit consent by signing informed documents. The research protocols adhered to the principles outlined in the Declaration of Helsinki and received approval from the Ethical Committee of Heidelberg University (approval code: S-313/2020). The procedure for human testing is depicted in Figure 6.6. It comprised two sessions dedicated to familiarization and measurement, respectively. The second session was scheduled a day after the initial one, allowing participants adequate time for rest. The conditions tested included: unassisted, hip-assisted, knee-assisted, and hybrid-assisted. During both visits, the sequence of conditions was randomized to mitigate any potential bias. During the familiarization session, subjects were introduced to the experimental setup, and the hybrid device was donned following its instructions for use. Next, they walked for 5 minutes in each condition or until they felt comfortable with the device. They were given a 10-minute break between each trial. In the measurement session, EMG sensors were placed on shaved and cleaned skin. After donning the hybrid device, the COSMED device was calibrated, and participants were instructed to breathe normally for 4 minutes in a standing resting state at the start and between trials. A 15-minute break was given between each trial.

At the end of the experiment, participants were asked to report subjectively about their perception of the provided assistance. Specifically, they were asked to grade using a scale from 1 to 10 (i.e., 1 = strong disagreement and 10 = strong agreement) whether the specific assisted condition helped them reduce their walking effort compared to an unassisted scenario.

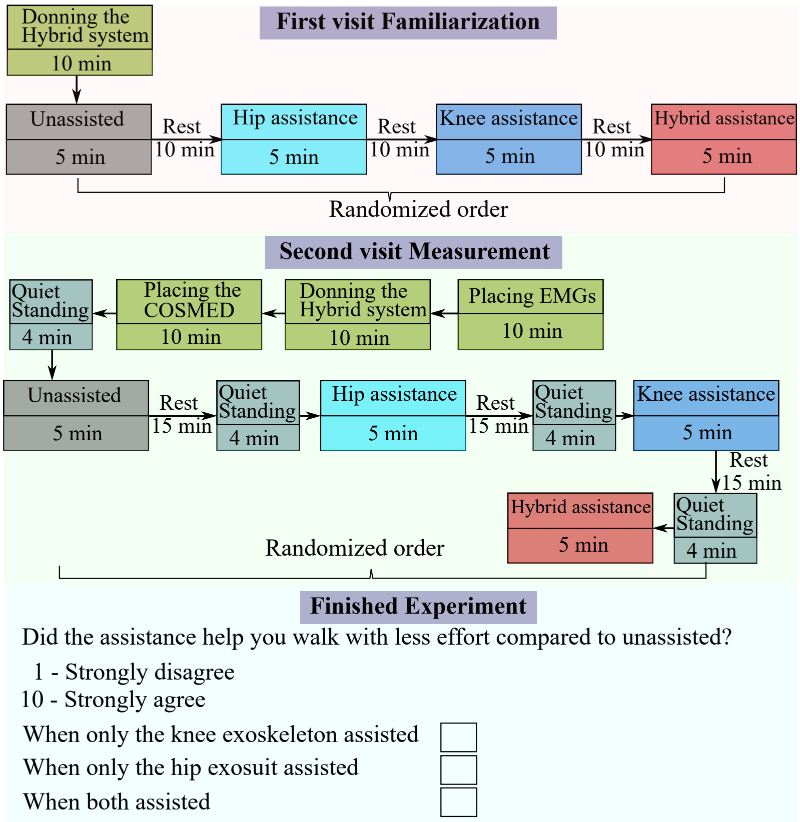

Figure 6.6: The protocol consisted of two visits: the familiarization and measurement visit. The second visit was arranged one day following the first. Randomization of conditions was applied during both visits. Upon completing the experiment, the participants were asked the questions shown in the figure.

6.2.3 Data and Statistical Analysis

6.2.3.1 Muscular Activity

To examine the impact on muscular activity, the change in muscle activation was evaluated across the four distinct conditions. The raw EMG signals were band-pass filtered (20-400 Hz, 4th order Butterworth), full-wave rectified, and low-pass filtered (6 Hz, 4th order Butterworth) to extract the EMG envelope. Normalization was performed with respect to the peak activation observed in the unassisted condition, and signals were segmented based on kinematic data. EMG data from the final 3 minutes of each trial was analyzed to capture a phase of intensified muscle effort compared to the initial stage. Muscle activation was quantified using the Root Mean Square (RMS) at each step. The RMS values for each subject were then averaged across steps.

6.2.3.2 Metabolic Cost

The gross metabolic cost of walking for all four conditions was estimated using Péronnet and Massicotte's equation [186], then subtracted by the average cost at quiet standing to isolate the costs associated with walking. The metabolic energy expenditure of the last three minutes of walking for each condition was analyzed, as data in the first two minutes were not yet at a steady state [187]. Data were normalized concerning subjects' weight for comparison among participants.

6.2.3.3 Kinematics

The kinematic assessment involved the examination of angle profiles of the hip and knee, along with angular velocity profiles, all for the left leg while assuming symmetry in the right. Raw data were segmented into steps and low-pass filtered (4th order Butterworth, cut-off frequency 10 Hz). The range of motion (RoM) was determined for each subject and the peak positive and negative velocity across all steps in all four conditions. The kinematic data of the last three minutes of walking for each condition was analyzed.

6.2.3.4 Hip Motor and Knee Exoskeleton Torque

Hip motor torque profiles on both legs were assessed, considering the coupled actuation. The raw motor torque data underwent a 4th-order Butterworth low-pass filtering (cutoff frequency 10 Hz), normalization based on subjects' weight, and segmentation using kinematic data. Assistive knee torque from the exoskeleton was derived through cylinder force measurements and lever arm length from the actuator's kinematic model. The identical filtering, normalization, and segmentation processes were applied as for the hip motor torque.

6.2.4 Statistical Analysis

The normality of data distributions was assessed using a Shapiro-Wilk test with a significance level of $\alpha = 0.05$, indicating that the data adhered to a normal distribution. To identify statistically significant differences in muscle activity, metabolic cost, kinematics, and user preference across the various tested conditions, a one-way ANOVA test was employed. Further analysis with paired t-tests was conducted to determine the statistical significance between pairwise comparisons. For all comparisons, a significance level of $\alpha = 0.05$ was used. The results section presents all quantitative data as mean ± standard error unless otherwise specified.

6.3 Results of Muscular Activity, Metabolic Cost, and Kinematics

6.3.1 Muscular Activity

The assistive device aims to alleviate the effort exerted by specific muscle groups, namely the knee extensors during the stance phase and the hip flexors during the swing phase.

Fig. 6.7 illustrates the results regarding the impact on muscular activity. The top row displays the mean RMS change from the unassisted condition, averaged across subjects, and the bottom row shows the normalized EMG envelopes for a representative subject throughout the gait cycle.

Knee extension assistance led to a significant reduction in the activity of the knee extensors Vastus Medialis—VM, and Vastus Lateralis—VL. The reduction is primarily observed during the stance phase and was evident in both the knee-only and hybrid conditions. In the hybrid condition, the average VM reduction was -30.06±3.68% ($p = 0.0003$), while in the knee-only condition, the reduction was -28.43±6.47% ($p = 0.010$). The hip-only condition resulted in a non-significant reduction of -2.23±5.84% ($p = 0.847$). Further pairwise comparisons revealed a significant difference in changes between the hybrid and hip-only conditions for VM ($p = 0.014$).

Comparable findings were noted for the VL muscle, with assistance resulting in a significant average reduction of -27.66±4.09% ($p = 0.0004$) for the hybrid condition and

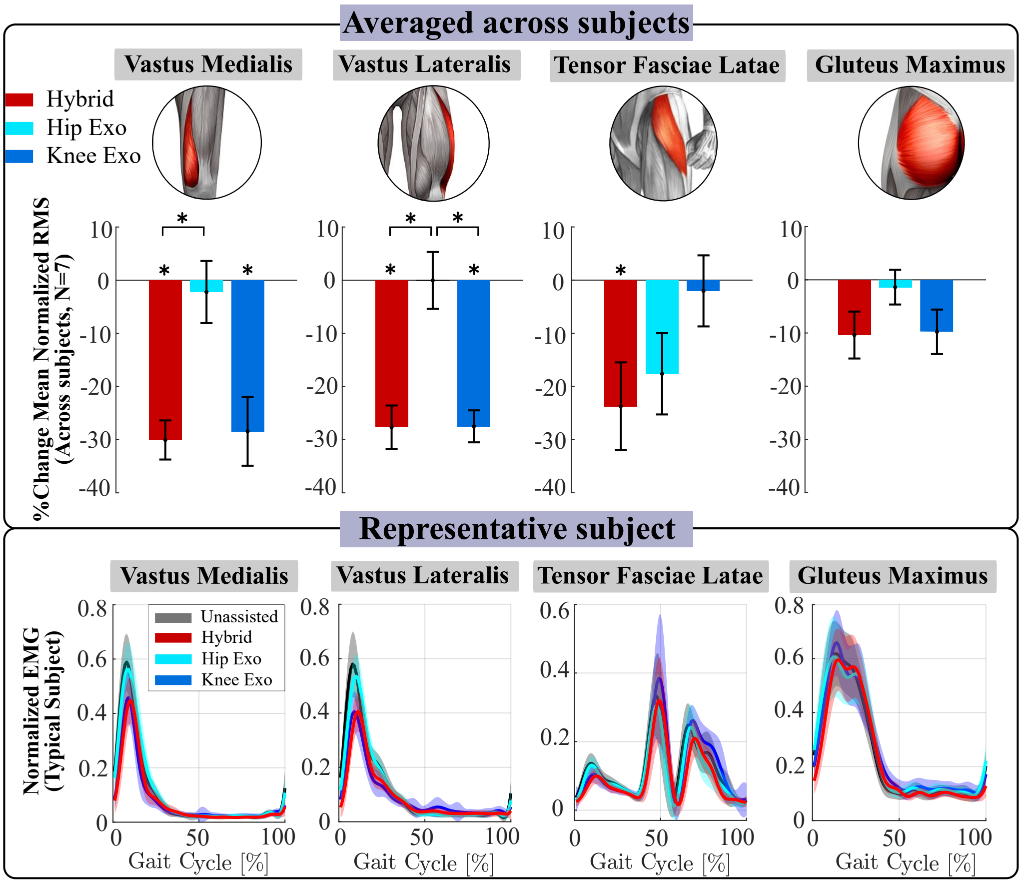

Figure 6.7: Top row illustrates the percentage change in mean RMS EMG from the unassisted condition, averaged across subjects (N=7). Negative values indicate a decrease, while positive values denote an increase in EMG activity. The asterisk (*) below the bars indicates statistically significant differences among conditions ($p < 0.05$). Error bars represent the mean ± standard error. The bottom row presents the normalized EMG activity throughout the gait cycle for a representative subject averaged across steps.

-27.49±3.00% ($p = 0.000$) for the knee-only condition. The hip-only condition exhibited a non-significant change of -0.04±5.34% ($p = 0.910$). Subsequent pairwise comparisons revealed a significant difference in VL change between the hybrid and hip-only conditions ($p = 0.015$), as well as between the knee-only and hip-only conditions ($p = 0.003$).

Tensor Fasciae Latae (TFL) functions as a superficial muscle for hip flexion, and is active during the swing phase (60%-100%), but also playing a role in hip abduction, medial rotation, and stabilization. For TFL, a significant average reduction of -23.79±8.26% ($p = 0.024$) is observed for the hybrid condition. The hip-only condition resulted in a non-significant reduction of -17.64±7.64% ($p = 0.102$) compared to the unassisted condition, and the knee-only condition led to a non-significant reduction of -2.03±6.68% ($p = 0.741$).

The Gluteus Maximus plays a crucial role in extending the hip joint and propelling the body forward. No statistically significant changes were recorded in Gluteus Maximus activity, with a -10.38±4.41% change in the hybrid condition ($p = 0.060$), -1.47±3.25% in the hip-only condition ($p = 0.650$), and -9.78±4.19% in the knee-only condition ($p = 0.055$).

6.3.2 Metabolic Cost

All assisted conditions demonstrated a significantly lower metabolic cost compared to the unassisted condition. The average metabolic cost results are shown in Fig. 6.8.

The unassisted condition resulted in a metabolic cost of 6.81±0.21 W/kg, while the hybrid condition recorded 5.77±0.36 W/kg, the hip-only condition measured 5.96±0.28 W/kg, and the knee-only condition 6.21±0.30 W/kg. The savings between unassisted and hybrid were -15.58±3.53% (p = 0.003), between unassisted and hip-only -12.69±2.32% (p = 0.001), and between unassisted and knee-only -8.83±3.51% (p = 0.038). No significant differences were found between assisted conditions.

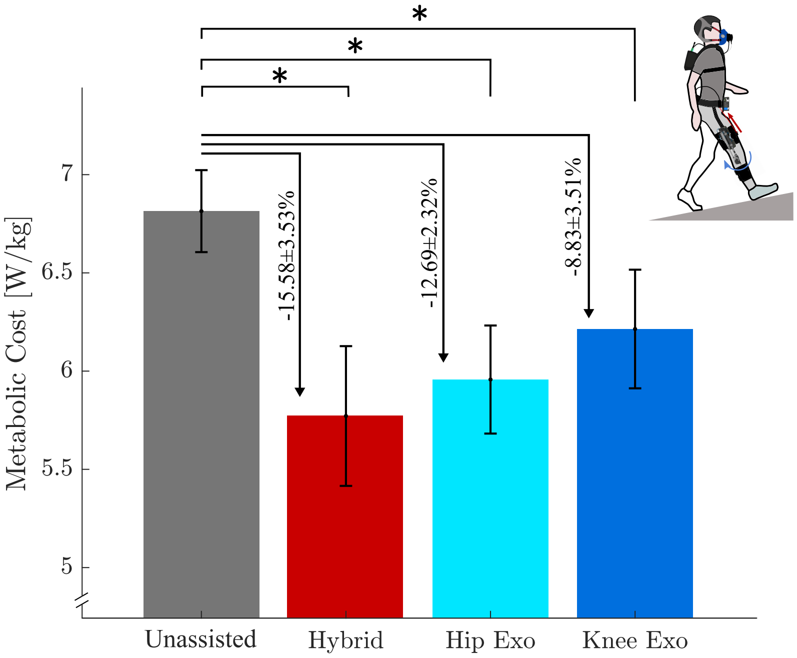

Figure 6.8: Average metabolic costs across subjects (N=7) in each condition. The metabolic cost for all assisted conditions is lower when compared to the unassisted condition. Error bars represent the mean ± standard error. The asterisk (*) denotes a statistically significant difference ($p < 0.05$). Arrows show percentage change from unassisted condition.

6.3.3 Kinematics

Figure 6.9 presents kinematic results, featuring average values across subjects in the top row and values for a representative subject in the bottom row. Across all assistance conditions, joint kinematics exhibited quite consistent patterns. The ANOVA revealed no significant differences ($p > 0.05$) among conditions for four kinematic metrics (knee angle, knee velocity, hip angle, and hip velocity). However, in pairwise t-test comparisons, the p-value for minimum average knee angular velocity was $p = 0.004$ between unassisted and hybrid, and $p = 0.010$ between unassisted and hip-only. For maximum average knee angular velocity, the p-value between unassisted and hybrid was $p = 0.004$, and between unassisted and hip-only was $p = 0.032$ (see Fig. 6.9b). There were no significant changes found in knee and hip angles, and hip velocity.

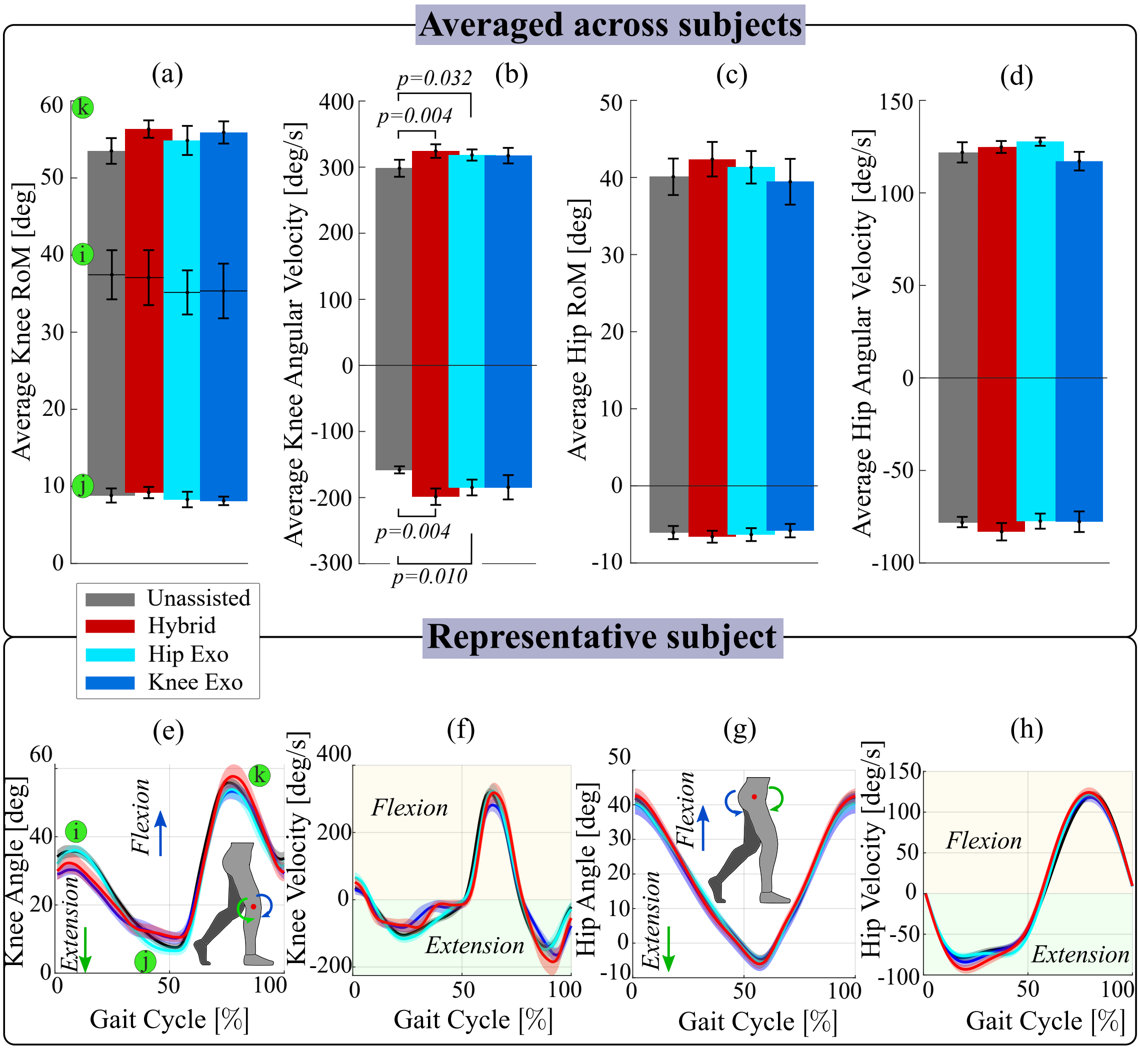

Figure 6.9: The first row shows average kinematic values across subjects (N=7), while the second row shows profiles for a representative subject. (a) Average knee angle RoM; minimum during knee extension, marked with ⓙ, medium during weight acceptance, marked with ⓘ, and maximum during knee flexion in preswing, marked with ⓚ. (b) Average knee angle velocity; (c) Average hip RoM; (d) Average hip angular velocity. In (e), rising knee angle indicates flexion, while falling indicates extension. In (f), positive velocity occurs during knee flexion and negative during extension. In (g), rising hip angle indicates flexion and decreasing indicates extension. (h) Hip velocity is positive during hip flexion and negative during extension.

6.3.4 User Preference

At the end of the experiment, participants were asked about their subjective preferences for different assistance modes, specifically estimating how much it contributed to making walking easier, if deemed effective. They were asked to grade using a scale from 1 to 10 (i.e., 1 = strong disagreement and 10 = strong agreement) whether the specific assisted condition helped them reduce their walking effort compared to an unassisted scenario. All participants rated the assisted conditions as having a positive effect compared to the unassisted condition, with the ratings for knee assistance 6.71±0.49 (mean ± SD), for hip assistance 7.42±0.98 and for hybrid assistance: 9.00±1.00. A significant difference was found in the responses between the hybrid and hip condition $p = 0.0424$ and the hybrid and knee condition $p = 0.0016$. There was no significant difference in responses between hip and knee conditions $p = 0.1403$. The results are shown in Fig. 6.10.

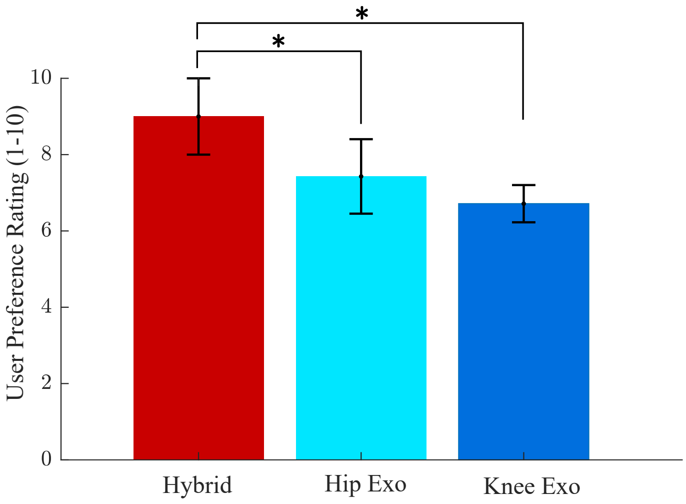

Figure 6.10: User preferences for walking assistance effectiveness compared to unassisted, rated on a scale from 1 (least effective) to 10 (highly effective). The asterisk (*) denotes a statistically significant difference ($p < 0.05$).

6.3.5 Assistance Profiles: Hip Motor and Knee Actuator

Figure 6.11 shows the average assistance from the knee exoskeleton and the average motor torque profiles of the hip actuator. The assistance profiles remained consistent across all operational modes, just turned on or off in various experimental conditions. For knee

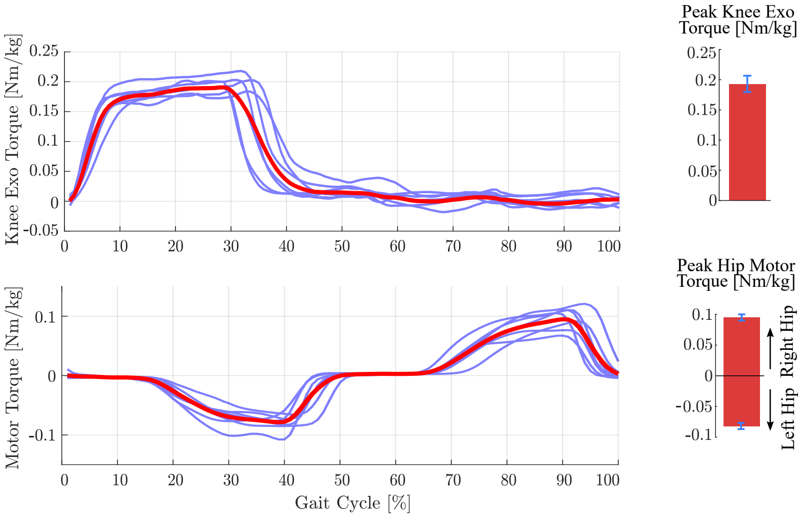

Figure 6.11: The top row depicts the assistance applied by the knee exoskeleton, while the bottom row illustrates the motor torque profiles for hip assistance. Blue lines represent profiles for individual subjects, with the red line indicating the average torque profile across all subjects. Bar charts represent the average mean peak value ± SD.

assistance, we recorded an average peak across subjects of 0.193±0.0135 Nm/kg. For hip assistance, we observed mean motor torque peak values across subjects: 0.095±0.005 Nm/kg for right leg support and -0.080±0.005 Nm/kg for left leg support (mean ± SD).

6.4 Discussion

This study introduced a hybrid assistive device consisting of a soft tendon-driven hip exosuit and a rigid pneumatic knee exoskeleton. The hip exosuit assists the multiple DoF hip joint, simplifying mechanics and avoiding movement restrictions, while the rigid knee exoskeleton supports the single active DoF knee joint, crucial for weight-bearing. The selection of assisting knee extension and hip flexion aligns with peak biomechanical power observed during inclined walking phases, as demonstrated by McIntosh et al. [179]. Given that the metabolic cost of walking includes supporting body weight, generating propulsion, leg swinging, and lateral stabilization [181], the knee exoskeleton aimed to reduce the load related to supporting body weight during the stance, while hip assistance addressed leg swinging, where weight support is not a primary requirement. The knee and hip controllers are independent; the knee controller uses a state machine, while the hip controller uses an adaptive oscillator at the high level to estimate the gait phase, and generates a reference velocity for the actuator via cubic spline interpolation at the low level. The knee joint displays several changes between flexion and extension throughout the gait cycle, reflecting a more variable kinematic pattern compared to the hip joint which transitions from extension to flexion only once during the gait cycle. To ensure effective knee assistance, precise detection of gait events is crucial. The knee's state machine controller offers discrete, phase-specific assistance by accurately identifying the initial contact and knee swing events. Meanwhile, adaptive oscillators excel in managing periodic motions by mirroring the cyclic dynamics of the hip, thereby ensuring smooth, continuous control that can adapt to variations in gait speed [182]–[184]. The combination of these controllers creates a synergistic interaction, where the precise and deterministic control from the knee's state machine complements the adaptive nature of the hip's oscillation-based controller.

In the experiments, all assisted conditions led to significant reductions in participants' metabolic costs compared to the unassisted condition. The most substantial significant reduction occurred in the hybrid condition, ∼16%. The hip condition resulted in an average reduction of ∼13%, while the knee condition achieved a reduction of approximately ∼9%. This outcome supports the study's initial hypothesis, indicating that the greatest reduction is achieved with hybrid assistance rather than with assistance from a single joint or with the unassisted condition. This finding is consistent with musculoskeletal simulations by Bianco et al. [188] and the study conducted by Franks et al. [189], where assistive torque at different lower limb joints was correlated with metabolic cost. In the latter study, applying assistance torque solely to the hip led to a 26% reduction in metabolic cost, while the combined hip and knee assistance resulted in a 33% reduction compared to wearing the device with no torque. Although the trends are comparable, direct numerical comparisons are challenging due to variations in device mass, treadmill inclination, and assistance profiles. The metabolic reduction trends observed in this study align with biomechanical principles outlined in [54]. Namely, in level ground walking, the hip joint primarily contributes to positive biological power, while the net biological power at the knee is slightly negative. Therefore, in such a scenario, it is anticipated that the majority of benefits would stem from the hip module. Conversely, during decline walking, the net biological power at the knee becomes more negative, while the hip joint power remains slightly positive [54]. Therefore, in such a scenario, it is speculated that the knee module, functioning as a passive damper, could potentially yield most of the benefits in this context. However, transitioning to inclined walking amplifies the positive power exerted by both the hip and knee joints. The hip joint predominantly performs positive work, while the knee joint primarily generates positive power, necessitating increased activation of the quadriceps muscles to support and lift body weight. This suggests that the benefits from the hybrid assistive device are most pronounced for both joints during inclined walking, where both the hip and knee joints exert increased positive net biological power. Similar findings were experimentally measured respectively for the hip in [12] and for the knee in [88].

It is noteworthy that the average users' preferences reflect the average results from the metabolic cost measurements. All users unanimously confirmed that the assistance methods were advantageous compared to the unassisted condition. Among the different assistance modes, knee-only assistance was the least preferred, followed by hip-only assistance, and hybrid assistance received the highest preference rating. There was a significant difference between responses for hybrid vs. hip and hybrid vs. knee, but not between hip and knee, suggesting that responses between these two conditions were relatively similar.

Through the use of EMG sensors to measure muscle activity, it was established that knee extension assistance torque significantly reduced the activation of knee extensor muscles compared to both unassisted and hip-only conditions. Specifically, Vastus Medialis' activity was reduced by ∼30% and Vastus Lateralis exhibited a similar reduction of ∼28% with knee assistance active. For comparison, in Lee et al.'s study, inclined walking with an active electromechanical knee exoskeleton showed reductions of -16.0% for the Vastus Lateralis and -15.1% for the Vastus Medialis when applying a biological torque controller with a peak torque of 0.2 Nm/kg during the stance phase [88]. The use of a pneumatic cylinder may have contributed to a more abrupt torque application, potentially resulting in a higher muscle activity reduction when using quadriceps to lift the body's weight. However, the abrupt movement might have affected the shape of the knee velocity profile during the stance phase. This deviation of knee velocity is visible in the bottom row of Figure 6.9f. The study from Lee et al. also revealed heightened activity in the hamstring muscle attributed to the antagonistic interaction between the quadriceps and hamstrings. However, our study, limited by thigh braces covering a substantial area of the hamstrings, could not reveal whether there would be increased activity in the hamstrings comparable to their scenario.

The primary hip flexor muscles, such as the Iliacus, reside internally and cannot be measured with surface electrodes. The main superficial hip flexor is the Rectus Femoris, whose examination was restrained due to thigh braces covering the muscle. As an alternative, Tensor Fasciae Latae (TFL) was chosen, where it is expected that the observed effects should be comparable since TFL serves as the superficial hip flexor, active during the swing phase, but also contributes to hip abduction, medial rotation, and stabilization. The TFL exhibited a significant reduction of ∼24% in the hybrid-assisted condition. Surprisingly, the anticipated statistically significant reduction in the hip-only condition did not manifest, even though the activity was reduced ∼18%. This discrepancy could be attributed to the multifaceted role of the TFL, which extends beyond hip flexion, making it active at various intervals during the gait cycle. Therefore, the hybrid condition achieved greater reductions in TFL activity, and was statistically significant, compared to the hip-only condition, where no statistical difference was found. However, given the impact of hip flexion assistance on metabolic cost, we speculate that the primary internal hip flexors would demonstrate larger reduction trends.

Earlier investigations into exoskeletons have demonstrated that powered assistance can influence not only the muscle activation and biomechanical kinetics of the targeted joints but also result in the redistribution of energy to other joints [11], [190]. An observed trend was the average reduction of $\sim$10% in Gluteus Maximus muscle activity in conditions when the knee extension assistance was active, suggesting a potential correlation with the assistance during the load response phase. However, this result was not statistically significant, making it premature to draw conclusive interpretations.

The preliminary kinematic evaluations relied solely on IMU sensors within the exosuit and an encoder for knee kinematics measurement. While ANOVA results did not reveal a significant overall difference among the four conditions, further analysis using pairwise t-tests suggested potential alterations in knee velocity profiles, particularly for minimum values between unassisted and hybrid, and unassisted and hip-only conditions, as well as maximum knee angular velocity between unassisted and hybrid, and unassisted and hip-only. This suggests that knee velocity reached higher peaks in both flexion and extension during the swing phase when hip flexion assistance was activated. However, given the sample size and the lack of strong evidence to reject the null hypothesis, caution is warranted in drawing definitive conclusions at this stage. Notably, there were no significant average changes observed in knee angle, hip angle, and hip velocity peaks. Future investigations should consider incorporating advanced optical measuring tools to provide a more comprehensive analysis of overall body posture and joint angles.

In discussing limitations, it's important to note that we assessed the hybrid assistive device across four conditions but omitted walking trials without the device. Instead, we established the baseline as walking in an unassisted transparent mode to specifically evaluate the impact of single versus multi-joint assistance within a hybrid system. This approach is common in laboratory evaluations aimed at assessing the effects of control or hardware modifications, as described in [69]. Additionally, the measuring kinematic sensors were directly connected to the wearable device, further influencing our methodology. Another limitation was the inability to measure hamstring activity and the Rectus Femoris, the primary superficial hip flexor. This limitation stemmed from the design of the exoskeleton, which includes thigh braces covering the leg surface of the suggested sensor placement.

6.4.1 Versatility of the Proposed Hybrid Configuration

The hybrid configuration proposed in this chapter has the potential to extend its applicability to various combinations of human joints. By adopting this approach, a singular active degree-of-freedom joint, pivotal for tasks such as lifting or weight carrying, can be effectively assisted using rigid exoskeletons. Simultaneously, joints with multiple degrees of freedom can benefit from a tendon-driven exosuit, providing simplified mechanics, minimized weight, and unrestricted motion across all axes of movement. In Figure 6.12a, the proposed hybrid configuration is illustrated, while in (b), a similar concept is proposed for upper limb joints, specifically the combination of the shoulder and elbow. With the shoulder's 3 degrees of freedom (DoF), a tendon-driven configuration simplifies mechanics, enabling unrestricted assistance in all axes. Conversely, the elbow, where torque is vital for lifting through antagonistic biceps-triceps activity, benefits from direct torque application, offering bidirectional support and precise control during lifting tasks.

6.5 Chapter Conclusion

In this study, we introduced a novel exoskeletal configuration, a hybrid assistive device with a soft tendon-driven hip exosuit and a rigid pneumatic knee exoskeleton interconnected through a thigh brace. Such a configuration is proposed to reduce mechanical complexity and space constraints in higher DoF joints, particularly the hip, while ensuring direct torque application through a rigid system in the single DoF knee joint, which is essential for

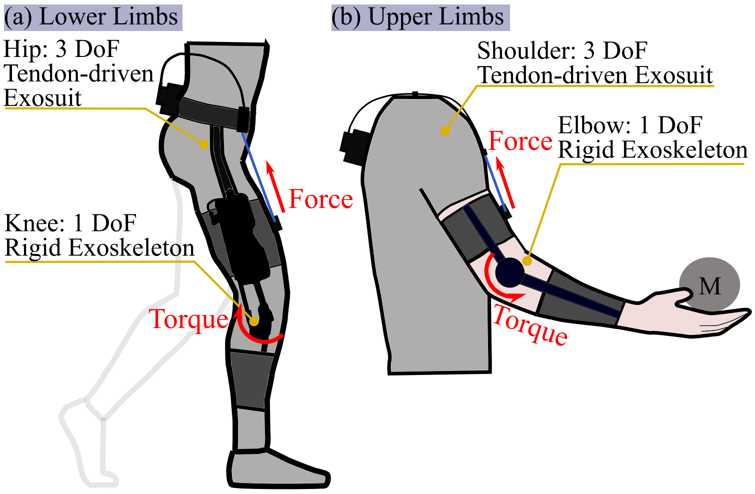

Figure 6.12: Versatility of Hybrid Rigid-Soft Configurations: (a) Illustration depicting the proposed concept discussed in this chapter, showcasing a rigid knee exoskeleton paired with a tendon-driven hip exosuit. (b) Hypothetical concept demonstrating potential upper limb configurations, including a rigid elbow exoskeleton coupled with a tendon-driven shoulder exosuit.

lifting and holding body weight in inclined walking. Tested in four conditions, all assisted conditions reduced metabolic cost compared to unassisted, with the hybrid exhibiting the most significant reduction ∼16%, followed by hip-only ∼13% and knee-only ∼9%. Additional decreases in muscular activity for knee extensors (∼29%) and hip flexors (∼24%) were observed, accompanied by minor changes in kinematics. Further research will involve detailed kinematic analyses and exploration of optimization strategies for enhanced device assistance at different experimental setups.

Chapter 7

Conclusion

This doctoral dissertation aimed to address critical challenges in exoskeleton research: actuation, control, mechanical design, and attachment to the human body. It specifically focused on novel pneumatic mechanisms with variable stiffness, capable of changing stiffness without an external air supply by using a new methodology to accumulate air within the pneumatic cylinder. The dissertation also explored innovative approaches for delivering and recovering pneumatic energy. Lastly, it examined synergies between tendon-driven electromechanical soft exosuit and pneumatic rigid exoskeleton to create a hybrid rigid-soft multi-joint device, simplifying mechanics and optimizing functionality and effectiveness. Considering the goals and hypotheses outlined at the beginning, most were successfully validated. A summary of the main **scientific contributions** are given below.

1. The first milestone successfully demonstrated air pressure modulation through air harvesting in a novel quasi-passive mechanism without an external air supply, thus altering the stiffness of the pneumatic cylinder. A significant contribution to the state of the art is our innovative method for accumulating air in a slim lightweight mechanism, where stiffness is independent of the lever arm length. Moreover, our mechanism allows for simultaneous increases in stiffness and energy storage capacity, a capability not found in other variable stiffness mechanisms. Therefore, our solution offers better adaptability to different situations.

2. The second milestone successfully developed the exoskeleton joint by applying a previously developed air accumulation methodology to adjust stiffness. This novel design incorporated a pneumatic artificial muscle to store accumulated air, which also plays a role in altering the lever arm length and influencing stiffness. Such a stiffness modulation method has not been reported in the literature until now. Thanks to this, the exoskeleton joint has a high energy storage capacity compared to other similar devices and has adjustable stiffness, which can also be increased by the air accumulation method. This feature makes it particularly suitable for quasi-passive knee exoskeletons.

3. With the completion of the third milestone, the entire exoskeleton was assembled and demonstrated its ability to operate in both quasi-passive and active modes within a single actuator. This flexibility not only enhanced energy efficiency but also demonstrated the potential of pneumatic exoskeletons and robots to recycle compressed air for productive work, thereby reducing energy consumption and the time required to produce compressed air using an air pump. A significant contribution of this milestone is in biomechanical energy harvesting, which was experimentally validated in sit-stand tasks—an area previously unexplored in the field.

4. The fourth milestone focused on evaluating a newly proposed hybrid rigid-soft assistive device combining pneumatic and electromechanical tendon-driven configurations. The advantage of employing this configuration is to use robust rigid structures for assistance during weight-bearing phases, while utilizing soft tendon-driven actuation for human joints with higher degrees of freedom to assist during the swing phase. This approach simplifies the mechanical design of exoskeletons, which would otherwise require passive metal mechanisms to accommodate all moving axes. This synergy was utilized to assist hip and knee joints during walking and was tested on human subjects. A rigid exoskeleton was specifically designed for the knee joint to assist in the stance phase, while a soft tendon-driven exosuit was applied to the hip joint to assist hip flexion.

While the dissertation has made strides in addressing specific challenges, there are still ongoing issues to tackle in the field of pneumatic exoskeletons. One unresolved aspect is the development of a portable pneumatic source capable of actively delivering compressed air at frequencies suitable for walking without excessive noise and weight. A potential solution could involve designing the pneumatic source with switching regimes, such as alternating between supplying and recovering the compressed air. This approach would ensure that compressed air from the actuator is not released into the atmosphere as it is usually done, but is instead supplied and recovered back, similar to the methodology outlined in the sit-stand experiments detailed in this dissertation. The key difference would be that instead of relying on the human body to recover air, the power source should be capable of generating enough vacuum to recover the air. This could potentially be integrated with soft inflatable actuators, which have recently garnered attention [191], [192]. Exosuits represent a promising direction in research as they address many challenges. The implementation of both rigid and soft configurations could prove pivotal for advancement. Therefore, future work will focus on tackling these technically unresolved challenges and integrating them into exosuits.

References

[1] C. Siviy, L. M. Baker, B. T. Quinlivan, *et al.*, "Opportunities and challenges in the development of exoskeletons for locomotor assistance," *Nature Biomedical Engineering*, vol. 7, no. April, pp. 456–472, 2023. DOI: `10.1038/s41551-022-00984-1`.

[2] R. Auberger, M. F. Russold, R. Riener, and H. Dietl, "Patient Motion Using a Computerized Leg Brace in Everyday Locomotion Tasks," *IEEE Transactions on Medical Robotics and Bionics*, vol. 1, no. 2, pp. 106–114, 2019. DOI: `10.1109/tmrb.2019.2913429`.

[3] F. L. Haufe, K. Schmidt, J. E. Duarte, P. Wolf, R. Riener, and M. Xiloyannis, "Activity-based training with the Myosuit: A safety and feasibility study across diverse gait disorders," *Journal of NeuroEngineering and Rehabilitation*, vol. 17, no. 1, pp. 1–11, 2020, ISSN: 17430003. DOI: `10.1186/s12984-020-00765-4`. [Online]. Available: `https://doi.org/10.1186/s12984-020-00765-4`.

[4] Z. F. Lerner, D. L. Damiano, and T. C. Bulea, "The effects of exoskeleton assisted knee extension on lower-extremity gait kinematics, kinetics, and muscle activity in children with cerebral palsy," *Scientific Reports*, vol. 7, no. 1, pp. 1–12, 2017, ISSN: 20452322. DOI: `10.1038/s41598-017-13554-2`. [Online]. Available: `http://dx.doi.org/10.1038/s41598-017-13554-2`.

[5] A. Stilli, A. Cremoni, M. Bianchi, *et al.*, "AirExGlove-A novel pneumatic exoskeleton glove for adaptive hand rehabilitation in post-stroke patients," *2018 IEEE International Conference on Soft Robotics, RoboSoft 2018*, pp. 579–584, 2018. DOI: `10.1109/ROBOSOFT.2018.8405388`.

[6] N. Singh, M. Saini, N. Kumar, M. P. Srivastava, and A. Mehndiratta, "Evidence of neuroplasticity with robotic hand exoskeleton for post-stroke rehabilitation: A randomized controlled trial," *Journal of neuroengineering and rehabilitation*, vol. 18, no. 1, p. 76, 2021.

[7] A. S. Khan, D. C. Livingstone, C. L. Hurd, *et al.*, "Retraining walking over ground in a powered exoskeleton after spinal cord injury: A prospective cohort study to examine functional gains and neuroplasticity," *Journal of neuroengineering and rehabilitation*, vol. 16, pp. 1–17, 2019.

[8] R. S. Calabrò, A. Naro, M. Russo, *et al.*, "Shaping neuroplasticity by using powered exoskeletons in patients with stroke: A randomized clinical trial," *Journal of neuroengineering and rehabilitation*, vol. 15, pp. 1–16, 2018.

[9] O. Mubin, F. Alnajjar, N. Jishtu, B. Alsinglawi, and A. Al Mahmud, "Exoskeletons with virtual reality, augmented reality, and gamification for stroke patients' rehabilitation: Systematic review," *JMIR rehabilitation and assistive technologies*, vol. 6, no. 2, e12010, 2019.

[10] J. Moon, K. Nam, J. Ryu, *et al.*, “Reducing sprint time with exosuit assistance in the real world,” *Science Robotics*, vol. 8, no. 82, eadf5611, 2023. DOI: `10.1126/scirobotics.adf5611`. eprint: `https://www.science.org/doi/pdf/10.1126/scirobotics.adf5611`. [Online]. Available: `https://www.science.org/doi/abs/10.1126/scirobotics.adf5611`.

[11] J. Kim, G. Lee, R. Heimgartner, *et al.*, “Reducing the metabolic rate of walking and running with a versatile, portable exosuit,” *Science*, vol. 365, no. 6454, pp. 668–672, 2019, ISSN: 10959203. DOI: `10.1126/science.aav7536`.

[12] K. Seo, J. Lee, and Y. J. Park, “Autonomous hip exoskeleton saves metabolic cost of walking uphill,” *IEEE International Conference on Rehabilitation Robotics*, pp. 246–251, 2017, ISSN: 19457901. DOI: `10.1109/ICORR.2017.8009254`.

[13] C. Rognon, B. Stephens-Fripp, J. Hartcher-O’Brien, B. Rost, and A. Israr, “Linking Haptic Parameters to the Emotional Space for Mediated Social Touch,” *Frontiers in Computer Science*, vol. 4, no. May, pp. 1–14, 2022, ISSN: 26249898. DOI: `10.3389/fcomp.2022.826545`.

[14] F. Missiroli, N. Lotti, E. Tricomi, *et al.*, “Rigid, Soft, Passive, and Active: A Hybrid Occupational Exoskeleton for Bimanual Multijoint Assistance,” *IEEE Robotics and Automation Letters*, vol. 7, no. 2, pp. 2557–2564, 2022, ISSN: 23773766. DOI: `10.1109/LRA.2022.3142447`.

[15] S. J. Baltrusch, J. H. van Dieën, A. S. Koopman, *et al.*, “SPEXOR passive spinal exoskeleton decreases metabolic cost during symmetric repetitive lifting,” *European Journal of Applied Physiology*, vol. 120, no. 2, pp. 401–412, 2020, ISSN: 14396327. DOI: `10.1007/s00421-019-04284-6`. [Online]. Available: `https://doi.org/10.1007/s00421-019-04284-6`.

[16] C. Latella, Y. Tirupachuri, L. Tagliapietra, *et al.*, “Analysis of Human Whole-Body Joint Torques During Overhead Work With a Passive Exoskeleton,” *IEEE Transactions on Human-Machine Systems*, vol. 52, no. 5, pp. 1060–1068, 2022, ISSN: 21682305. DOI: `10.1109/THMS.2021.3128892`.

[17] S. De Bock, M. Rossini, D. Lefeber, *et al.*, “An Occupational Shoulder Exoskeleton Reduces Muscle Activity and Fatigue During Overhead Work,” *IEEE Transactions on Biomedical Engineering*, vol. 69, no. 10, pp. 3008–3020, 2022, ISSN: 15582531. DOI: `10.1109/TBME.2022.3159094`.

[18] S. Toxiri, M. B. Näf, M. Lazzaroni, *et al.*, “Back-support exoskeletons for occupational use: An overview of technological advances and trends,” *IISE Transactions on Occupational Ergonomics and Human Factors*, vol. 7, no. 3-4, pp. 237–249, 2019, ISSN: 24725846. DOI: `10.1080/24725838.2019.1626303`. [Online]. Available: `https://doi.org/10.1080/24725838.2019.1626303`.

[19] “Occupational exoskeletons: A roadmap toward large-scale adoption. Methodology and challenges of bringing exoskeletons to workplaces,” *Wearable Technologies*, vol. 2, 2021, ISSN: 26317176. DOI: `10.1017/wtc.2021.11`.

[20] S. Lee, J. Kim, L. Baker, *et al.*, “Autonomous multi-joint soft exsosuit with online optimization reduces energy cost of loaded walking,” *Journal of NeuroEngineering and Rehabilitation*, Under review, 2018.

[21] W. Cao, C. Chen, D. Wang, *et al.*, “A Lower Limb Exoskeleton with Rigid and Soft Structure for Loaded Walking Assistance,” *IEEE Robotics and Automation Letters*, vol. 7, no. 1, pp. 454–461, 2022, ISSN: 23773766. DOI: `10.1109/LRA.2021.3125723`.

[22] P. Malcolm, S. Lee, S. Crea, *et al.*, “Varying negative work assistance at the ankle with a soft exosuit during loaded walking,” *Journal of NeuroEngineering and Rehabilitation*, vol. 14, no. 1, pp. 1–12, 2017, ISSN: 17430003. DOI: `10.1186/s12984-017-0267-5`.

[23] C. J. Walsh, K. Endo, and H. Herr, “A quasi-passive leg exoskeleton for load-carrying augmentation,” *International Journal of Humanoid Robotics*, vol. 4, no. 3, pp. 487–506, 2007, ISSN: 02198436. DOI: `10.1142/S0219843607001126`.

[24] “Exobuddy - A Non-Anthropomorphic Quasi-Passive Exoskeleton for Load Carrying Assistance,” *Proceedings of the IEEE RAS and EMBS International Conference on Biomedical Robotics and Biomechatronics*, vol. 2018-Augus, pp. 336–341, 2018, ISSN: 21551774. DOI: `10.1109/BIOROB.2018.8487794`.

[25] D. J. Farris, D. J. Harris, H. M. Rice, *et al.*, “A systematic literature review of evidence for the use of assistive exoskeletons in defence and security use cases,” *Ergonomics*, vol. 66, no. 1, pp. 61–87, 2023, ISSN: 13665847. DOI: `10.1080/00140139.2022.2059106`. [Online]. Available: `https://doi.org/10.1080/00140139.2022.2059106`.

[26] S. H. Collins, M. Bruce Wiggin, and G. S. Sawicki, “Reducing the energy cost of human walking using an unpowered exoskeleton,” *Nature*, vol. 522, no. 7555, pp. 212–215, 2015, ISSN: 14764687. DOI: `10.1038/nature14288`.

[27] M. B. Yandell, J. R. Tacca, and K. E. Zelik, “Design of a Low Profile, Unpowered Ankle Exoskeleton That Fits Under Clothes: Overcoming Practical Barriers to Widespread Societal Adoption,” *IEEE Transactions on Neural Systems and Rehabilitation Engineering*, vol. 27, no. 4, pp. 712–723, 2019, ISSN: 15580210. DOI: `10.1109/TNSRE.2019.2904924`.

[28] P. Maurice, S. Ivaldi, J. Babic, *et al.*, “Objective and Subjective Effects of a Passive Exoskeleton on Overhead Work,” *IEEE Transactions on Neural Systems and Rehabilitation Engineering*, vol. 28, no. 1, pp. 152–164, 2020, ISSN: 15580210. DOI: `10.1109/TNSRE.2019.2945368`.

[29] E. Etenzi, R. Borzuola, and A. M. Grabowski, “Passive-elastic knee-ankle exoskeleton reduces the metabolic cost of walking,” pp. 1–15, 2020.

[30] R. Nasiri, A. Ahmadi, and M. N. Ahmadabadi, “Reducing the energy cost of human running using an unpowered exoskeleton,” *IEEE Transactions on Neural Systems and Rehabilitation Engineering*, vol. 26, no. 10, pp. 2026–2032, 2018, ISSN: 15344320. DOI: `10.1109/TNSRE.2018.2872889`.

[31] F. A. Panizzolo, C. Bolgiani, L. Di Liddo, E. Annese, and G. Marcolin, “Reducing the energy cost of walking in older adults using a passive hip flexion device,” *Journal of NeuroEngineering and Rehabilitation*, vol. 16, no. 1, pp. 1–9, 2019, ISSN: 17430003. DOI: `10.1186/s12984-019-0599-4`.

[32] M. Goršič, Y. Song, B. Dai, and V. D. Novak, “Short-term effects of the Auxivo LiftSuit during lifting and static leaning,” *Applied Ergonomics*, vol. 102, no. April, 2022, ISSN: 18729126. DOI: `10.1016/j.apergo.2022.103765`.

[33] S. Kumar, M. R. Zwall, E. A. Bolivar-Nieto, R. D. Gregg, and N. Gans, “Extremum Seeking Control for Stiffness Auto-Tuning of a Quasi-Passive Ankle Exoskeleton,” *IEEE Robotics and Automation Letters*, vol. 5, no. 3, pp. 4604–4611, 2020, ISSN: 23773766. DOI: `10.1109/LRA.2020.3001541`.

[34] C. Di Natali, A. Sadeghi, A. Mondini, *et al.*, "Pneumatic Quasi-Passive Actuation for Soft Assistive Lower Limbs Exoskeleton," *Frontiers in Neurorobotics*, vol. 14, no. June, pp. 1–18, 2020, ISSN: 16625218. DOI: `10.3389/fnbot.2020.00031`.

[35] M. Jamšek, T. Petrič, and J. Babič, "Gaussian mixture models for control of Quasi-passive spinal exoskeletons," *Sensors (Switzerland)*, vol. 20, no. 9, pp. 1–13, 2020, ISSN: 14248220. DOI: `10.3390/s20092705`.

[36] G. Elliott, A. Marecki, and H. Herr, "Design of a clutch-spring knee exoskeleton for running," *Journal of Medical Devices, Transactions of the ASME*, vol. 8, no. 3, pp. 1–11, 2014, ISSN: 1932619X. DOI: `10.1115/1.4027841`.

[37] M. K. Ishmael, D. Archangeli, and T. Lenzi, "A Powered Hip Exoskeleton With High Torque Density for Walking, Running, and Stair Ascent," *IEEE/ASME Transactions on Mechatronics*, vol. PP, pp. 1–12, 2022, ISSN: 1083-4435. DOI: `10.1109/tmech.2022.3159506`.

[38] M. K. Shepherd and E. J. Rouse, "Design and Validation of a Torque-Controllable Knee Exoskeleton for Sit-to-Stand Assistance," *IEEE/ASME Transactions on Mechatronics*, vol. 22, no. 4, pp. 1695–1704, 2017, ISSN: 10834435. DOI: `10.1109/TMECH.2017.2704521`.

[39] D. Lee, E. C. Kwak, B. J. McLain, I. Kang, and A. J. Young, "Effects of Assistance during Early Stance Phase Using a Robotic Knee Orthosis on Energetics, Muscle Activity, and Joint Mechanics during Incline and Decline Walking," *IEEE Transactions on Neural Systems and Rehabilitation Engineering*, vol. 28, no. 4, pp. 914–923, 2020, ISSN: 15580210. DOI: `10.1109/TNSRE.2020.2972323`.

[40] P. Slade, M. J. Kochenderfer, S. L. Delp, and S. H. Collins, "Personalizing exoskeleton assistance while walking in the real world," *Nature*, vol. 610, no. 7931, pp. 277–282, 2022, ISSN: 14764687. DOI: `10.1038/s41586-022-05191-1`.

[41] U. Heo, S. J. Kim, and J. Kim, "Backdrivable and Fully-Portable Pneumatic Back Support Exoskeleton for Lifting Assistance," *IEEE Robotics and Automation Letters*, vol. 5, no. 2, pp. 2047–2053, 2020, ISSN: 23773766. DOI: `10.1109/LRA.2020.2969169`.

[42] S. J. Kim, H. Chang, J. Park, and J. Kim, "Design of a Portable Pneumatic Power Source with High Output Pressure for Wearable Robotic Applications," *IEEE Robotics and Automation Letters*, vol. 3, no. 4, pp. 4351–4358, 2018, ISSN: 23773766. DOI: `10.1109/LRA.2018.2864823`.

[43] J. Chung, R. Heimgartner, C. T. Oneill, N. S. Phipps, and C. J. Walsh, "ExoBoot, a Soft Inflatable Robotic Boot to Assist Ankle during Walking: Design, Characterization and Preliminary Tests," *Proceedings of the IEEE RAS and EMBS International Conference on Biomedical Robotics and Biomechatronics*, vol. 2018-August, pp. 509–516, 2018, ISSN: 21551774. DOI: `10.1109/BIOROB.2018.8487903`.

[44] M. Wehner, B. Quinlivan, P. M. Aubin, *et al.*, "A lightweight soft exosuit for gait assistance," *Proceedings - IEEE International Conference on Robotics and Automation*, pp. 3362–3369, 2013, ISSN: 10504729. DOI: `10.1109/ICRA.2013.6631046`.

[45] C. M. Thalman, T. Hertzell, and H. Lee, "Toward A Soft Robotic Ankle-Foot Orthosis (SR-AFO) Exosuit for Human Locomotion: Preliminary Results in Late Stance Plantarflexion Assistance," *2020 3rd IEEE International Conference on Soft Robotics, RoboSoft 2020*, pp. 801–807, 2020. DOI: `10.1109/RoboSoft48309.2020.9116050`.

[46] M. Wehner, B. Quinlivan, P. M. Aubin, *et al.*, "A lightweight soft exosuit for gait assistance," *Proceedings - IEEE International Conference on Robotics and Automation*, pp. 3362–3369, 2013, ISSN: 10504729. DOI: `10.1109/ICRA.2013.6631046`.

[47] C. P. Chou and B. Hannaford, "Measurement and modeling of McKibben pneumatic artificial muscles," *IEEE Transactions on Robotics and Automation*, vol. 12, no. 1, pp. 90–102, 1996, ISSN: 1042296X. DOI: `10.1109/70.481753`.

[48] T. Lee, D. Lee, B. Song, and Y. Su Baek, "Design and control of a polycentric knee exoskeleton using an electro-hydraulic actuator," *Sensors (Switzerland)*, vol. 20, no. 1, 2020, ISSN: 14248220. DOI: `10.3390/s20010211`.

[49] O. Mohseni, F. Gagey, G. Zhao, A. Seyfarth, and M. A. Sharbafi, "How far are Pneumatic Artificial Muscles from biological muscles?" *Proceedings - IEEE International Conference on Robotics and Automation*, pp. 1909–1915, 2020, ISSN: 10504729. DOI: `10.1109/ICRA40945.2020.9197177`.

[50] R. Baud, A. R. Manzoori, A. Ijspeert, and M. Bouri, "Review of control strategies for lower-limb exoskeletons to assist gait," *Journal of NeuroEngineering and Rehabilitation*, vol. 18, no. 1, pp. 1–34, 2021, ISSN: 17430003. DOI: `10.1186/s12984-021-00906-3`. [Online]. Available: `https://doi.org/10.1186/s12984-021-00906-3`.

[51] M. A. Diaz, M. Voss, A. Dillen, *et al.*, "Human-in-the-loop optimization of wearable robotic devices to improve human–robot interaction: A systematic review," *IEEE Transactions on Cybernetics*, vol. 53, no. 12, pp. 7483–7496, 2022.

[52] S. Baltrusch, "Lifting Success of Trunk Exoskeletons. Bridging the gap between biomechanical solutions and end-users' perceptions.," Ph.D. dissertation, Vrije Universiteit Amsterdam, 2020, ISBN: 9789463758833.

[53] W. Liang, H. Liu, K. Wang, Z. Qian, L. Ren, and L. Ren, "Comparative study of robotic artificial actuators and biological muscle," *Advances in Mechanical Engineering*, vol. 12, no. 6, pp. 1–25, 2020, ISSN: 16878140. DOI: `10.1177/1687814020933409`.

[54] R. W. Nuckols, K. Z. Takahashi, D. J. Farris, S. Mizrachi, R. Riemer, and G. S. Sawicki, "Mechanics of walking and running up and downhill: A joint-level perspective to guide design of lower-limb exoskeletons," *PLoS ONE*, vol. 15, no. 8 August, pp. 1–20, 2020, ISSN: 19326203. DOI: `10.1371/journal.pone.0231996`.

[55] R. A. Shveda, A. Rajappan, T. F. Yap, *et al.*, "A wearable textile-based pneumatic energy harvesting system for assistive robotics," *Science Advances*, vol. 8, no. 34, pp. 1–11, 2022, ISSN: 23752548. DOI: `10.1126/sciadv.abo2418`.

[56] R. S. Diteesawat, T. Helps, M. Taghavi, and J. Rossiter, "Electro-pneumatic pumps for soft robotics," *Science Robotics*, vol. 6, no. 51, pp. 1–12, 2021, ISSN: 24709476. DOI: `10.1126/SCIROBOTICS.ABC3721`.

[57] M. Xiloyannis, R. Alicea, A. M. Georgarakis, *et al.*, "Soft Robotic Suits: State of the Art, Core Technologies, and Open Challenges," *IEEE Transactions on Robotics*, vol. 38, no. 3, pp. 1343–1362, 2022, ISSN: 19410468. DOI: `10.1109/TRO.2021.3084466`.

[58] F. Hussain, R. Goecke, and M. Mohammadian, "Exoskeleton robots for lower limb assistance: A review of materials, actuation, and manufacturing methods," *Proceedings of the Institution of Mechanical Engineers, Part H: Journal of Engineering in Medicine*, vol. 235, no. 12, pp. 1375–1385, 2021.

[59] E. Tricomi, M. Mossini, F. Missiroli, *et al.*, "Environment-based Assistance Modulation for a Hip Exosuit via Computer Vision," *IEEE Robotics and Automation Letters*, pp. 1–8, 2023.

[60] B. Laschowski, W. McNally, A. Wong, and J. McPhee, "Environment classification for robotic leg prostheses and exoskeletons using deep convolutional neural networks," *Frontiers in Neurorobotics*, vol. 15, p. 730 965, 2022.

[61] S. R. Soekadar, M. Witkowski, C. Gómez, *et al.*, "Hybrid eeg/eog-based brain/neural hand exoskeleton restores fully independent daily living activities after quadriplegia," *Science Robotics*, vol. 1, no. 1, eaag3296, 2016. DOI: `10.1126/scirobotics.aag3296`. eprint: `https://www.science.org/doi/pdf/10.1126/scirobotics.aag3296`. [Online]. Available: `https://www.science.org/doi/abs/10.1126/scirobotics.aag3296`.

[62] Y. Ding, M. Kim, S. Kuindersma, and C. J. Walsh, "Human-in-the-loop optimization of hip assistance with a soft exosuit during walking," *Science Robotics*, vol. 3, no. 15, pp. 1–9, 2018, ISSN: 24709476. DOI: `10.1126/scirobotics.aar5438`.

[63] J. Babič, M. Laffranchi, F. Tessari, *et al.*, "Challenges and solutions for application and wider adoption of wearable robots," *Wearable Technologies*, vol. 2, e14, 2021.

[64] C. Marquardt, P. Weiner, M. Dežman, and T. Asfour, "Embedded barometric pressure sensor unit for force myography in exoskeletons," in *2022 IEEE-RAS 21st International Conference on Humanoid Robots (Humanoids)*, 2022, pp. 67–73. DOI: `10.1109/Humanoids53995.2022.10000204`.

[65] Y. Jin, C. M. Glover, H. Cho, *et al.*, "Soft Sensing Shirt for Shoulder Kinematics Estimation," *Proceedings - IEEE International Conference on Robotics and Automation*, pp. 4863–4869, 2020, ISSN: 10504729. DOI: `10.1109/ICRA40945.2020.9196586`.

[66] G. E. M. Abro, S. A. B. Zulkifli, K. Kumar, N. El Ouanjli, V. S. Asirvadam, and M. A. Mossa, "Comprehensive review of recent advancements in battery technology, propulsion, power interfaces, and vehicle network systems for intelligent autonomous and connected electric vehicles," *Energies*, vol. 16, no. 6, p. 2925, 2023.

[67] G. S. Sawicki, O. N. Beck, I. Kang, and A. J. Young, "The exoskeleton expansion: Improving walking and running economy," *Journal of NeuroEngineering and Rehabilitation*, vol. 17, no. 1, pp. 1–9, 2020, ISSN: 17430003. DOI: `10.1186/s12984-020-00663-9`.

[68] J. M. Nassar, J. P. Rojas, A. M. Hussain, and M. M. Hussain, "From stretchable to reconfigurable inorganic electronics," *Extreme Mechanics Letters*, vol. 9, pp. 245–268, 2016, ISSN: 2352-4316. DOI: `https://doi.org/10.1016/j.eml.2016.04.011`. [Online]. Available: `https://www.sciencedirect.com/science/article/pii/S2352431616300864`.

[69] M. Xiloyannis, R. Alicea, A.-M. Georgarakis, *et al.*, "Soft robotic exosuits : State of the art , core technologies and open challenges," *IEEE Transactions on Robotics*, vol. (in press), pp. 1–20, 2021.

[70] V. Sanchez, C. J. Walsh, and R. J. Wood, "Textile technology for soft robotic and autonomous garments," *Advanced functional materials*, vol. 31, no. 6, p. 2 008 278, 2021.

[71] C. Laschi and M. Cianchetti, "Soft robotics: New perspectives for robot bodyware and control," *Frontiers in bioengineering and biotechnology*, vol. 2, p. 3, 2014.

[72] S. Podsiadlo, D; Richardson, "The Timed Up and Go: A Test of Basic Functional Mobility for Frail Elderly Persons," *Journal of the American Geriatrics Society*, vol. 39, no. 2, pp. 142–148, 1991.

[73] D. J. Gladstone, C. J. Danells, and S. E. Black, "The Fugl-Meyer Assessment of Motor Recovery after Stroke: A Critical Review of Its Measurement Properties," *Neurorehabilitation and Neural Repair*, vol. 16, no. 3, pp. 232–240, 2002, ISSN: 15459683. DOI: `10.1177/154596802401105171`.

[74] "Towards Restoring Locomotion for Paraplegics: Realizing Dynamically Stable Walking on Exoskeletons," *Proceedings - IEEE International Conference on Robotics and Automation*, pp. 2804–2811, 2018, ISSN: 10504729.

[75] K. Li, M. Tucker, E. Bıyık, *et al.*, "ROIAL: Region of Interest Active Learning for Characterizing Exoskeleton Gait Preference Landscapes," *Proceedings - IEEE International Conference on Robotics and Automation*, vol. 2021-May, no. May, pp. 3212–3218, 2021, ISSN: 10504729. DOI: `10.1109/ICRA48506.2021.9560840`. arXiv: `2011.04812`.

[76] A. Esquenazi, M. Talaty, A. Packel, and M. Saulino, "The Rewalk powered exoskeleton to restore ambulatory function to individuals with thoracic-level motor-complete spinal cord injury," *American Journal of Physical Medicine and Rehabilitation*, vol. 91, no. 11, pp. 911–921, 2012, ISSN: 08949115. DOI: `10.1097/PHM.0b013e318269d9a3`.

[77] "Accelerometry-enabled measurement of walking performance with a robotic exoskeleton: A pilot study," *Journal of NeuroEngineering and Rehabilitation*, vol. 13, no. 1, pp. 1–11, 2016, ISSN: 17430003. DOI: `10.1186/s12984-016-0142-9`. [Online]. Available: `http://dx.doi.org/10.1186/s12984-016-0142-9`.

[78] G. Orekhov and Z. F. Lerner, "Design and Electromechanical Performance Evaluation of a Powered Parallel-Elastic Ankle Exoskeleton," *IEEE Robotics and Automation Letters*, vol. 7, no. 3, pp. 8092–8099, 2022, ISSN: 23773766. DOI: `10.1109/LRA.2022.3185372`.

[79] H. D. Yang, M. Cooper, A. Eckert-Erdheim, D. Orzel, and C. J. Walsh, "A Soft Exosuit Assisting Hip Abduction for Knee Adduction Moment Reduction During Walking," *IEEE Robotics and Automation Letters*, vol. 7, no. 3, pp. 7439–7446, 2022, ISSN: 23773766. DOI: `10.1109/LRA.2022.3182106`.

[80] K. A. Strausser and H. Kazerooni, "The development and testing of a human machine interface for a mobile medical exoskeleton," *2011 IEEE/RSJ International Conference on Intelligent Robots and Systems*, pp. 4911–4916, 2011. DOI: `10.1109/iros.2011.6095025`.

[81] D. H. Gagnon, M. J. Escalona, M. Vermette, *et al.*, "Locomotor training using an overground robotic exoskeleton in long-term manual wheelchair users with a chronic spinal cord injury living in the community: Lessons learned from a feasibility study in terms of recruitment, attendance, learnability, performa," *Journal of NeuroEngineering and Rehabilitation*, vol. 15, no. 1, pp. 1–12, 2018, ISSN: 17430003. DOI: `10.1186/s12984-018-0354-2`.

[82] "Actively controlled lateral gait assistance in a lower limb exoskeleton," *IEEE International Conference on Intelligent Robots and Systems*, pp. 965–970, 2013, ISSN: 21530858. DOI: `10.1109/IROS.2013.6696467`.

[83] T. Kagawa and Y. Uno, "A human interface for stride control on a wearable robot," *2009 IEEE/RSJ International Conference on Intelligent Robots and Systems, IROS 2009*, no. 1, pp. 4067–4072, 2009. DOI: `10.1109/IROS.2009.5353899`.

[84] M. G. McKinley, “Design of Lightweight Assistive Exoskeletons for Individuals with Mobility Disorders - Berkley,” Ph.D. dissertation, UNIVERSITY OF CALIFORNIA, BERKELEY, 2014.

[85] K. Seo, J. Lee, Y. Lee, T. Ha, and Y. Shim, “Fully autonomous hip exoskeleton saves metabolic cost of walking,” *Proceedings - IEEE International Conference on Robotics and Automation*, vol. 2016-June, pp. 4628–4635, 2016, ISSN: 10504729. DOI: `10.1109/ICRA.2016.7487663`.

[86] Z. F. Lerner, G. M. Gasparri, M. O. Bair, *et al.*, “An untethered ankle exoskeleton improves walking economy in a pilot study of individuals with cerebral palsy,” *IEEE Transactions on Neural Systems and Rehabilitation Engineering*, vol. 26, no. 10, pp. 1985–1993, 2018, ISSN: 15344320. DOI: `10.1109/TNSRE.2018.2870756`.

[87] Donald A. Neumann, *"Kinesiology of the Musculoskeletal System Foundations for Rehabilitation"*. Elsevier, 2016, p. 595, ISBN: 978-0-323-28753-1.

[88] D. Lee, B. McLain, I. Kang, and A. Young, “Biomechanical Comparison of Assistance Strategies Using a Bilateral Robotic Knee Exoskeleton,” *IEEE Transactions on Biomedical Engineering*, vol. 68, no. 9, pp. 2870–2879, 2021, ISSN: 15582531. DOI: `10.1109/TBME.2021.3083580`.

[89] T. H. Huang, S. Zhang, S. Yu, *et al.*, “Modeling and Stiffness-Based Continuous Torque Control of Lightweight Quasi-Direct-Drive Knee Exoskeletons for Versatile Walking Assistance,” *IEEE Transactions on Robotics*, vol. 38, no. 3, pp. 1442–1459, 2022, ISSN: 19410468. DOI: `10.1109/TRO.2022.3170287`.

[90] S. Sridar, Z. Qiao, N. Muthukrishnan, W. Zhang, and P. Polygerinos, “A soft-inflatable exosuit for knee rehabilitation: Assisting swing phase during walking,” *Frontiers Robotics AI*, vol. 5, no. MAY, pp. 1–9, 2018, ISSN: 22969144. DOI: `10.3389/frobt.2018.00044`.

[91] “Bio-inspired active soft orthotic device for ankle foot pathologies,” *2011 IEEE/RSJ International Conference on Intelligent Robots and Systems*, pp. 4488–4495, 2011. DOI: `10.1109/iros.2011.6094933`.

[92] R. Ezzibdeh, P. Arora, and D. F. Amanatullah, “Utilization of a pneumatic exoskeleton after total knee arthroplasty,” *Arthroplasty Today*, vol. 5, no. 3, pp. 314–315, 2019, ISSN: 23523441. DOI: `10.1016/j.artd.2019.02.008`. [Online]. Available: `https://doi.org/10.1016/j.artd.2019.02.008`.

[93] P. Beyl, K. Knaepen, S. Duerinck, *et al.*, “Safe and compliant guidance by a powered knee exoskeleton for robot-assisted rehabilitation of gait,” *Advanced Robotics*, vol. 25, no. 5, pp. 513–535, 2011, ISSN: 01691864. DOI: `10.1163/016918611X558225`.

[94] C. M. Thalman, J. Hsu, L. Snyder, and P. Polygerinos, “Design of a soft ankle-foot orthosis exosuit for foot drop assistance,” *Proceedings - IEEE International Conference on Robotics and Automation*, vol. 2019-May, pp. 8436–8442, 2019, ISSN: 10504729. DOI: `10.1109/ICRA.2019.8794005`.

[95] M. Wehner, M. T. Tolley, Y. Mengüç, *et al.*, “Pneumatic Energy Sources for Autonomous and Wearable Soft Robotics,” *Soft Robotics*, vol. 1, no. 4, pp. 263–274, 2014, ISSN: 21695180. DOI: `10.1089/soro.2014.0018`.

[96] R. Auberger, C. Breuer-Ruesch, F. Fuchs, N. Wismer, and R. Riener, “Smart Passive Exoskeleton for Everyday Use with Lower Limb Paralysis: Design and First Results of Knee Joint Kinetics,” *Proceedings of the IEEE RAS and EMBS International Conference on Biomedical Robotics and Biomechatronics*, vol. 2018-Augus, pp. 1109–1114, 2018, ISSN: 21551774. DOI: `10.1109/BIOROB.2018.8488119`.

[97] "C-Brace ® Reshaping the future of orthotics,"

[98] G. A. Pratt and M. M. Williamson, "Series elastic actuators," *IEEE International Conference on Intelligent Robots and Systems*, vol. 1, pp. 399–406, 1995. DOI: `10.1109/iros.1995.525827`.

[99] S. Wolf, G. Grioli, O. Eiberger, *et al.*, "Variable Stiffness Actuators: Review on Design and Components," *IEEE/ASME Transactions on Mechatronics*, vol. 21, no. 5, pp. 2418–2430, 2016, ISSN: 10834435. DOI: `10.1109/TMECH.2015.2501019`.

[100] M. Malosio, G. Spagnuolo, A. Prini, L. Molinari Tosatti, and G. Legnani, "Principle of operation of RotWWC-VSA, a multi-turn rotational variable stiffness actuator," *Mechanism and Machine Theory*, vol. 116, pp. 34–49, 2017, ISSN: 0094114X. DOI: `10.1016/j.mechmachtheory.2017.05.006`.

[101] W. Wang, Y. Zhao, and Y. Li, "Design and Dynamic Modeling of Variable Stiffness Joint Actuator Based on Archimedes Spiral," *IEEE Access*, vol. 6, pp. 43 798–43 807, 2018, ISSN: 21693536. DOI: `10.1109/ACCESS.2018.2864100`.

[102] F. Petit, M. Chalon, W. Friedl, M. Grebenstein, A. Albu-Schäffer, and G. Hirzinger, "Bidirectional antagonistic variable stiffness actuation: Analysis, design & implementation," *Proceedings - IEEE International Conference on Robotics and Automation*, pp. 4189–4196, 2010, ISSN: 10504729. DOI: `10.1109/ROBOT.2010.5509267`.

[103] M. G. Catalano, G. Grioli, M. Garabini, *et al.*, "VSA-CubeBot: A modular variable stiffness platform for multiple degrees of freedom robots," *Proceedings - IEEE International Conference on Robotics and Automation*, pp. 5090–5095, 2011, ISSN: 10504729. DOI: `10.1109/ICRA.2011.5980457`.

[104] R. Van Ham, B. Vanderborght, M. Van Damme, B. Verrelst, and D. Lefeber, "MACCEPA: The mechanically adjustable compliance and controllable equilibrium position actuator for 'Controlled Passive Walking'," *Proceedings - IEEE International Conference on Robotics and Automation*, vol. 2006, no. May, pp. 2195–2200, 2006, ISSN: 10504729. DOI: `10.1109/ROBOT.2006.1642029`.

[105] B. Vanderborght, N. G. Tsagarakis, R. Van Ham, I. Thorson, and D. G. Caldwell, "MACCEPA 2.0: Compliant actuator used for energy efficient hopping robot Chobino1D," *Autonomous Robots*, vol. 31, no. 1, pp. 55–65, 2011, ISSN: 09295593. DOI: `10.1007/s10514-011-9230-7`.

[106] S. Wolf and G. Hirzinger, "A new variable stiffness design: Matching requirements of the next robot generation," *Proceedings - IEEE International Conference on Robotics and Automation*, pp. 1741–1746, 2008, ISSN: 10504729. DOI: `10.1109/ROBOT.2008.4543452`.

[107] M. Dežman and A. Gams, "Rotatable cam-based variable-ratio lever compliant actuator for wearable devices," *Mechanism and Machine Theory*, vol. 130, pp. 508–522, 2018, ISSN: 0094114X. DOI: `10.1016/j.mechmachtheory.2018.09.006`.

[108] A. Jafari, N. G. Tsagarakis, and D. G. Caldwell, "AwAS-II: A new actuator with adjustable stiffness based on the novel principle of adaptable pivot point and variable lever ratio," *Proceedings - IEEE International Conference on Robotics and Automation*, pp. 4638–4643, 2011, ISSN: 10504729. DOI: `10.1109/ICRA.2011.5979994`.

[109] S. S. Groothuis, G. Rusticelli, A. Zucchelli, S. Stramigioli, and R. Carloni, "The variable stiffness actuator vsaUT-II: Mechanical design, modeling, and identification," *IEEE/ASME Transactions on Mechatronics*, vol. 19, no. 2, pp. 589–597, 2014, ISSN: 10834435. DOI: `10.1109/TMECH.2013.2251894`.

[110] J. Sun, Z. Guo, Y. Zhang, X. Xiao, and J. Tan, “A Novel Design of Serial Variable Stiffness Actuator Based on an Archimedean Spiral Relocation Mechanism,” *IEEE/ASME Transactions on Mechatronics*, vol. 23, no. 5, pp. 2121–2131, 2018, ISSN: 10834435. DOI: `10.1109/TMECH.2018.2854742`.

[111] S. Y. Kim, T. Zhang, and D. J. Braun, “Variable Stiffness Springs for Energy Storage Applications,” *Proceedings - IEEE International Conference on Robotics and Automation*, pp. 928–933, 2020, ISSN: 10504729. DOI: `10.1109/ICRA40945.2020.9197245`.

[112] D. J. Braun, V. Chalvet, and A. Dahiya, “Positive – Negative Stiffness Actuators,” vol. 35, no. 1, pp. 162–173, 2019.

[113] S. Y. Kim and D. J. Braun, “Novel Variable Stiffness Spring Mechanism: Modulating Stiffness Independent of the Energy Stored by the Spring,” pp. 8232–8237, 2021, ISSN: 21530866. DOI: `10.1109/iros51168.2021.9636339`.

[114] P. Cherelle, V. Grosu, P. Beyl, *et al.*, “The MACCEPA actuation system as torque actuator in the gait rehabilitation robot ALTACRO,” *2010 3rd IEEE RAS and EMBS International Conference on Biomedical Robotics and Biomechatronics, BioRob 2010*, pp. 27–32, 2010. DOI: `10.1109/BIOROB.2010.5627030`.

[115] A. Jafari, N. G. Tsagarakis, B. Vanderborght, and D. G. Caldwell, “A novel actuator with adjustable stiffness (AwAS),” *IEEE/RSJ 2010 International Conference on Intelligent Robots and Systems, IROS 2010 - Conference Proceedings*, pp. 4201–4206, 2010. DOI: `10.1109/IROS.2010.5648902`.

[116] H. Zheng, M. Wu, and X. Shen, “Pneumatic Variable Series Elastic Actuator,” *Journal of Dynamic Systems, Measurement and Control, Transactions of the ASME*, vol. 138, no. 8, pp. 1–10, 2016, ISSN: 15289028. DOI: `10.1115/1.4033620`.

[117] Y. Sun, P. Tang, D. Dong, J. Zheng, X. Chen, and L. Bai, “Modeling and Experimental Evaluation of a Pneumatic Variable Stiffness Actuator,” *IEEE/ASME Transactions on Mechatronics*, vol. PP, pp. 1–12, 2021, ISSN: 1083-4435. DOI: `10.1109/tmech.2021.3116871`.

[118] X. Luo, D. Song, Z. Zhang, S. Wang, and C. Shi, “A novel distal hybrid pneumatic/cable-driven continuum joint with variable stiffness capacity for flexible gastrointestinal endoscopy,” *Advanced Intelligent Systems*, vol. 5, no. 6, p. 2 200 403, 2023.

[119] C. Xiang, M. E. Giannaccini, T. Theodoridis, L. Hao, S. Nefti-Meziani, and S. Davis, “Variable stiffness mckibben muscles with hydraulic and pneumatic operating modes,” *Advanced Robotics*, vol. 30, no. 13, pp. 889–899, 2016.

[120] B. Laschowski, J. McPhee, and J. Andrysek, “Lower-Limb Prostheses and Exoskeletons With Energy Regeneration: Mechatronic Design and Optimization Review,” *Journal of Mechanisms and Robotics*, vol. 11, no. 4, pp. 1–43, 2019, ISSN: 19424310. DOI: `10.1115/1.4043460`.

[121] Q. Li, V. Naing, and J. M. Donelan, “Development of a biomechanical energy harvester,” *Journal of NeuroEngineering and Rehabilitation*, vol. 6, no. 1, pp. 1–12, 2009, ISSN: 17430003. DOI: `10.1186/1743-0003-6-22`.

[122] J. M. Donelan, Q. Li, V. Naing, J. A. Hoffer, D. J. Weber, and A. D. Kuo, “Biomechanical energy harvesting: Generating electricity during walking with minimal user effort,” *Science*, vol. 319, no. 5864, pp. 807–810, 2008, ISSN: 00368075. DOI: `10.1126/science.1149860`.

[123] R. Chin, E. T. Hsiao-Wecksler, E. Loth, *et al.*, "A pneumatic power harvesting ankle-foot orthosis to prevent foot-drop," *Journal of NeuroEngineering and Rehabilitation*, vol. 6, no. 1, 2009, ISSN: 17430003. DOI: `10.1186/1743-0003-6-19`.

[124] J. Babič, T. Petrič, K. Mombaur, *et al.*, "SPEXOR: Design and development of passive spinal exoskeletal robot for low back pain prevention and vocational reintegration," *SN Applied Sciences*, vol. 1, no. 3, pp. 1–5, 2019, ISSN: 25233971. DOI: `10.1007/s42452-019-0266-1`. [Online]. Available: `https://doi.org/10.1007/s42452-019-0266-1`.

[125] M. Plooij, G. Mathijssen, P. Cherelle, D. Lefeber, and B. Vanderborght, "Lock your robot: A review of locking devices in robotics," *IEEE Robotics and Automation Magazine*, vol. 22, no. 1, pp. 106–117, 2015, ISSN: 10709932. DOI: `10.1109/MRA.2014.2381368`.

[126] Y. Jiang, J. Ma, D. Chen, Z. Liu, Y. Li, and J. Paik, "Compact Pneumatic Clutch with Integrated Stiffness Variation and Position Feedback," *IEEE Robotics and Automation Letters*, vol. 6, no. 3, pp. 5697–5704, 2021, ISSN: 23773766. DOI: `10.1109/LRA.2021.3083236`.

[127] M. Dežman, T. Debevec, J. Babič, and A. Gams, "Effects of passive ankle exoskeleton on human energy expenditure: Pilot evaluation," *Advances in Intelligent Systems and Computing*, vol. 540, pp. 491–498, 2017, ISSN: 21945357. DOI: `10.1007/978-3-319-49058-8{\_}53`.

[128] "Elastic energy-recycling actuators for efficient robots," *Science Robotics*, vol. 9, no. 88, pp. 1–10, 2024, ISSN: 2470-9476. DOI: `10.1126/scirobotics.adj7246`. [Online]. Available: `https://www.science.org/doi/10.1126/scirobotics.adj7246`.

[129] S. Diller, C. Majidi, and S. H. Collins, "A lightweight, low-power electroadhesive clutch and spring for exoskeleton actuation," *Proceedings - IEEE International Conference on Robotics and Automation*, vol. 2016-June, pp. 682–689, 2016, ISSN: 10504729. DOI: `10.1109/ICRA.2016.7487194`.

[130] J. L. Pons, *Wearable robots: biomechatronic exoskeletons.* John Wiley & Sons, 2008.

[131] J. L. Pons, "Witnessing a wearables transition," *Science*, vol. 365, no. 6454, pp. 636–637, 2019, ISSN: 10959203. DOI: `10.1126/science.aaw9407`.

[132] J. Kim, F. Porciuncula, H. D. Yang, *et al.*, "Soft robotic apparel to avert freezing of gait in Parkinson's disease," *Nature Medicine*, vol. 30, no. 1, pp. 177–185, 2024, ISSN: 1546170X. DOI: `10.1038/s41591-023-02731-8`.

[133] C. M. Thalman, L. Baye-wallace, and H. Lee, "A Soft Robotic Hip Exosuit (SR-HExo) to Assist Hip Flexion and Extension during Human Locomotion," *2021 IEEE/RSJ International Conference on Intelligent Robots and Systems (IROS)*, pp. 5060–5066, 2021. DOI: `10.1109/IROS51168.2021.9636225`.

[134] B. Chen, C.-H. Zhong, X. Zhao, H. Ma, L. Qin, and W.-H. Liao, "Reference joint trajectories generation of cuhk-exo exoskeleton for system balance in walking assistance," *IEEE Access*, vol. 7, pp. 33 809–33 821, 2019.

[135] I. Kagirov, A. Karpov, I. Kipyatkova, *et al.*, "Lower limbs exoskeleton control system based on intelligent human-machine interface," in *Intelligent Distributed Computing XIII*, Springer, 2020, pp. 457–466.

[136] C. Bayon, O. Ramírez, J. I. Serrano, *et al.*, "Development and evaluation of a novel robotic platform for gait rehabilitation in patients with cerebral palsy: Cpwalker," *Robotics and autonomous systems*, vol. 91, pp. 101–114, 2017.

[137] J. Choi, K.-T. Kim, J. Lee, S. J. Lee, and H. Kim, “Robust semi-synchronous bci controller for brain-actuated exoskeleton system,” in *2020 8th international winter conference on brain-computer interface (BCI)*, IEEE, 2020, pp. 1–3.

[138] A. G. Kurbis, D. Kuzmenko, B. Ivanyuk-Skulskiy, A. Mihailidis, and B. Laschowski, “Stairnet: Visual recognition of stairs for human–robot locomotion,” *BioMedical Engineering OnLine*, vol. 23, no. 1, p. 20, 2024.

[139] B. Laschowski, W. McNally, A. Wong, and J. McPhee, “Computer vision and deep learning for environment-adaptive control of robotic lower-limb exoskeletons,” in *2021 43rd Annual International Conference of the IEEE Engineering in Medicine & Biology Society (EMBC)*, IEEE, 2021, pp. 4631–4635.

[140] W. Huo, S. Mohammed, Y. Amirat, and K. Kong, “Fast gait mode detection and assistive torque control of an exoskeletal robotic orthosis for walking assistance,” *IEEE Transactions on Robotics*, vol. 34, no. 4, pp. 1035–1052, 2018. DOI: `10.1109/TRO.2018.2830367`.

[141] O. M. Alaoui, F. Expert, G. Morel, and N. Jarrassé, “Using generic upper-body movement strategies in a free walking setting to detect gait initiation intention in a lower-limb exoskeleton,” *IEEE Transactions on Medical Robotics and Bionics*, vol. 2, no. 2, pp. 236–247, 2020.

[142] J. Zhang, C. C. Cheah, and S. H. Collins, “Torque control in legged locomotion,” in *Bioinspired Legged Locomotion*, Elsevier, 2017, pp. 347–400.

[143] L. Mišković, M. Dežman, and T. Petrič, “Pneumatic Quasi-Passive Variable Stiffness Mechanism for Energy Storage Applications,” *IEEE Robotics and Automation Letters*, vol. 7, no. 2, pp. 1705–1712, 2022, ISSN: 23773766. DOI: `10.1109/LRA.2022.3141211`.

[144] L. Mišković, M. Dežman, and T. Petrič, “Pneumatic Exoskeleton Joint with a Self-Supporting Air Tank and Stiffness Modulation: Design, Modeling, and Experimental Evaluation,” *IEEE/ASME Transactions on Mechatronics*, pp. 1–12, 2024. DOI: `10.1109/TMECH.2023.3344998`.

[145] L. Mišković, T. Brecelj, M. Dežman, and T. Petrič, “Active, quasi-passive, pneumatic, and portable knee exoskeleton with bidirectional energy flow for efficient air recovery in sit-stand tasks,” in *2024 IEEE International Conference on Robotics and Automation (ICRA)*, 2024, pp. 15 292–15 298. DOI: `10.1109/ICRA57147.2024.10610457`.

[146] L. Mišković, E. Tricomi, X. Zhang, *et al.*, “Hybrid rigid-soft and pneumatic- electromechanical exoskeleton for multi-joint lower limb assistance,” *IEEE Transactions on Medical Robotics and Bionics*, vol. 6, no. 3, pp. 1180–1189, 2024. DOI: `10.1109/TMRB.2024.3421547`.

[147] C. S. Simpson, C. G. Welker, S. D. Uhlrich, *et al.*, “Connecting the legs with a spring improves human running economy,” *Journal of Experimental Biology*, vol. 222, no. 17, 2019, ISSN: 00220949. DOI: `10.1242/jeb.202895`.

[148] F. A. Panizzolo, E. Annese, A. Paoli, and G. Marcolin, “A single assistive profile applied by a passive hip flexion device can reduce the energy cost of walking in older adults,” *Applied Sciences (Switzerland)*, vol. 11, no. 6, 2021, ISSN: 20763417. DOI: `10.3390/app11062851`.

[149] A. Sutrisno and D. J. Braun, "Enhancing Mobility with Quasi-Passive Variable Stiffness Exoskeletons," *IEEE Transactions on Neural Systems and Rehabilitation Engineering*, vol. 27, no. 3, pp. 487–496, 2019, ISSN: 15344320. DOI: `10.1109/TNSRE.2019.2899753`.

[150] M. Doumit, S. Member, A. Fahim, and M. Munro, "Analytical Modeling and Experimental Validation of the Braided Pneumatic Muscle," *IEEE Transactions on Robotics*, vol. 25, no. 6, pp. 1282–1291, 2009.

[151] C. Suulker, S. Skach, and K. Althoefer, "Soft robotic fabric actuator with elastic bands for high force and bending performance in hand exoskeletons," *IEEE Robotics and Automation Letters*, vol. 7, no. 4, pp. 10 621–10 627, 2022. DOI: `10.1109/LRA.2022.3194883`.

[152] D. Plettenburg, "Pneumatic actuators: A comparison of energy-to-mass ratio's," in *9th International Conference on Rehabilitation Robotics, 2005. ICORR 2005.*, 2005, pp. 545–549. DOI: `10.1109/ICORR.2005.1502022`.

[153] H. K. Yap, J. H. Lim, F. Nasrallah, J. C. Goh, and R. C. Yeow, "A soft exoskeleton for hand assistive and rehabilitation application using pneumatic actuators with variable stiffness," *Proceedings - IEEE International Conference on Robotics and Automation*, vol. 2015-June, no. June, pp. 4967–4972, 2015, ISSN: 10504729. DOI: `10.1109/ICRA.2015.7139889`.

[154] A. J. Young and D. P. Ferris, "State of the art and future directions for lower limb robotic exoskeletons," *IEEE Transactions on Neural Systems and Rehabilitation Engineering*, vol. 25, no. 2, pp. 171–182, 2017, ISSN: 15344320. DOI: `10.1109/TNSRE.2016.2521160`.

[155] T. Noda, T. Teramae, B. Ugurlu, and J. Morimoto, "Development of an upper limb exoskeleton powered via pneumatic electric hybrid actuators with bowden cable," *IEEE International Conference on Intelligent Robots and Systems*, no. Iros, pp. 3573–3578, 2014, ISSN: 21530866. DOI: `10.1109/IROS.2014.6943062`.

[156] Y. Sun, P. Tang, D. Dong, J. Zheng, X. Chen, and L. Bai, "Modeling and Experimental Evaluation of a Pneumatic Variable Stiffness Actuator," *IEEE/ASME Transactions on Mechatronics*, vol. PP, pp. 1–12, 2021, ISSN: 1083-4435. DOI: `10.1109/tmech.2021.3116871`.

[157] M. Martens and I. Boblan, "Modeling the static force of a Festo pneumatic muscle actuator: A new approach and a comparison to existing models," *Actuators*, vol. 6, no. 4, pp. 1–11, 2017, ISSN: 20760825. DOI: `10.3390/act6040033`.

[158] K. Schmidt, J. E. Duarte, M. Grimmer, *et al.*, "The myosuit: Bi-articular antigravity exosuit that reduces hip extensor activity in sitting transfers," *Frontiers in Neurorobotics*, vol. 11, no. OCT, pp. 1–16, 2017, ISSN: 16625218. DOI: `10.3389/fnbot.2017.00057`.

[159] L. Liu, Z. Hong, B. Penzlin, *et al.*, "Low Impedance-Guaranteed Gain-Scheduled GESO for Torque-Controlled VSA with Application of Exoskeleton-Assisted Sit-to-Stand," *IEEE/ASME Transactions on Mechatronics*, vol. 26, no. 4, pp. 2080–2091, 2021, ISSN: 1941014X. DOI: `10.1109/TMECH.2020.3032372`.

[160] H. Zhu, C. Nesler, N. Divekar, V. Peddinti, and R. D. Gregg, "Design Principles for Compact, Backdrivable Actuation in Partial-Assist Powered Knee Orthoses," *IEEE/ASME Transactions on Mechatronics*, vol. 26, no. 6, pp. 3104–3115, 2021, ISSN: 1941014X. DOI: `10.1109/TMECH.2021.3053226`.

[161] J. Vantilt, K. Tanghe, M. Afschrift, *et al.*, "Model-based control for exoskeletons with series elastic actuators evaluated on sit-to-stand movements," *Journal of NeuroEngineering and Rehabilitation*, vol. 16, no. 1, pp. 1–21, 2019, ISSN: 17430003. DOI: `10.1186/s12984-019-0526-8`.

[162] X. Wu, W. Cao, H. Yu, Z. Zhang, Y. Leng, and M. Zhang, "Generating Electricity During Locomotion Modes Dominated by Negative Work via a Knee Energy-Harvesting Exoskeleton," pp. 1–11, 2022.

[163] A. M. Dollar and H. Herr, "Design of a quasi-passive knee exoskeleton to assist running," *2008 IEEE/RSJ International Conference on Intelligent Robots and Systems, IROS*, pp. 747–754, 2008. DOI: `10.1109/IROS.2008.4651202`.

[164] B. Laschowski, R. S. Razavian, and J. McPhee, "Simulation of Stand-to-Sit Biomechanics for Robotic Exoskeletons and Prostheses with Energy Regeneration," *IEEE Transactions on Medical Robotics and Bionics*, vol. 3, no. 2, pp. 455–462, 2021, ISSN: 25763202. DOI: `10.1109/TMRB.2021.3058323`.

[165] D. Maeda, K. Tominaga, T. Oku, *et al.*, "Muscle synergy analysis of human adaptation to a variable-stiffness exoskeleton: Human walk with a knee exoskeleton with pneumatic artificial muscles," *IEEE-RAS International Conference on Humanoid Robots*, no. 1, pp. 638–644, 2012, ISSN: 21640572. DOI: `10.1109/HUMANOIDS.2012.6651587`.

[166] K. Knaepen, P. Beyl, S. Duerinck, F. Hagman, D. Lefeber, and R. Meeusen, "Human-robot interaction: Kinematics and muscle activity inside a powered compliant knee exoskeleton," *IEEE Transactions on Neural Systems and Rehabilitation Engineering*, vol. 22, no. 6, pp. 1128–1137, 2014, ISSN: 15344320. DOI: `10.1109/TNSRE.2014.2324153`.

[167] H. J. Hermens, B. Freriks, C. Disselhorst-Klug, and G. Rau, "Development of recommendations for SEMG sensors and sensor placement procedures," *J. Electromyogr. Kinesiol*, vol. 10, no. 5, pp. 361–374, 2000, ISSN: 15735117. DOI: `10.1007/s10750-015-2551-3`.

[168] N. Jarrassé and G. Morel, "Connecting a human limb to an exoskeleton," *IEEE Transactions on Robotics*, vol. 28, no. 3, pp. 697–709, 2012, ISSN: 15523098. DOI: `10.1109/TRO.2011.2178151`.

[169] H. Zhu, C. Nesler, N. Divekar, V. Peddinti, and R. D. Gregg, "Design Principles for Compact, Backdrivable Actuation in Partial-Assist Powered Knee Orthoses," *IEEE/ASME Transactions on Mechatronics*, vol. 26, no. 6, pp. 3104–3115, 2021, ISSN: 1941014X. DOI: `10.1109/TMECH.2021.3053226`.

[170] M. K. MacLean and D. P. Ferris, "Energetics of walking with a robotic knee exoskeleton," *Journal of Applied Biomechanics*, vol. 35, no. 5, pp. 320–326, 2019, ISSN: 15432688. DOI: `10.1123/jab.2018-0384`.

[171] K. Seo, K. Kim, Y. J. Park, *et al.*, "Adaptive Oscillator-Based Control for Active Lower-Limb Exoskeleton and its Metabolic Impact," *Proceedings - IEEE International Conference on Robotics and Automation*, pp. 6752–6758, 2018, ISSN: 10504729. DOI: `10.1109/ICRA.2018.8460841`.

[172] E. Tricomi, M. Mossini, F. Missiroli, *et al.*, "Environment-Based Assistance Modulation for a Hip Exosuit Via Computer Vision," *IEEE Robotics and Automation Letters*, vol. 8, no. 5, pp. 1–8, 2023, ISSN: 23773766. DOI: `10.1109/lra.2023.3256135`.

[173] E. J. Park, T. Akbas, A. Eckert-Erdheim, *et al.*, “A Hinge-Free, Non-Restrictive, Lightweight Tethered Exosuit for Knee Extension Assistance during Walking,” *IEEE Transactions on Medical Robotics and Bionics*, vol. 2, no. 2, pp. 165–175, 2020, ISSN: 25763202. DOI: `10.1109/TMRB.2020.2989321`.

[174] Z. Wang, C. Chen, F. Yang, Y. Liu, G. Li, and X. Wu, “Real-Time Gait Phase Estimation Based on Neural Network and Assistance Strategy Based on Simulated Muscle Dynamics for an Ankle Exosuit,” *IEEE Transactions on Medical Robotics and Bionics*, vol. 5, no. 1, pp. 100–109, 2023, ISSN: 25763202. DOI: `10.1109/TMRB.2023.3240284`.

[175] B. T. Quinlivan, S. Lee, P. Malcolm, *et al.*, “Assistance magnitude versus metabolic cost reductions for a tethered multiarticular soft exosuit,” *Science robotics*, vol. 2, no. 2, eaah4416, 2017.

[176] Z. Wang, Z. Zhou, L. Ruan, X. Duan, and Q. Wang, “Mechatronic Design and Control of a Rigid-Soft Hybrid Knee Exoskeleton for Gait Intervention,” *IEEE/ASME Transactions on Mechatronics*, vol. 28, no. 5, pp. 2553–2564, 2023, ISSN: 1941014X. DOI: `10.1109/TMECH.2023.3245810`.

[177] H. Aguilar-Sierra, R. Lopez, W. Yu, S. Salazar, and R. Lozano, “A lower limb exoskeleton with hybrid actuation,” in *5th IEEE RAS/EMBS International Conference on Biomedical Robotics and Biomechatronics*, IEEE, 2014, pp. 695–700.

[178] S. V. Sarkisian, M. K. Ishmael, and T. Lenzi, “Self-Aligning Mechanism Improves Comfort and Performance with a Powered Knee Exoskeleton,” *IEEE Transactions on Neural Systems and Rehabilitation Engineering*, vol. 29, pp. 629–640, 2021, ISSN: 15580210. DOI: `10.1109/TNSRE.2021.3064463`.

[179] A. S. McIntosh, K. T. Beatty, L. N. Dwan, and D. R. Vickers, “Gait dynamics on an inclined walkway,” *Journal of Biomechanics*, vol. 39, no. 13, pp. 2491–2502, 2006, ISSN: 00219290. DOI: `10.1016/j.jbiomech.2005.07.025`.

[180] E. Tricomi, N. Lotti, F. Missiroli, *et al.*, “Underactuated Soft Hip Exosuit Based on Adaptive Oscillators to Assist Human Locomotion,” *IEEE Robotics and Automation Letters*, vol. 7, no. 2, pp. 936–943, 2022, ISSN: 23773766. DOI: `10.1109/LRA.2021.3136240`.

[181] J. S. Gottschall and R. Kram, “Energy cost and muscular activity required for leg swing during walking,” vol. 99, no. 1, pp. 23–30, 2004. DOI: `10.1152/japplphysiol.01190.2004.`.

[182] T. Petrič, A. Gams, A. J. Ijspeert, and L. Žlajpah, “On-line frequency adaptation and movement imitation for rhythmic robotic tasks,” *International Journal of Robotics Research*, vol. 30, no. 14, pp. 1775–1788, 2011, ISSN: 02783649. DOI: `10.1177/0278364911421511`.

[183] L. Righetti, J. Buchli, and A. J. Ijspeert, “Dynamic Hebbian learning in adaptive frequency oscillators,” *Physica D: Nonlinear Phenomena*, vol. 216, no. 2, pp. 269–281, 2006, ISSN: 01672789. DOI: `10.1016/j.physd.2006.02.009`.

[184] L. Righetti, J. Buchli, and A. J. Ijspeert, “Adaptive Frequency Oscillators and Applications,” *The Open Cybernetics & Systemics Journal*, vol. 3, no. 2, pp. 64–69, 2009, ISSN: 1874110X. DOI: `10.2174/1874110x00903020064`.

[185] M. Haggerty, D. C. Dickin, J. Popp, and H. Wang, “The influence of incline walking on joint mechanics,” *Gait and Posture*, vol. 39, no. 4, pp. 1017–1021, 2014, ISSN: 18792219. DOI: `10.1016/j.gaitpost.2013.12.027`. [Online]. Available: `http://dx.doi.org/10.1016/j.gaitpost.2013.12.027`.

[186] F. Peronnet and D. Massicotte, "Table of nonprotein respiratory quotient: an update," *Can J Sport Sci*, vol. 16, no. November, pp. 23–29, 1991.

[187] F. A. Panizzolo, G. M. Freisinger, N. Karavas, *et al.*, "Metabolic cost adaptations during training with a soft exosuit assisting the hip joint," *Scientific Reports*, vol. 9, no. 1, pp. 1–10, 2019, ISSN: 20452322. DOI: `10.1038/s41598-019-45914-5`.

[188] N. Bianco, P. W. Franks, J. L. Hicks, and S. L. Delp, "Coupled exoskeleton assistance simplifies control and maintains metabolic benefits : A simulation study," *PLoS ONE*, pp. 1–18, 2022. DOI: `10.1371/journal.pone.0261318`. [Online]. Available: `http://dx.doi.org/10.1371/journal.pone.0261318`.

[189] P. W. Franks, G. M. Bryan, R. M. Martin, R. Reyes, A. C. Lakmazaheri, and S. H. Collins, "Comparing optimized exoskeleton assistance of the hip, knee, and ankle in single and multi-joint configurations," *Wearable Technologies*, vol. 2, 2021, ISSN: 26317176. DOI: `10.1017/wtc.2021.14`.

[190] K. Shamaei, M. Cenciarini, A. A. Adams, K. N. Gregorczyk, J. M. Schiffman, and A. M. Dollar, "Biomechanical effects of stiffness in parallel with the knee joint during walking," *IEEE Transactions on Biomedical Engineering*, vol. 62, no. 10, pp. 2389–2401, 2015, ISSN: 15582531. DOI: `10.1109/TBME.2015.2428636`.

[191] Y. M. Zhou, C. J. Hohimer, H. T. Young, *et al.*, "A portable inflatable soft wearable robot to assist the shoulder during industrial work," *Science Robotics*, vol. 9, no. 91, eadi2377, 2024.

[192] T. Proietti, C. O'Neill, L. Gerez, *et al.*, "Restoring arm function with a soft robotic wearable for individuals with amyotrophic lateral sclerosis," *Science Translational Medicine*, vol. 15, no. 681, pp. 1–13, 2023, ISSN: 19466242. DOI: `10.1126/scitranslmed.add1504`.

Bibliography

Publications Related to the Thesis

Journal Articles

L. Mišković, E. Tricomi, X. Zhang, *et al.*, “Hybrid rigid-soft and pneumatic- electromechanical exoskeleton for multi-joint lower limb assistance,” *IEEE Transactions on Medical Robotics and Bionics*, vol. 6, no. 3, pp. 1180–1189, 2024. DOI: `10.1109/TMRB.2024.3421547`.

L. Mišković, M. Dežman, and T. Petrič, “Pneumatic Exoskeleton Joint with a Self-Supporting Air Tank and Stiffness Modulation: Design, Modeling, and Experimental Evaluation,” *IEEE/ASME Transactions on Mechatronics*, pp. 1–12, 2024. DOI: `10.1109/TMECH.2023.3344998`.

L. Mišković, M. Dežman, and T. Petrič, “Pneumatic Quasi-Passive Variable Stiffness Mechanism for Energy Storage Applications,” *IEEE Robotics and Automation Letters*, vol. 7, no. 2, pp. 1705–1712, 2022, ISSN: 23773766. DOI: `10.1109/LRA.2022.3141211`.

Conference Paper

L. Mišković, E. Tricomi, X. Zhang, *et al.*, “Coupling Rigid Pneumatic Knee Exoskeleton with Soft Tendon-Driven Hip Exosuit: First Insights,” *IEEE RAS EMBS 10th International Conference on Biomedical Robotics and Biomechatronics (BioRob)*, 2024.

V. Gerhard, L. Mišković, A. Nanni, *et al.*, “Design of a high Bandwidth Wearable Actuation for seamless Assistance in Walking and Running,” *IEEE RAS EMBS 10th International Conference on Biomedical Robotics and Biomechatronics (BioRob)*, 2024.

L. Mišković, T. Brecelj, M. Dežman, and T. Petrič, “Active, quasi-passive, pneumatic, and portable knee exoskeleton with bidirectional energy flow for efficient air recovery in sit-stand tasks,” in *2024 IEEE International Conference on Robotics and Automation (ICRA)*, 2024, pp. 15 292–15 298. DOI: `10.1109/ICRA57147.2024.10610457`.

L. Mišković and T. Petrič, “Variable stiffness joint based on pneumatic relocation mechanism,” in *International Conference on Robotics in Alpe-Adria Danube Region*, Springer, 2023, pp. 73–80.

L. Mišković, M. Dežman, and T. Petrič, “Modular quasi-passive mechanism for energy storage applications: Towards lightweight high-performance exoskeleton,” *2021 20th International Conference on Advanced Robotics, ICAR 2021*, pp. 588–593, 2021. DOI: `10.1109/ICAR53236.2021.9659353`.

L. Mišković, E. Tricomi, X. Zhang, *et al.*, “Optimizing end-effector force during the sit-stand task on the Talos humanoid bipedal robot,” *30th International Electrotechnical and Computer Science Conference in Portorož, Slovenia*, 2021.

Patents

L. Mišković, M. Dežman, and T. Petrič, "Quasi-passive mechanism for prosthetic or orthotic joint and a method for stiffness modulation" (Slovenian version), in Ljubljana, Slovenia, 2022.

Biography

The author of this dissertation was born on December 22, 1995 in Zagreb, Croatia. He received his bachelor's degree in 2018 from the Faculty of Mechanical Engineering at the University of Zagreb. He continued his studies at the same faculty and graduated from the Master's program in Mechatronics and Robotics in 2020. In the same year, he joined the Jožef Stefan Institute under the Young Researcher program of the Slovenian Research Agency. Here, he pursued a Ph.D. degree, focusing on wearable robotics within the Department of Automatics, Robotics, and Biocybernetics, alongside the CoBoTaT laboratory. Between May and November 2023, he worked as a visiting student in the Assistive Robotics and Interactive Exosuits (ARIES) Lab at Heidelberg University to facilitate collaboration between the two institutions and enrich his research portfolio. His main research interests include design, actuation, and control of lower limb exoskeletons. So far, his applied research culminated in several innovative physical prototypes, one of which has been patented, while others were published in prestigious peer-reviewed journals and several scientific conferences. He has gained extensive experience in mechanical and electronic design, prototyping mechatronic systems and control using Matlab and Simulink. Other relevant achievements are described below.

Conference presentations

September 2024: Oral and poster presentations at the IEEE RAS EMBS BioRob (International Conference on Biomedical Robotics and Biomechatronics), in Heidelberg, Germany, 2024.

May 2024: Oral and poster presentations at the IEEE ICRA (International Conference on Robotics and Automation), in Yokohama, Japan, 2024.

June 2023: Oral presentation at the 32$^{\text{nd}}$ International Conference on Robotics in Alpe-Adria-Danube Region (RAAD), in Bled, Slovenia, 2023.

May 2022: Oral and poster presentations at the IEEE ICRA (International Conference on Robotics and Automation), the flagship conference of the IEEE Robotics and Automation Letters journal, in Philadelphia, USA, 2022.

December 2021: Oral presentation at the IEEE ICAR (International Conference on Advanced Robotics), in Ljubljana, Slovenia, 2021.

September 2021: Oral presentation at the IEEE ERK (International Electrotechnical and Computer Science Conference ERK), in Portorož, Slovenia, 2021.

May 2021: Oral presentation (online) at the 13th IPSSC (Student conference of the International Postgraduate School of Jožef Stefan), in Slovenia, 2021.

Research visits

May 2023 - November 2023: Research visit at the ARIES (Assistive Robotics and Interactive Exosuits) Lab of Prof. Dr. Lorenzo Masia, to design a hybrid assistive device.

Summer and winter schools

December 2021: International Winter School on Smart Materials for Soft Robots, Department of Engineering University of Cambridge, UK, 2021.

September 2021: Summer School on Wearable Robotics, COST Association – European Cooperation in Science and Technology, Isla de Valdecañas, Spain, 2021.

Guest lectures

June 2021: Guest lecture: "Challenges, solutions and future directions for robotic exoskeletons and prostheses", at the Faculty of Mechanical Engineering, University of Zagreb.